

NOVEL DESIGN-BASED COMPLEX
NANOSTRUCTURES IN HYBRID CORE-
SHELL ARCHITECTURES FOR HIGH-
EFFICIENCY LIGHT GENERATION

A THESIS

SUBMITTED TO THE DEPARTMENT OF PHYSICS
AND THE INSTITUTE OF ENGINEERING AND SCIENCES
OF BILKENT UNIVERSITY

IN PARTIAL FULLFILMENT OF THE REQUIREMENTS

FOR THE DEGREE OF
MASTER OF SCIENCE

By

Ilkem Özge Özel

July 2010

I certify that I have read this thesis and that in my opinion it is fully adequate, in scope and in quality, as a thesis for the degree of Master of Science.

Assoc. Prof. Dr. Hilmi Volkan Demir (Supervisor)

I certify that I have read this thesis and that in my opinion it is fully adequate, in scope and in quality, as a thesis for the degree of Master of Science.

Assist. Prof. Dr. Dönüş Tuncel

I certify that I have read this thesis and that in my opinion it is fully adequate, in scope and in quality, as a thesis for the degree of Master of Science.

Assoc. Prof. Dr. Ceyhun Bulutay

Approved for the Institute of Engineering and Sciences:

Prof. Dr. Levent Onural
Director of Institute of Engineering and Sciences

ABSTRACT

NOVEL DESIGN-BASED COMPLEX NANOSTRUCTURES IN HYBRID CORE-SHELL ARCHITECTURES FOR HIGH-EFFICIENCY LIGHT GENERATION

İlkem Özge Özel

M.S. in Physics

Supervisor: Assoc. Prof. Dr. Hilmi Volkan Demir

July 2010

Recent developments in nanoscience and nanotechnology have given rise to the discovery of hybrid nanostructured multi-component materials that serve several tasks all at once. A very important and rapidly growing field of these materials is the development of highly efficient fluorophores to meet the urgent demand of low-energy consuming, high-quality light emitters for future solid-state lighting applications. Such hybrid nanomaterials are entailed to exhibit extraordinary optoelectronic properties compared to the bulk case of their single components such as enhanced quantum efficiency, tunable multi-color emission, and reduction of multiple processing steps. Herein, to address these requirements, we propose and demonstrate novel design-based complex nanomaterials in hybrid multi-shell architectures for high-efficiency light generation. These requirements are made possible by using the concept of hybrid core-shell-... nanostructures comprising at least two units, including hybrid metal-core/dielectric-shell nanoparticles furnished with an outer shell of semiconductor nanocrystals for enhanced emission and different conjugated polymers forming a single multi-polymer nanoparticle and emitting

simultaneously at different wavelengths. In the first part of this thesis, we developed and demonstrated Au-silica core/shell nanoparticles that successfully assemble CdTe nanocrystals right on their silica shells for enhanced plasmon-exciton interactions, while solving the common problems of lacking control in dielectric spacing and limited film thickness typically encountered in such plasmon-coupled nanocrystals. Here we present the synthesis and characterization results of this new set of multi-shell decorated nanoparticle composites with a tunable dielectric spacing thickness of silica shell precisely controlled by synthesis to optimize plasmon-exciton interactions for enhanced emission. Experimental data obtained from steady-state and time-resolved photoluminescence measurements together with extensive computational analysis clearly verify the strong plasmon-exciton interactions in these design-based multi-shell nanocomposites. In the second part, we construct bi-polymer nanoparticle systems in various architectures of core/shells, for each of which thorough investigations of the non-radiative energy transfer mechanisms are made. Here we present the synthesis and characterization results of these core/shell bi-polymer nanoassemblies. The flexibility of designing such bi-polymer nanostructures allows for the optimization of maximum energy transfer efficiency. This concept of complex hybrid nanostructures for high-efficiency light generation opens up new paths for optoelectronic devices and nanophotonics applications including those in solid-state lighting.

Keywords: Nanostructures, nanomaterials; plasmonics, localized plasmons, metal-enhanced luminescence; exciton migration, non-radiative energy transfer, Förster resonance energy transfer (FRET); hybrid nanoparticles, metal nanoparticles; semiconductor nanocrystals, colloidal quantum dots; conjugated polymers; excitons, spontaneous emission, photoluminescence, time-resolved fluorescence; FDTD.

ÖZET

YÜKSEK VERİMLİ IŞIK ÜRETİMİ İÇİN MELEZ ÇEKİRDEK-KABUK MİMARİLİ YENİLİKÇİ DİZAYN TEMELLİ KOMPLEKS NANOYAPILAR

İlkem Özge Özel

Fizik Bölümü Yüksek Lisans

Tez Yöneticisi: Doç. Dr. Hilmi Volkan Demir

Temmuz 2010

Nanobilim ve nanoteknolojideki yeni gelişmeler çoklu içerikli malzeme içeren birçok görevi tek başına yapabilen melez nanoyapıların keşfine yol açmıştır. Geleceğin katı hal aydınlanma uygulamalarının acil ihtiyacı olan düşük enerji tüketimli, yüksek kaliteli ışık yayıcı ihtiyacının karşılanması amaçlı olarak yüksek verimli ışık üretiminin geliştirilmesi bu malzemelerin çok önemli ve hızlı bir şekilde gelişen bir alanıdır. Böyle melez nanomalzemelerin tek içerikli büyük boyutlarına göre arttırılmış kuvantum verimliliği, ayarlanabilir çok renkli ışık ve çoklu işlem basamaklarının azalması gibi olağandışı optoelektronik özellikler göstermesini gerektirmektedir. Burada bu gereksinimleri hedefleyen yüksek verimli ışık üretimini için yenilikçi dizayn temelli çoklu kabuklu melez mimaride kompleks nanomalzemeleri teklif ediyor ve gösteriyoruz. Bu gereksinimler arttırılmış ışık üretimi amaçlı melez çekirdek-kabuk-(...) konseptindeki en az iki birim içeren en dış kabuğu yarıiletken nanokristallerle döşenmiş metal-çekirdek/yalıtkan-kabuk nanoparçacıklar ve farklı konjuge polimerle çoklu polimer içeren ve eş zamanlı farklı dalgaboylarında ışık tek nanoparçacıklar ile giderilmiştir. Bu tezin ilk kısmında, arttırılmış plazmon-ekziton etkileşimleri için aynı zamanda plazmon etkileşimli nanokristallerin

genel sorunu olan yalıtkan ayraç kalınlık kontrolü ve sınırlı film kalınlığı gibi sorunları çözen silica kabuğun hemen üzerinde yerleştirilmiş CdTe nanokristalleri olan Au-Silika çekirdek/kabuk nanoparçacıkların geliştirilmesi ve gösterimi vardır. Burada arttırılmış ışık yayılımı için bu yeni set plazmon-ekziton etkileşimleri optimizasyonu için kalınlığı sentez esnasında ayarlanabilir yalıtkan ayraçlı çoklu-kabuk döşenmiş nanoparçacık kompozitlerin sentez ve karakterizasyon sonuçları sunulmaktadır. Sabit ve zaman çözünürlü fotoışma ölçümlerinden elde edilen deneysel veriler ve bilgisayarlı derin analizler bu dizayn tabanlı çoklu-kabuk nanokompozitleride güçlü plazmon-ekziton etkileşimleri olduğunu net bir şekilde göstermektedir. İkinci kısımda çift-polimer nanoparçacık sistemlerini her birinde ışık yayılımsız enerji transfer mekanizmalarını incelemek üzere değişik çekirdek-kabuk mimarilerinde yapılandırdık. Burada bu çekirdek/kabuk çift polimer nanobirleşimlerin sentez ve karakterizasyon sonuçlarını sunuyoruz. Bu tarz çift-polimer nanoyapı dizayn esnekliği maksimum enerji transfer verimliliğinin optimizasyonuna izin vermektedir. Yüksek verimli ışık üretimi amaçlı bu kompleks melez nanoyapılar konsepti optoelektronik aygıt ve katı hal aydınlanmayı da içeren nanofotonik uygulamalarında yeni bir yol açmaktadır.

Keywords: Nanoyapılar, nanomalzemeler; plazmonik, localize plazmonlar, metalle arttırılan ışma; ekziton göçü, ışık yayılımsız enerji transferi, Förster rezonans enerji transferi (FRET); melez nanoparçacıklar, metal nanoparçacıklar; yarıiletken nanokristaller, kolloid kuvantum noktacıklar; konjuge polimerler; ekzitonlar, kendiliğinden ışınsalım, fotoışma, zaman çözünürlü ışma; FDTD.

Acknowledgements

I am grateful to Assoc. Prof. Dr. Hilmi Volkan Demir, for giving me the opportunity to undertake the research outlined in this thesis. Along with his positive attitude to life and his endless support, as well as his hard work on the project, his enthusiasm has maintained my growing interests in various fields of research.

It is also an honor for me to thank my co-advisor, Asst. Prof. Dr. Dönüş Tuncel, who has made her support available in a number of ways. I would like to thank her for her guidance and support in our collaborative research works. Her advice and suggestions helped me enormously over the past five years.

I would like to thank Assoc. Prof. Dr. Ceyhun Bulutay for his useful comments and suggestions as being a member of my thesis committee.

During the course of this work at Bilkent University (2008 – 2010), I was fully supported in by the TÜBİTAK National Scholarship Programme-2210 for MSc Students for which I owe special thanks.

I wish to thank UNAM and staff for providing the lab facilities and especially Mustafa Güler for taking all my TEM images and being very kind to me.

I would like to thank all former and recent group members of Devices and Sensors Group, who work under the supervision of Assoc. Prof. Dr. Hilmi Volkan Demir. I would especially like to thank Asli Yilmaz, Olga Samarskaya, Nihan Kosku Perkgoz, Hatice Ertugrul, Neslihan Cicek, Gülis Zengin, Emre Sari, Can Uran, Gurkan Polat, Murat Soganci, Akin Sefunc, Ozgun Akyuz, Emre Unal, Sina Toru, Talha Erdem, Burak Guzelturk, Ugur Karatay, and Cuneyt Eroglu for their friendship and collaborations.

I would like to thank all former and recent group members of PLED Group, who work under the supervision of Assist. Prof. Dr. Donus Tuncel. I would especially like to thank Muge Artar, Vusala Imbrahimova, Eun Ju Park, Zeynep Goksel Ozsarp, Gizem Celtek, Gizem Er, Unsal Koldemir, Ibrahim Hocaoglu, for their friendship and collaborations.

There are some very special friends to me with whom some of them we have shared almost all the years at Bilkent. These are Seçkin and Özlem Şenlik, Samed Yumrukçu and Şeyda İpek. I am glad to be sharing such a nice friendship, which I hope will never end. I always feel very lucky to be their close friends. I want to say how glad I am to meet Evren Mutlugün and his wife Sümeyye who are a cheer supply for me all the time, Rohat and Bahar Melik who always treated me and Tuncay as his younger siblings, Sedat Nizamoğlu who is always kind and helpful in my research. Those are very special friends to me and they were always there when I needed them.

Last, but not least, I thank my entire extended family: my parents, Ayhan and İlhan Huyal for giving me life in the first place, and for their unconditional love, support and encouragement to pursue my interests. I would especially like to thank my sister Simge for listening to my complaints and frustrations, and for believing in me all the time and my brother Ulaş, for always being there when I had questions and his interesting discussions on almost any irrelevant field. I would like to deeply thank to my new family members, my mother-in-law Yıldız Özel and my father-in-law Ali Özel for their sincere love as if I am their daughter, being always kind to me and supporting me in all respects and raising Tuncay up as a great person. Also my thanks go to my brother-in-law Taner and his wife Zülal Tezcan Özel for their guidance and support.

And finally, my deepest gratitude goes to my husband Tuncay Özel, without whom this thesis would not be possible. Tuncay had confidence in me when I

doubted myself, and brought out the good ideas in me. His endless love and support has created what I am today for which I will be ever indebted. To him I dedicate this thesis.

Table of Contents

ABSTRACT	III
ÖZET	V
ACKNOWLEDGEMENTS	VII
TABLE OF CONTENTS	X
CHAPTER 1	1
INTRODUCTION	1
CHAPTER 2	7
FLUORESCENT CONJUGATED POLYMERS	7
2.1 POLYFLUORENES: A NOVEL CLASS OF LIGHT EMITTING POLYMERS	7
CHAPTER 3	16
SEMICONDUCTOR NANOCRYSTALS	16
3.1 SIZE AND COLOR TUNING: THE QUANTUM SIZE EFFECT	19
3.2 CdTe NANOCRYSTAL SYNTHESIS	20
3.3 MEASUREMENT OF FLUORESCENCE QUANTUM EFFICIENCY	23
CHAPTER 4	25
FUNDAMENTALS OF SURFACE PLASMONS	25
4.1 OPTICAL PROPERTIES OF METALS	27
4.1.1 MIE SCATTERING	34
4.1.2 SIZE, SHAPE, COMPOSITION AND ENVIRONMENT DEPENDENCY OF SURFACE PLASMONS	35
4.1.4 METHODS FOR METAL NANOPARTICLE FORMATION	37
CHAPTER 5	39
AU-SILICA CORE/SHELL HYBRID NANOPARTICLES FURNISHED WITH CdTe NANOCRYSTALS FOR ENHANCED PLASMON-EXCITON INTERACTIONS	39
5.1 STATE-OF-THE-ART	40
5.2 COMPUTATIONAL ANALYSIS AND EXPERIMENTAL DEMONSTRATION WITH OPTICAL CHARACTERIZATION RESULTS OF OUR HYBRID CdTe FURNISHED AU-SILICA CORE/SHELL NANOPARTICLES	44
5.2.1 SYNTHESIS, CHARACTERIZATION, AND SIMULATION OF HYBRID NANO-ASSEMBLIES	45
5.2.2 EXPERIMENTAL DEMONSTRATION AND OPTICAL CHARACTERIZATION RESULTS AND NUMERICAL ANALYSIS	49
CHAPTER 6	67
NON-RADIATIVE ENERGY TRANSFER IN BI-POLYMER NANOPARTICLES OF FLUORESCENT CONJUGATED POLYMERS	67
6.1 FÖRSTER RESONANCE ENERGY TRANSFER IN ORGANIC SYSTEMS	67
6.2 A NEW APPROACH FOR THE PREPARATION OF DUAL-EMITTING POLYMER NANOPARTICLES	69
6.3 BI-POLYMER NANOPARTICLE PREPARATION	70

6.4 EXPERIMENTAL DEMONSTRATION AND OPTICAL CHARACTERIZATION RESULTS	74
CHAPTER 7.....	90
CONCLUSION	90
BIBLIOGRAPHY	92

List of Figures

Figure 2.1. Chemical structure of a polyfluorene backbone with functional groups R attached at the 9 th position.	8
Figure 2.2. Energy-minimized 3D structure of cyclodextrin-threaded polyrotaxane with poly(para-phenylene) (β -CD-PPP) and its chemical structure[].	9
Figure 2.3. Cartoon representation of the process flow for the reprecipitation method of polyfluorene with the chemical structure of the polymer given at the bottom.....	10
Figure 2.4. a) Preparation of the solid polymer nanoparticle dispersion in water. b) Polymer blend preparation from a dispersion containing nanoparticles of two different polymers, or by using dispersions that contain both polymers in each individual nanoparticle [43].	12
Figure 2.5. TEM images of different biphasic blend particles with percentages of the amounts employed in the preparation given. The particles are deposited on a carbon-coated copper grid and left to dry under air. The samples are not further labeled or stained [50].	12
Figure 2.6. (a) Structural formula of P3DDUT, (b-g) SEM images of nanoparticles prepared by reprecipitation method and dynamic light scattering (DLS) size distributions, (b,e)) 0.1 wt.-% P3DDUT/THF at 20°C, (c,f) 1.0 wt.-% P3DDUT/THF at 20°C, (d,g) 1.0 wt.-% P3DDUT/THF at 80°C [44].	14
Figure 2.7. (a) Absorption and (b) fluorescence spectra of P3DDUT nanoparticles, with various mean diameters, dispersed in water [44]......	14
Figure 2.8. (a) Normalized absorption and (b) normalized fluorescence spectra of conjugated polymer nanoparticles (solid line) compared to polymers in THF solutions (dashed line). (c) Photo of various polymer nanoparticle dispersions under UV radiation [49].	15
Figure 3.1. Wurtzite crystal structure of a CdSe quantum dot, where purple spheres indicate cadmium atoms and green ones selenium atoms.	17
Figure 3.2. (a) Cross-sectional view of a silica shell capped CdSe/ZnS nanocrystal, and (b) chemical compounds used for the silanization of NCs. The outer surface of the silica shell is further functionalized with phosphonate and thiol groups [53].	18

Figure 3.2.1. A picture of CdTe nanocrystal synthesis setup. Precursors are produced in the main flask (left) and Al_2Te_3 source is activated in the small three-necked flask (right).	22
Figure 3.2.2. (onset) Normalized photoluminescence spectra of our CdTe NCs emitting at different wavelengths which correspond to different boiling durations. (inset) A photo of our CdTe nanocrystals emitting in different colors depending on the size distribution.....	23
Figure 4.1. (Left) The Lycurgus cup when light is shine from the outside (reflection), and (right) when light is shine from the inside of the cup (absorption).	25
Figure 4.2. Schematic representation of surface propagating and localized plasmons on nanostructured gold surfaces [76].	27
Figure 4.1.1. Schematic representation of electric field which is created by an incident wave and corresponding shift of electron cloud resulting in a plasmon resonance of the particle [].	31
Figure 4.1.2. Electric field distribution of 15 nm Au metal nanoparticles at an incident planewave radiating at 520 nm, which (a) propagates along the x-axis and is polarized along the y-axis, and (b) propagates along the y-axis and is polarized along the x-axis	33
Figure 4.1.3. Scattered light intensities for silver nanoparticles with their corresponding high-resolution TEM images. Particles having spherical shape peak at the blue region, pentagon-shaped particles appear green, and triangular-shaped particles appear red [91].	36
Figure 5.1.1 (left) Schematic representation of the experimental setup using a scanning probe method. (right) Fluorescence enhancement factor (red curve), lifetime (brown curve) of terrylene for varying sample-particle separations [95].	41
Figure 5.1.2. (a) Cartoon picture of the hybrid nanostructure composed of Au nanorods, silica shell and dye molecules, (b) Chemical structure of the dye oxazine 725, (c) SEM image of only Au nanorods, (d) TEM image of the core-shell nanostructures [99].	42
Figure 5.1.3. Electric field intensity maps obtained from FDTD simulations on a single Au nanorod core/silica shell structure, where the nanorod is aligned vertically. The excitation polarization of the incident light relative to the nanorod length axis is 0° , 15° , 30° , 45° , 60° , 75° , and 90° , respectively [99]...	42
Figure 5.1.4. (a) Schematic of the hybrid nanostructure composed of Au core/dye-doped silica shell, (b) TEM image of Au core, (c) SEM image of gold/dye-doped silica core/shell nanoparticles, and (d) spaser mode with $\lambda = 525$ nm and $Q = 14.8$, where inner and outer circles are representative of the core and shell boundaries [100].	43

Figure 5.1.5. Normalized extinction (1), excitation (2), spontaneous emission (3) and stimulated emission (4) curves of Au/dye-doped silica nanoparticles [100].	43
Figure 5.2.1.1 A sample of dark red, colloidal synthesized gold nanoparticles dispersed in aqueous medium.....	47
Figure 5.2.1.2 Principal procedure for the formation of gold-silica core/shell nanostructures. (a) Formation of monodisperse citrate capped gold nanoparticles, (b) surface modification by use of APS which forms as a monolayer, and (c) deposition of silica shell by polymerization of active silica on the pre-coated silanized gold surface.	48
Figure 5.2.2.1 (Onset) Normalized numerical and experimental absorption spectra of 15 nm-colloidal Au NPs dispersed in water. (Inset) FDTD simulation and experimental data of real and imaginary parts of the permittivity constant of Au adopted from Johnson and Christy [].	50
Figure 5.2.2.2 (a)-(f) Transmission electron micrographs of only Au NPs with average diameter being 15 nm, and Au core/silica shell nanoparticles with average shell thickness varying from 3, 6, 16, 19, 22 nm, respectively. The silica shell thicknesses are controlled and tuned by varying synthesis conditions.....	53
Figure 5.2.2.3. Absorbance spectra of samples given in Figures 5.1.2.2 a)-f) to monitor shifts in the surface plasmon resonance peaks because of increasing silica thickness. The SPR band for only Au NPs appears at 518 nm.	54
Figure 5.2.2.4 Flow diagram for the decoration of APS functionalized Au/SiO ₂ core/shell nanoparticles with water-soluble CdTe NCs.	55
Figure 5.2.2.5. Transmission electron micrograph of hybrid Au/SiO ₂ /CdTe-NC nano-assembly (onset), schematic representation of this hybrid structure (inset).	55
Figure 5.2.2.6. Absorbance spectrum of colloidal synthesized CdTe NC in water.	56
Figure 5.2.2.7. Spectral overlap between NCs and Au NPs for maximum plasmon-exciton coupling interactions. Absorbance and PL intensities are normalized.	57
Figure 5.2.2.8. PL spectra of our CdTe NCs alone (blue curve), and those in the presence of Au NPs with and without a dielectric spacer made of a silica shell. The red curve indicates a 5.2-fold quenching due to the lack of a silica shell... ..	58
Figure 5.2.2.9. Time resolved PL decays of our CdTe NCs alone (blue curve) and those in the presence of Au NPs (red curve) and in the presence of Au NPs and a dielectric spacer shell. Corresponding fitted curves are indicated in black.	59
Figure 5.2.2.10. Calculations of normalized decay rates using computational FDTD method, and analytical method [] in different orientations of dipole polarization to investigate the effect of particle-dipole separation.	62

Figure 5.2.2.11. (Top) Perpendicular and (bottom) parallel polarization orientations of the dipole emitter with respect to the Au surface.....	63
Figure 5.2.2.12. Simulation results of enhancement factors in relation to varying particle-dipole separations by using a silica shell for parallel orientation (square) and perpendicular orientation (disc).....	64
Figure 5.2.2.13. Particle diameter dependence of the simulated enhancement factors at perpendicular orientation for 2 nm (square) and 5 nm (disc) dipole-particle separation using a silica shell.	66
Figure 6.3.1 Synthesis of poly(9,9-dihexyl-9H-fluorene) using 2,7-dibromo-9,9-dihexyl-9H-fluorene and 9,9-dihexylfluorene-2,7-bis(trimethyleneborate) as the monomers.	70
Figure 6.3.2 Chemical structure of poly[2-methoxy-5-(2'-ethyl-hexyloxy)-1,4-phenylene vinylene] (MEH-PPV) purchased from Sigma-Aldrich	71
Figure 6.3.3. Schematic representation of the proposed nanostructures for polymer nanoparticles formed from PF and MEH-PPV via the reprecipitation method. (a) System 1: (PF NP + MEH-PPV NP), (b) System 2: (PF + MEH-PPV) mixed NPs, (c) System 3: (PF/MEH-PPV) sequential NPs, and (d) System 4: (MEH-PPV/PF) sequential NPs [].	73
Figure 6.3.4. SEM micrographs of films prepared from (a) PF solution, (b) PF NP dispersion (c) MEH-PPVa NP dispersion, and (d) (MEH-PPVa/PF) sequential NP dispersion. The last image is taken with a tilt angle of 15° [22].	74
Figure 6.4.1. Onset: Emission spectra of PF solution and its corresponding PF NP dispersion, MEH-PPVa solution and its corresponding MEH-PPVa NP dispersion, and MEH-PPVb solution and its corresponding MEH-PPVb NP dispersion. Inset: Absorption spectra of PF solution and PF NP dispersion, MEH-PPVa solution and MEH-PPVa NP dispersion, and MEH-PPVb solution and MEH-PPVb NP dispersion.	75
Figure 6.4.2. Onset: Emission spectra of solutions of PF, MEH-PPVa, MEH-PPVb, (PF + MEH-PPVa) and (PF + MEH-PPVb) at absorption maximum of PF (solid) and absorption maximum of MEH-PPV (dotted). Inset: Absorption spectra of PF, MEH-PPVa, MEH-PPVb, (PF + MEH-PPVa), and (PF + MEH-PPVb) solutions.	77
Figure 6.4.3. Onset: Emission spectra of PF NP, MEH-PPVa NP, MEH-PPVb NP dispersions and their corresponding mixtures in a 1:1 ratio as (PF NP + MEH-PPVa NP) and (PF NP + MEH-PPVb NP) at absorption maximum of PF (solid) and MEH-PPV (dotted), respectively. The concentration of each species in the NP mixtures is reduced by a factor of two due to mixing. Inset: Absorption spectra of PF NP, MEH-PPVa NP, MEH-PPVb NP dispersions and their mixtures in a 1:1 ratio, (PF NP + MEH-PPVa NP) and (PF NP + MEH-PPVb NP).	80

Figure 6.4.4. Onset: Emission spectra of (PF + MEH-PPVa) and (PF + MEH-PPVb) mixed NPs at absorption maximum of PF (solid) and MEH-PPV (dotted). Inset: Corresponding absorption spectra of (PF + MEH-PPV) mixed NPs.	81
Figure 6.4.5. Onset: Emission spectra of PF NPs, (PF/MEH-PPVa) sequential NPs at absorption maximum of PF (solid) and MEH-PPV (dotted), and (PF/MEH-PPVb) sequential NPs at absorption maximum of PF (solid) and MEH-PPV (dotted) Inset: Absorption spectra of PF NPs and (PF/MEH-PPV) sequential NPs.	84
Figure 6.4.6. Biexponentially fitted decay curves of PF NPs at 429 nm (0.26 ns), MEH-PPVa NPs at 589 nm (0.51 ns) and (PF/MEH-PPVa) sequential NPs at 429 nm (0.20 ns) and 566 nm (1.22 ns). Reported lifetimes are average intensity weighted values and decay fit parameter “R” ranges from 0.8 to 1.2.	85
Figure 6.4.7. a) Onset: Emission spectra of MEH-PPV NPs, (MEH-PPVa/PF) sequential NPs at absorption maximum of PF (solid) and MEH-PPV (dotted). Inset: Absorption spectra of MEH-PPV NPa and (MEH-PPVa/PF) sequential NPs. b) Onset: Emission spectra of MEH-PPVb NPs, (MEH-PPVb/PF) sequential NPs at absorption maximum of PF (solid) and MEH-PPV (dotted). Inset: Absorption spectra of MEH-PPVb NP and (MEH-PPVb/PF) sequential NPs.	87
Figure 6.4.8. Biexponentially fitted decay curves of PF NPs at 429 nm (0.26 ns), MEH-PPVa NPs at 589 nm (0.51 ns) and (MEH-PPVa/PF) sequential NPs at 425 nm (0.17 ns) and 561 nm (0.90 ns). Reported lifetimes are average intensity weighted values and decay fit parameter “R” ranges from 0.8 to 1.1.	88

List of Tables

Table 5.2.2.1. Comparison of the decay lifetimes and rates, calculated and experimental enhancement factors for the CdTe NCs with and without Au nanoparticles.....	60
---	----

To Tuncay...

Chapter 1

Introduction

In the last few decades science and nanotechnology have attracted wide-scale interest to a large extent, which gave rise to the development of numerous synthesis, fabrication, and characterization techniques together with a large variety of chemical compositions used in these nanostructures compared to the conventional chemical methods. These discoveries brought along more important contributions of this fascinating field, while materials at the micrometer scale mostly display properties that are the same as those of the bulk form, their nanoscale versions exhibit a lot more distinctive properties compared to the bulk [1]. A special class of these nanomaterials, which gained increasingly more attention thanks to their extraordinary electrical and optical characteristics, is semiconductors.

An increasing awareness of the necessity to save energy has directed scientific research to develop various materials and techniques for use in lighting and displays applications. In this context, polymer light-emitting diodes promise great potential to replace the traditional light sources because of their significant economical and technological advantages in energy saving [2]. Because of their versatility and superior optical properties, conjugated polymers are on their way to earning an irreplaceable position for use in white light generation though phosphors have thus far been most extensively used for white light applications [2,3,4,5]. Conjugated polymers possess inherent advantages over other photo-

emitters such as high absorption coefficients and feature high solid-state photoluminescence quantum efficiencies [2,6]. Also, with conjugated polymers, an almost unlimited number of chemical modifications are possible, resulting in more easily processed, custom tailored, and functional materials. Furthermore these materials can be coated using very low-cost techniques. Till date, a wide range of conducting polymers have been investigated and implemented in device application for solid-state lighting application [3,7,8,9,10,11,12,13,14,15,16]. Among them, polyfluorenes, a special class of electro- and photoactive polymers, received particular interest because of their unusual properties including an emission color span through the entirety of the visible spectrum, high fluorescence quantum efficiency, ease of processability, good thermal stability and low operating voltages as active materials in light-emitting diodes [17,18]. The listed advantages offered by polyfluorenes over other alternative light emitters make this polymer family an ideal candidate for device implementation including LEDs, photovoltaic cells, and full color displays [2,3,7,8,17,19].

Förster resonance energy transfer (FRET) is an important proximity phenomenon, which is also effective among different polymer species. In this energy transfer mechanism different from the radiative energy transfer, the excitation energy of the donor polymer is non-radiatively transferred to the acceptor polymer molecules by coupling of the donor emission to the excitation of the acceptor [20,21]. The extent to which the energy transfer can be realized between two emitting species is of crucial importance for the physical aspects of fluorophore-embedded photonic applications. In this work, we combine two different conjugated polymers, namely polyfluorene as the donor and poly[2-methoxy-5-(2'-ethyl-hexyloxy)-1,4-phenylene vinylene] (MEH-PPV) as the the acceptor, in four different nanoparticle systems to analyze energy transfer mechanisms taking place among them. We report on the steady-state and time-resolved photoluminescence properties of these bi-polymer systems interacting

with each other via FRET and analyze consequent modifications of their emission kinetics [22].

Another highly attractive field of interest is the light generation and harvesting from colloidal semiconductor nanocrystals (NCs) for their potential use in different applications such as solid-state lighting, photovoltaics, and bio-labeling [23,24,25]. Due to the quantum size effect, which determines the electro-optical properties of these nanostructures, their emission/absorption wavelengths can be effectively tuned by controlling their size during the synthesis. This property provides NCs with sufficient flexibility of spectral tuning for a broad variety of applications ranging from the near-UV to near-IR. Together with the size effect, also variation of chemical composition makes it possible to tune the emission of NCs over wide spectral ranges. For several years, nanocrystals have been used in diverse context and application, ranging from photovoltaic device to biosensors and in diverse architecture from hybrid architectures including polymers to nucleotides because of their easily modifiable ligands. In most of the listed applications, including light generation and harvesting, the utilization of highly efficient NC emitters is of vital importance. Unfortunately, the quantum efficiency of colloidal NCs highly decreases upon film formation [26]. To address this problem, the recently growing field of metal-enhanced fluorescence using plasmon coupling to these NC emitters can be applied to achieve a substantial increase in the resulting fluorescence quantum efficiency of NCs in film. Through the use of plasmon coupling, the emission characteristics of excited NCs are modified via enhanced electric field localization created nearby the NC emitters. Since the emission properties of nanocrystals can be changed by surface plasmons generated at the surface of metal nanoparticles, significant changes are observed in the radiative and non-radiative decay rates of the NC photoluminescence. Nanocrystal emission can be enhanced (quenched) via plasmonic coupling as a result of the increase in the radiative (non-radiative) decay rates under certain conditions. To target emission enhancement of NCs, the particle-emitter separation is very essential as well as

the spectral match between plasmon resonance wavelength of metal nanoparticles and emission wavelength of nanocrystals.

As described above, to achieve enhancement of CdTe NC emission we made use of plasmonic coupling to NC emission in hybrid nanoassemblies made of NC decorated core/shell Au-silica nanoparticles. The use of plasmonics, in the form of stained glasses, dates back to the 4th century (A.D.) with the famous Lycurgus cup, which is made for decorative purposes [27]. Interestingly, due to nanosized metal, the cup looks green when illuminated from outside, but red when illuminated from the inside. It took many years to fully discover the underlying physical principles causing this phenomenon. It was only in the 19th century, when Faraday explained the mystery of the Lycurgus cup [28]. In the beginning of the 20th century Mie solved the Maxwell equations for spherical particles to present their extinction properties at different sizes of the spheres [29]. Many years later, the field of plasmonics reached its maturation with its physical properties being fully understood to further open up new horizons towards the exploitation of these nanostructures in complex photonic device applications. Now with the recent discoveries in nanotechnology, there has been a great deal of interest and progress in the investigation of the photo-physical properties of surface plasmons like in the case of metal-enhanced fluorescence, surface-enhanced Raman spectroscopy, plasmon-enhanced nonlinear optical processes, and plasmon-mediated two-photon absorption [30 31 32 33].

Our research interest mainly focuses on the understanding and the development of highly efficient emitters/absorbers using energy transfer mechanisms. We are especially interested in two main mechanisms: the plasmon coupling of Au nanoparticles to NC emitters to facilitate increase in quantum efficiency, and the Förster resonance energy transfer between two conjugated polymers in four different bi-polymer systems.

In Chapter 1, we present a brief introduction on the nanostructures used in our studies including polymer nanoparticles, colloidal semiconducting nanocrystals, and plasmonic gold nanoparticles. The importance and the application fields of these materials in today's research are explained with some examples. This chapter is a brief overview of the problems faced with the current state-of-the-art technology and the solutions offered by our nanosystems to solve these problems by using mechanisms including FRET and plasmon coupling.

In Chapter 2, we introduce polyfluorenes, which are a class of electro- and photoactive polymers, which are highly attractive due to their high efficiencies and ease of applicability in devices.

Next, in Chapter 3, we describe the size dependent optical properties of nanocrystals with their applications in the literature. Also discussed is the dependency of NC emission on various other factors including composition and environment. The synthesis procedure is given for CdTe NCs along with their optical characterization results.

In Chapter 4, we give background on the fundamentals of surface plasmons. The basics of localized plasmons and surface propagating plasmons are introduced with extensive discussion on the optical properties of metal nanoparticles including size, shape, composition, and environment dependency.

Chapter 5 is devoted to numerical simulation results together with optical data for the realization of plasmonic coupling of Au NPs to CdTe NCs in hybrid core/shell nano-architectures for enhancement of NC emission in aqueous medium. Calculations are performed at various particle-dipole separations and experimental results are obtained for varying silica shell thicknesses. We present our results showing emission enhancements NC emission at the same time along with a shortening in the fluorescence decay lifetimes.

In Chapter 6, we show the extensive study of modified emission kinetics of different bi-polymer nanoparticle systems, which provide the possibility of targeting desired optical properties for future use in device applications. Significant emission enhancement is obtained for core-shell polymer nanoparticles, which are a result of the FRET mechanism involved in these nanostructures.

Finally, in Chapter 7 we conclude our study by making short remarks on our major contributions in the related fields and the impacts of our results, which render this work important. Also shortly mentioned will be the future prospects of our research work in this field.

Chapter 2

Fluorescent Conjugated Polymers

2.1 Polyfluorenes: A Novel Class of Light Emitting Polymers

Polyfluorenes (PFs) are a wide class of electroactive and photoactive polymers, which have exceptional chemical, physical and optoelectronic properties. In the past few years, research in this field has reached a saturation point because of a number of various unusual properties including an emission color span through the entirety of the visible spectrum, high fluorescence quantum efficiency, ease of processability, good thermal stability and low operating voltages as active materials in light-emitting diodes (LEDs). Improved optical and electrical properties together with certain chemical modifications can be achieved by attachment of different side chains to the fluorene backbone at the 9th position [34]. The listed advantages offered by polyfluorenes over other alternative light emitters make this polymer family an ideal candidate for device implementation including LEDs, photovoltaic cells, full color displays, etc [2 3 7 8 17 35]. For use in such devices, however, it is necessary to deposit solutions of π -conjugated polymers onto solid substrates, typically by spin-coating, dip-coating, or drop-coating.

After the discovery of the electroluminescence of organic compounds by Bernanose in 1953, who performed studies on dyes including gonacrin, brilliant acridine orange E and carbazole, many different classes of conjugated polymers like poly(p-phenylene) (PPP), polythiophene (PT) and polyfluorene (PF) have been synthesized, investigated and further developed for applications in solid-state lighting till date [18 36]. Although PPPs offer a number of benefits like chemical stability and large bandgap for blue light emission, there are certain drawbacks such as the insolubility of PPPs in common organic solvents, causing a significant reduction in the processability of the polymer. The solubility of PPPs has been increased by introduction of bulky alkyl chains to the phenylene units; however these chains lead to the destruction of conjugation, because of the enforcement of steric strains. PFs, on the other hand are molecular compounds with pairs of phenylene rings locked into a coplanar arrangement by the carbon atom at the 9th position as shown in Fig. 2.1 [37]. Functionalization of the backbone at that particular C-9 position for enhancement of solubility causes no change in the high fluorescence quantum yields and high degree of brightness.

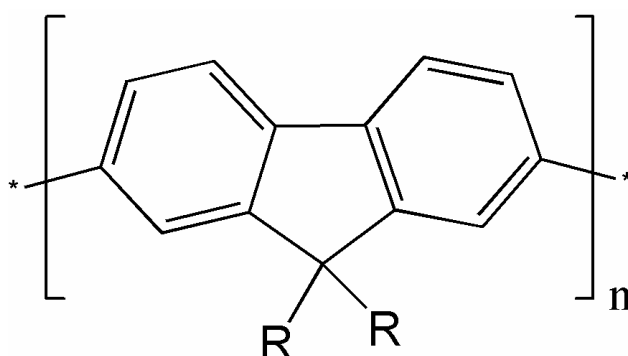


Figure 2.1. Chemical structure of a polyfluorene backbone with functional groups R attached at the 9th position.

On-going research has, however, shown, that PFs lack spectral stability which is verified by a change in the blue emission to a greenish-blue broad band emission. This is basically attributed to chemical structure changes in form of

keto defects by thermo-, photo- or electro-oxidative degradation. Another mechanism leading to significant changes in the emission properties of π -conjugated polymers is the physical aggregation observed especially in film form. Deposition of solutions of π -conjugated polymers by spin-coating or drop-casting onto solid substrates results in electronic coupling of polymer chains (interchain interaction), which is essential for charge carrier transport in the film state. The presence of interchain coupled states may induce an efficient energy transfer from higher energy intrachain singlet excitons to lower lying eigenstates that are delocalized over several polymer chains in intimate contact with each other through dispersive relaxation processes. In fact, the aggregate-induced depopulation of the initially excited intrachain excitons results in a red-

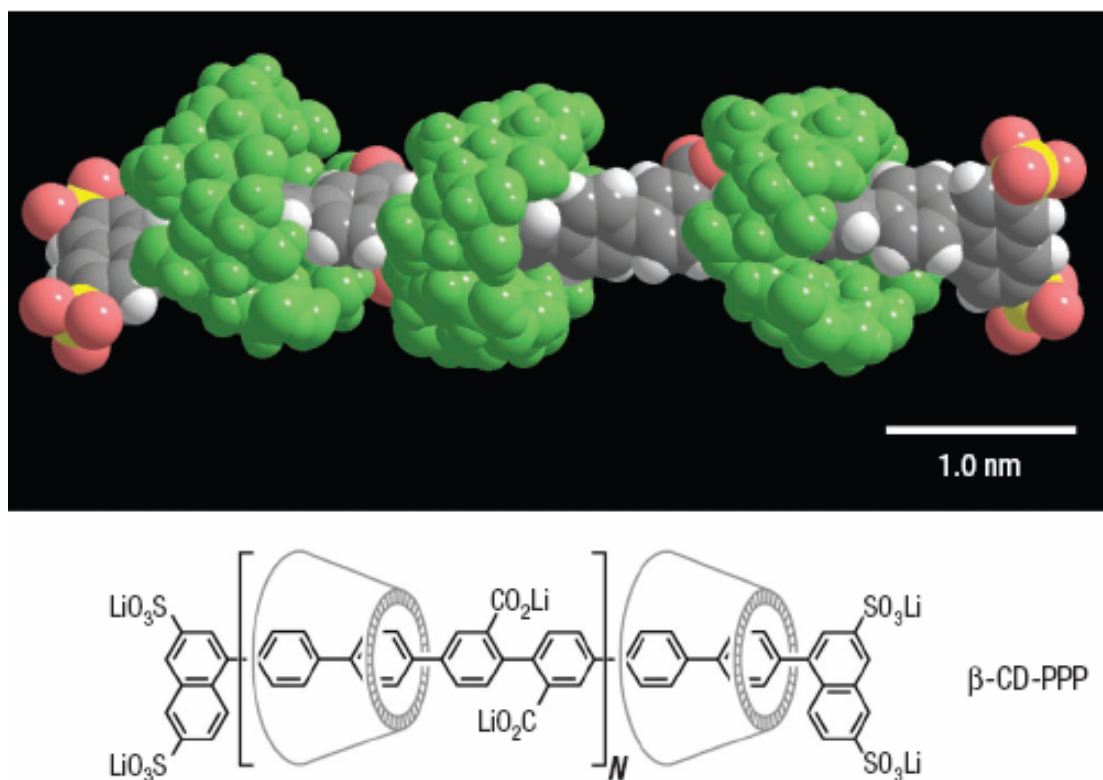


Figure 2.2. Energy-minimized 3D structure of cyclodextrin-threaded polyrotaxane with poly(para-phenylene) (β -CD-PPP) and its chemical structure[38].

shifted emission band, which is also associated with a significant reduction in the fluorescence quantum efficiency (Φ_{PL}) in film state in the order of 50% [39]. To address this problem faced in films of conjugated polymers, which are essential for device applications, some researchers have developed various isolation techniques like rotaxation (Fig. 2.2) [38], blending of various polymer structures and introduction of bulky dendrimer side groups to the polymer network [40]. These changes are supposed to reduce stacking interactions among molecules which may otherwise lead to significant quenching of the photoluminescence intensity in polymers.

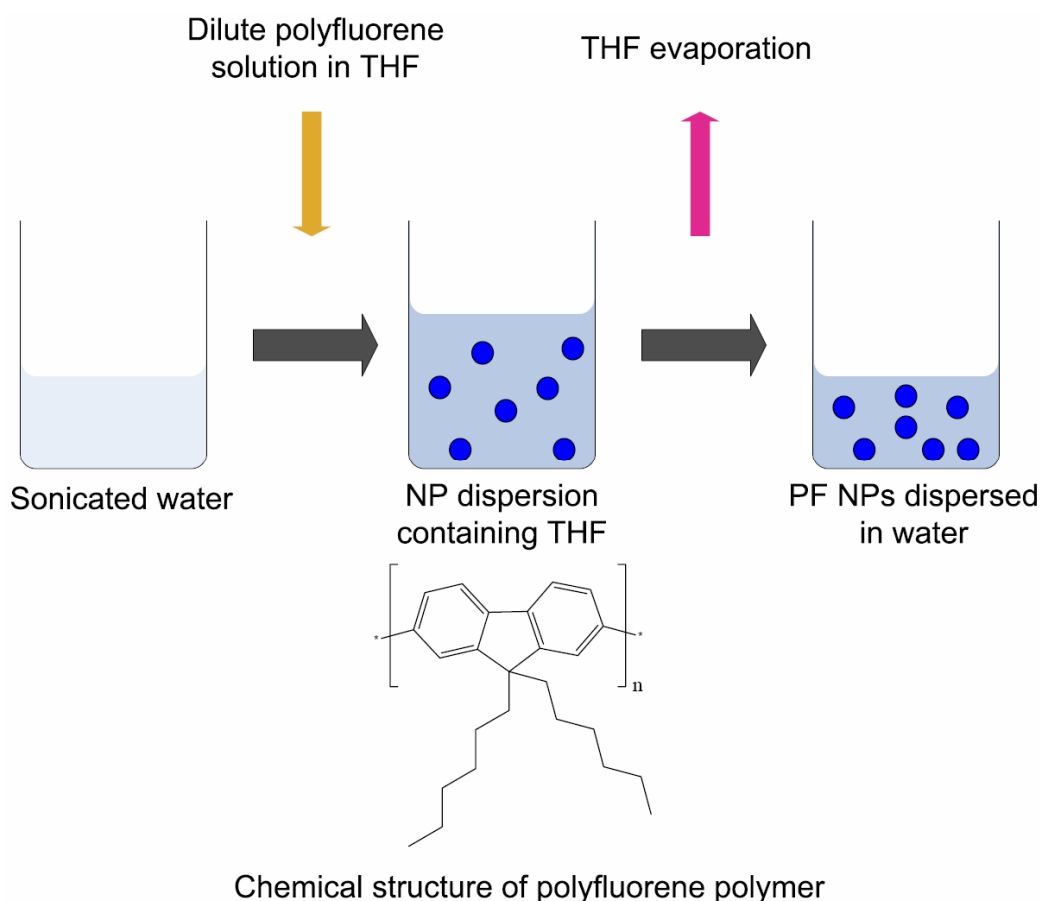


Figure 2.3. Cartoon representation of the process flow for the reprecipitation method of polyfluorene with the chemical structure of the polymer given at the bottom.

A recently newly developed approach for the processing of conjugated polymers for potential use in device applications is the formation of organic nanoparticles from π -conjugated polymers [41,42,43,44,45,46]. Various methods have been proposed for the formation of organic nanoparticles including mini-emulsion process, hydrothermal synthesis, and reprecipitation methods (Fig. 2.3) [42,43,44,45,46,47,48,49]. By making use of the mini-emulsion approach, Scherf and coworkers reported that polymer layers can possess improved performance in a multi-component phase-separated morphology. Adjustment of optical and electro-optical properties is achieved by blending two individually prepared nanoparticle dispersions of different copolymers. Nanoparticles, containing both copolymer components, were prepared by mixing first the copolymer solutions and then forming the micro-emulsion as is depicted in Fig. 2.4 [43]. Though in their study in 2003 Scherf and coworkers believed that the blend nanosphere was composed of two randomly mixed polymers in each particle, it was later discovered that these particles were in fact two-component phase-separated particles with each side consisting of a different polymer as revealed by TEM images given in Fig. 2.5 [50]. In this method a water-immiscible solvent is used for the stock solution preparation of the copolymers. Also, the use of a surfactant is required by which the formation of the nanoparticles is stabilized as illustrated in Fig. 2.4 below.

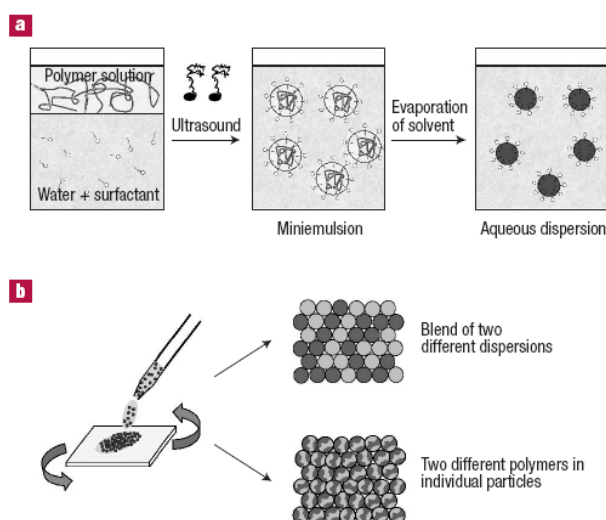


Figure 2.4. a) Preparation of the solid polymer nanoparticle dispersion in water. b) Polymer blend preparation from a dispersion containing nanoparticles of two different polymers, or by using dispersions that contain both polymers in each individual nanoparticle [43].

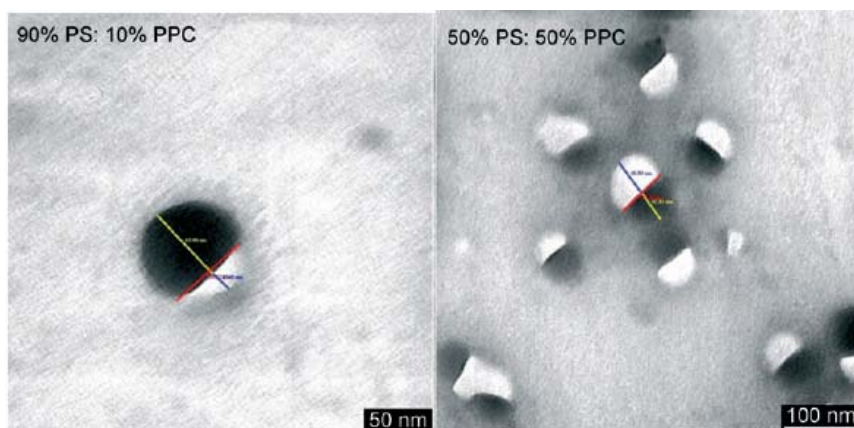


Figure 2.5. TEM images of different biphasic blend particles with percentages of the amounts employed in the preparation given. The particles are deposited on a carbon-coated copper grid and left to dry under air. The samples are not further labeled or stained [50].

This approach allows for the preparation of novel nanoscale structures to be further processed as thin polymer films with novel optical properties.

Among the above listed methods, especially attractive is the reprecipitation method, because of its simplicity and versatility [39]. This method is applied by reprecipitation of a polymer solution into a poor solvent such as water under sonication, followed by vacuum evaporation of the good solvent inside the dispersion [48]. This method was first developed by Kasai et al., who also performed studies revealing the size-dependent optical properties of perylene nanoparticles. Depending on decreasing diameters of the particles, they observed blue-shifts in both the absorption and the fluorescence spectra related to the shortened conjugation length of particles varying from diameters of hundreds to tens of nanometers. The proposed mechanism for the increased

bandgap was a change in lattice state resulting from an increase in surface area, which reduces the Coulombic interactions between molecules [48].

Polymer nanoparticles are found to exhibit size-dependent properties as has been stated by Kurokawa and coworkers who have recorded blue-shifting absorption and emission spectra as the nanoparticle diameters were reduced from 420 to 40 nm. This observation was explained by a difference in polymer conformations and spatial arrangements. Also a lattice softening of the nanoparticles is believed to be responsible for the size-dependent properties in poly(3-[2-(N-dodecylcarbamoyloxy)ethyl]-thiophene-2,5-diyl) (P3DDUT) nanoparticles as is demonstrated in Fig. 2.6 [44,48].

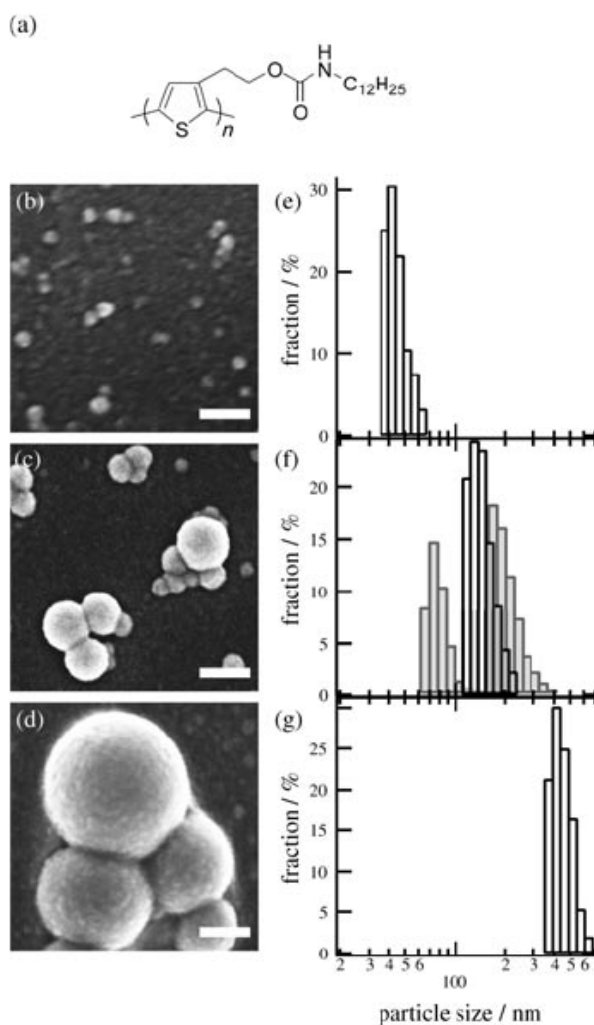


Figure 2.6. (a) Structural formula of P3DDUT, (b-g) SEM images of nanoparticles prepared by reprecipitation method and dynamic light scattering (DLS) size distributions, (b,e)) 0.1 wt.-% P3DDUT/THF at 20°C, (c,f) 1.0 wt.-% P3DDUT/THF at 20°C, (d,g) 1.0 wt.-% P3DDUT/THF at 80°C [48].

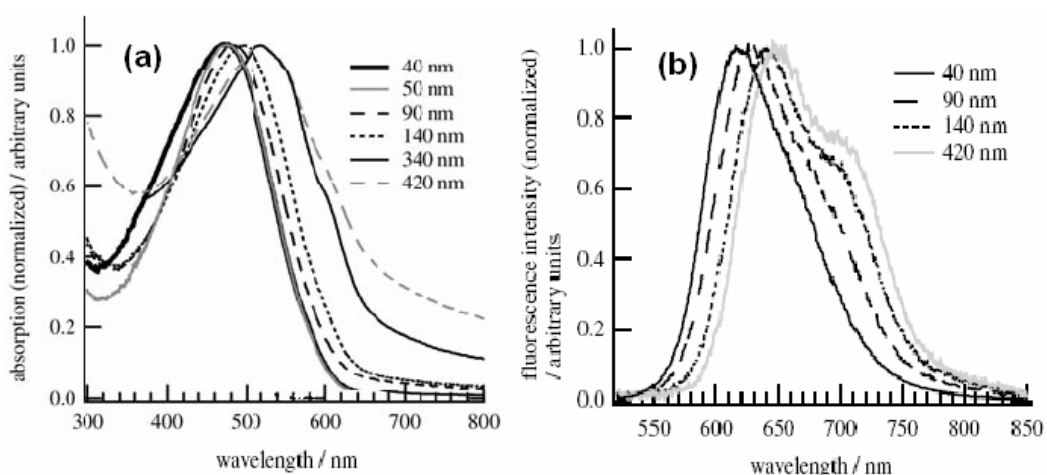


Figure 2.7. (a) Absorption and (b) fluorescence spectra of P3DDUT nanoparticles, with various mean diameters, dispersed in water [44].

Another study conducted by McNeill and coworkers includes the preparation and characterization of nanoparticles formed by the reprecipitation of polymer poly(9,9-dioctylfluorene) (PFO), [9,9-dioctyl-2,7-divinylene-fluorenylene]-alt-co-{2-methoxy-5-(2-ethylhexyloxy)-1,4-phenylene} (PFPPV) and poly[2-methoxy-5-(2-ethylhexyloxy)-1,4-phenylenevinylene] (MEH-PPV), recording a quantum yield of 10% [49]. They report a blue-shift for the absorption spectra but a red-shift for the fluorescence spectra of the nanoparticle dispersions of all three polymers with respect to their THF solutions. Fig. 2.8 is a nice illustration of the changes in absorption and fluorescence spectra of nanoparticle dispersions versus solutions of these polymers, which are similar to previous observations of blue-shift in absorption spectra but the reverse effect with a red-shift in fluorescence spectra compared to other groups.

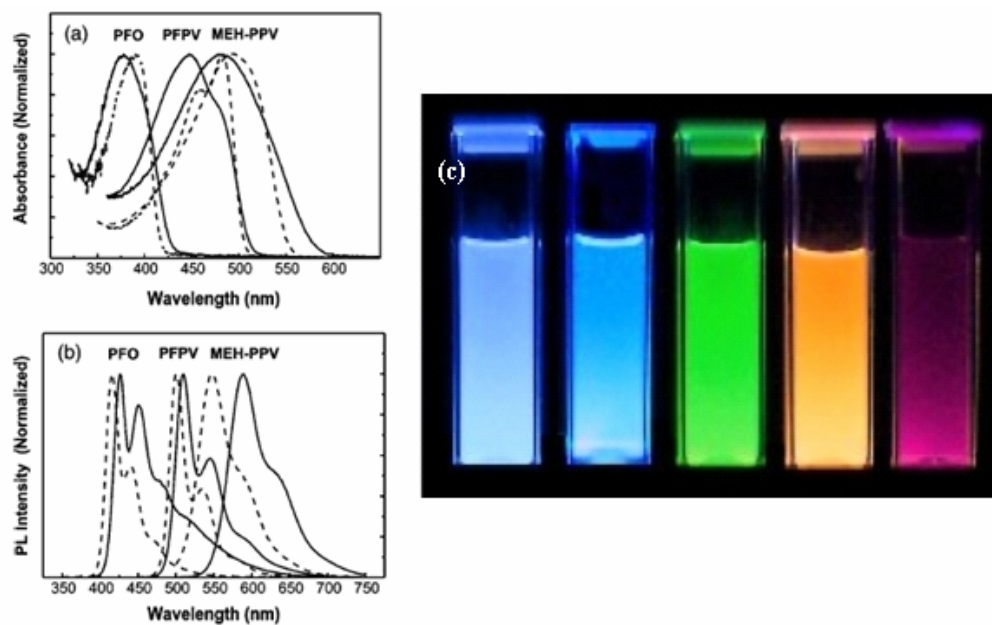


Figure 2.8. (a) Normalized absorption and (b) normalized fluorescence spectra of conjugated polymer nanoparticles (solid line) compared to polymers in THF solutions (dashed line). (c) Photo of various polymer nanoparticle dispersions under UV radiation [49].

These results reveal the compact conformation that causes increased interactions between polymer chains. The fluorescence quantum yield for the PFPV nanoparticles suspended in water is found to be 0.1.

Chapter 3

Semiconductor Nanocrystals

The development of synthesis methods to produce semiconducting colloidal quantum dots (QDs) led to an immense growth in research in this field over the past several decades because of the exciting optical and electrical properties of these artificial crystals [51,52,53]. The exploration of various electro-optical features of these nanocrystals (NCs) further induced the rapid expansion of research on the fundamental physics of these nanostructures. For example, one of the defining features of these semiconducting nanocrystals is the quantum size effect, which is a phenomenon caused by the comparable spatial extent of the electronic wavefunction with respect to the particle size, typically in the order of several nanometers [51]. This effect was discovered in the 80s simultaneously in the United States and Russia [54,55]. Consisting of only a few hundred to a few thousand atoms, QDs are typically composed of group II-VI, III-V and IV-VI elements, which allow for the adjustment of the desired emission wavelengths spanning a wide range depending on the type of elements used and the targeted size. Specific types of nanocrystals include CdS, CdSe (Fig. 3.1), ZnS, CdTe, PbS, PbSe, Si and Ge constituting the class of only core nanocrystals. Different from these core structures, there have also been synthesized core/shell nanocrystals such as CdSe/ZnS and CdTe/CdS in which the shell has a wider bandgap [56,57]. This serves for the surface passivation

and, as a result, leads to higher emission rates. The increased emission achieved by using these additional shell structures is a consequence of the charge carrier confinement inside the nanocrystals.

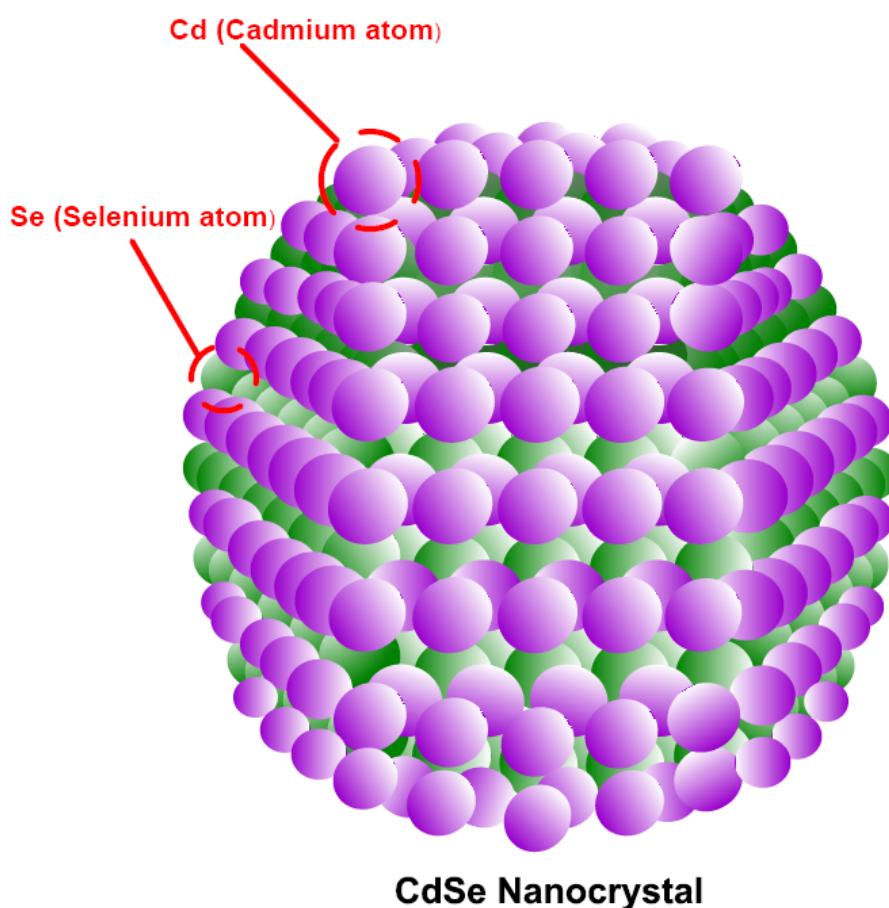


Figure 3.1. Wurtzite crystal structure of a CdSe quantum dot, where purple spheres indicate cadmium atoms and green ones selenium atoms.

Ongoing research makes important progress towards finding new, environment-friendly experimental routes and compounds for quantum dot formation, development of synthesis techniques for better size control and monodispersity, and the integration of these quantum dots into novel structures via surface functionalization (ligand exchange) [53]. Alternative, more environment-friendly synthetic routes have been developed in the recent years for which the

synthesis of water-soluble CdTe NCs can be listed as a nice example compared to its CdSe-like counterparts made by organometallic chemical methods [53]. Of particular interest in this study are these environmentally less harmful CdTe nanocrystals, which are composed of II-VI group atoms.

On the other extreme, in order to make these NCs more bio-applicable, there exist various methods to passivate biomolecules from the potential harms caused by toxic elements like cadmium. One of the methods used in literature is the exchange of the hydrophobic TOPO surface of CdSe/ZnS with a bifunctional molecule that is hydrophilic on one end and binds to ZnS on the other end [53]. For this purpose, one may use thiol (-SH) groups as one end for the ZnS binding while a carboxyl (-COOH) group can be used as the hydrophilic binding group. Very commonly used molecules for these applications are mercaptoacetic acid or mercaptopropionic acid [58,59,60]. Unfortunately, the -SH-ZnS bonds are not as stable as -SH-Au bonds; as a result, these NCs start to precipitate in solution after certain treatment conditions including varying pH. A more difficult but stable chemical route towards the synthesis of biocompatible NCs is the silica capping of CdSe/ZnS NCs as is illustrated in Fig. 3.2 [61,62,63].

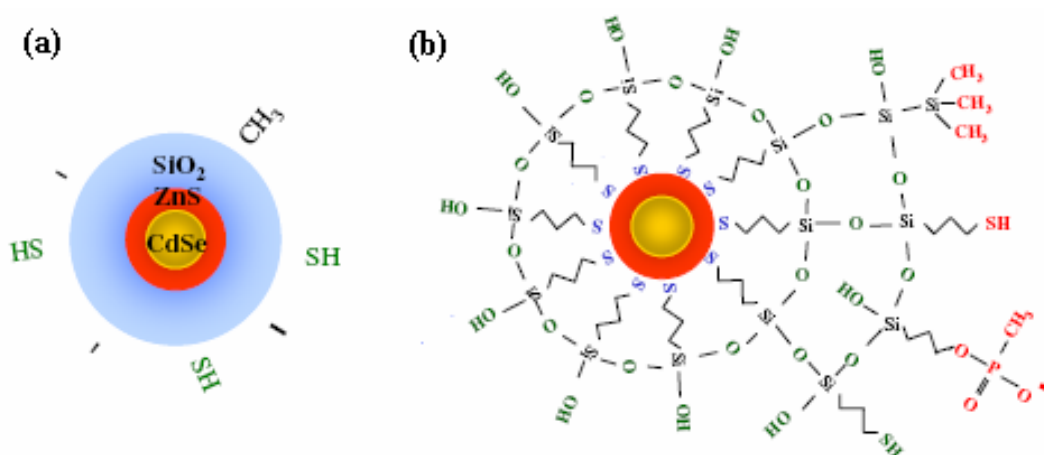


Figure 3.2. (a) Cross-sectional view of a silica shell capped CdSe/ZnS nanocrystal, and (b) chemical compounds used for the silanization of NCs. The outer surface of the silica shell is further functionalized with phosphonate and thiol groups [53].

Further stabilization of these particles is achieved by surface functionalization via various groups that are either negatively or positively charged like phosphonate or ammonium groups [64]. Thereby, particles carry a net charge on their surface, which prevents particle agglomeration in a long term. An even simpler method, however, is the adsorption of biocompatible polymers onto the NC surface through either recognizing head groups or electrostatic interactions between the capping layer of the NCs and the polymer molecules [65]. This can be achieved by the use of polyelectrolyte molecules like poly(allyl amine) (PAA) or polystyrene sulfonate (PSS) depending on the positive or negative nature of the surface charge on the NCs.

3.1 Size and Color Tuning: The Quantum Size Effect

It is worth noting that nanocrystals should be considered different from their bulk forms. In bulk form crystals exhibit more continuous-like energy bands (although the energy levels are indeed discretized due to the finite size of the crystal). Energy levels, however, become more discrete when the quantum size effects come into play via reduction of crystal size to nanoscales, by which electron hole pairs are confined to quasi-zero dimensions [51]. The wavelength control of the emitted light resulting from the excitation of nanocrystals is mainly governed by two factors. The first one is the composition of the nanocrystal; the second is the size. Nanocrystals, which are also commonly termed as ‘artificial atoms’ owing to the resemblance of their discrete energy levels to that of atoms, exhibit highly tunable emission properties. The energy bandgap of nanocrystals can be very precisely set through variation of size during their synthesis. Analogous to a particle-in-a-box model, because of their small size, which is comparable to the de Broglie wavelength of charge carriers,

NCs form discrete quantum energy levels, in which free electrons and holes are trapped in all three dimensions. The more the dimensions of the quantum dot approach the de Broglie wavelength, the more energy is needed to confine the electron-hole within that small volume; as a result emission at shorter wavelengths is observed. The exciton binding energy is given by the following expression in (3.1).

$$E_n = \frac{\hbar^2 n^2}{8mr^2} \quad (3.1)$$

The quantum size effect is the underlying reason for the blue-shifted emission for decreasing nanocrystal dimensions, i.e., for growing nanocrystal diameter we can clearly observe emission peaks towards the red end of the visible spectrum. Specifically, it has been recorded that CdSe/ZnS core/shell NCs emit from 490 to 620 nm, while PbSe and PbS this range changes from 850 nm to 2100 nm [66]. As one of the fascinating properties of NCs, it is thus possible to tune the emission wavelength by variations in size as well as the composition of the quantum dots during synthesis, which make NCs the material of choice for numerous applications. Nowadays NCs find use in optical device electronics like light emitting diodes, diode lasers, storage devices, photodetectors, photovoltaic solar cells, amplifiers, and biosensors [67,68,69,70,71,72].

3.2 CdTe Nanocrystal Synthesis

The water-soluble CdTe nanocrystals are synthesized in our laboratory. The synthetic route used for nanocrystal formation is as follows under the methodology of our collaborators' work [73,74]. First, a solution containing 4.59 g Cd(ClO₄)₂ prepared into 0.2 L Milli-Q water (18.2 MΩ cm⁻¹). Next, a second solution containing 1.31 g of TGA is prepared in 0.3 L water. Both solutions are then mixed so that the total volume of the solution becomes 0.5 L.

Because a basic medium is required for the synthesis of CdTe NCs, the solution pH is set to 12 by drop-wise addition of ca. 30 mL of 1 M NaOH solution under continuous stirring. To prevent any oxidative reactions, the reaction flask is kept under Argon purge and stirring is continued throughout the reaction. In another flask, a 10 mL solution of 0.5 M H₂SO₄ and 15 mL of Milli-Q water are mixed. This solution is further degassed for 20-30 min to ensure complete depletion of the inside oxygen content. In the next step, 0.8 g of Al₂Te₃ is measured in another flask in the glove-box, because of the high tendency of this compound to oxidize under air conditions. To transport the measured Al₂Te₃ in a gaseous state to the main flask again a continuous Ar flow is used, which carries the produced gas through the bridging glassware and should last for 30-40 min. The setup for nanocrystal synthesis in our laboratory is given in Fig. 3.2.1. To start gas formation, 10 mL of the previously prepared H₂SO₄ solution is taken with a syringe, which is then slowly dropped into Al₂Te₃. Right after, the main solution turns into red, then into dark red and finally to black. To finish up the preparation of the pre-cursors, we continue stirring further for 25 min and increase the Ar flow inside the flask. At this point there is no more need for the Al₂Te₃ line, which can be disconnected; instead a condenser is attached to the main flask. Now, the main solution is heated up to 100 °C and NCs start to grow when the solution begins to boil. Depending on the boiling time, as more atoms add to the nucleated crystal, the crystal size becomes bigger and accordingly the emission characteristics change.



Figure 3.2.1. A picture of CdTe nanocrystal synthesis setup. Precursors are produced in the main flask (left) and Al_2Te_3 source is activated in the small three-necked flask (right).

During the first minute of reaction time, the emission obtained from the NCs is blue, which then turns to green and upon further waiting finally to red if the solution is allowed to react for a sufficient time. The reaction is brought to a stop by rapidly cooling the mixture down to room temperature. For further removal of excess solvent and increase of NC concentration, vacuum evaporation may be used. Also, the synthesized colloidal quantum dots are cleaned from remaining impurities by simple filtering and are thereafter size-selectively precipitated by repetitive centrifugation steps. Through this procedure, it is possible to synthesize highly efficient, negatively charged CdTe NCs. Fig. 3.2.2 is a plot of the light emission obtained from variously sized CdTe NCs upon UV illumination.

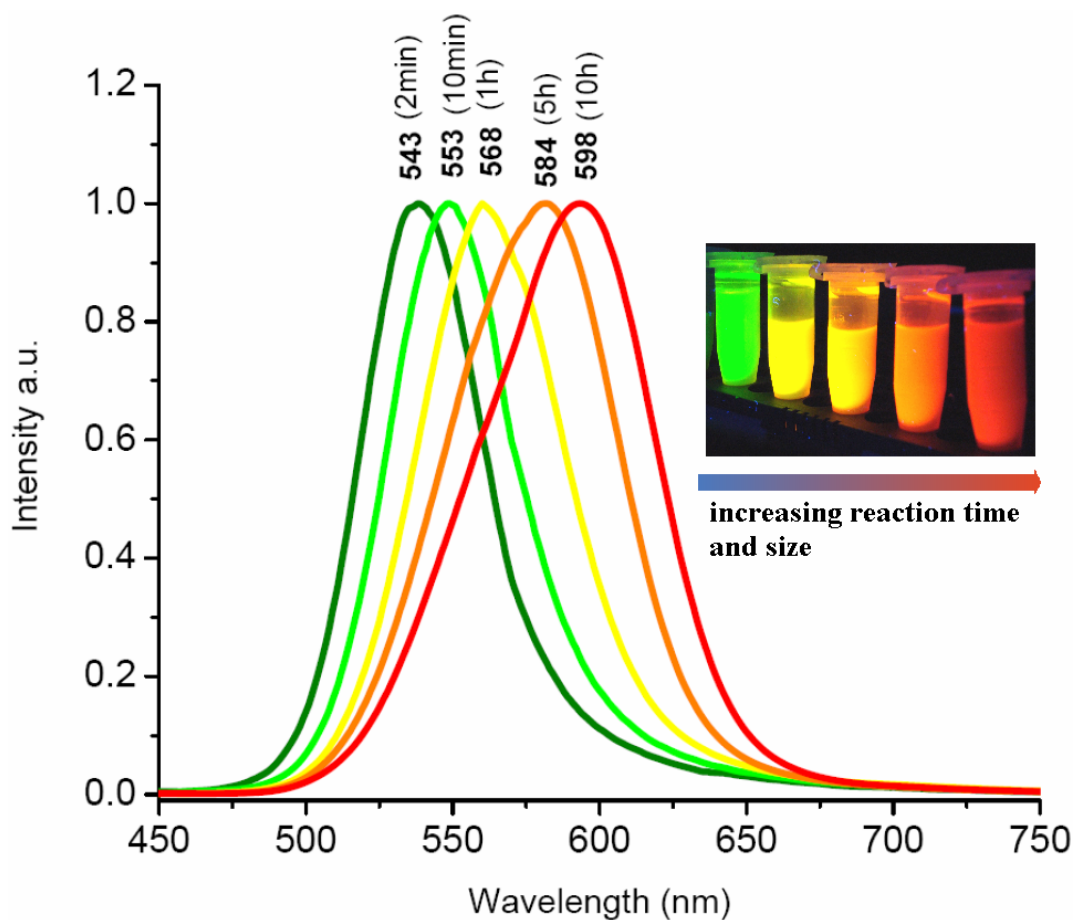


Figure 3.2.2. (onset) Normalized photoluminescence spectra of our CdTe NCs emitting at different wavelengths which correspond to different boiling durations. (inset) A photo of our CdTe nanocrystals emitting in different colors depending on the size distribution.

3.3 Measurement of Fluorescence Quantum Efficiency

The fluorescence quantum efficiency (QE), also known as the fluorescence quantum yield, is a measure of a fluorophore of how much of the incident pump light is transformed into emitted light in photon counts [75]. In other words, it is the ratio of the number of emitted photons to the number of absorbed photons.

To make QE measurements properly, there is a need for a specific reference material with exactly known quantum efficiency value in a certain solvent. Usually, the well known dye Rhodamine 6G in pure ethanol is well suited for NC QE measurements. The highest range of fluorescence quantum efficiency recorded in literature for nanocrystals is around 80%. The excitation wavelength of the fluorophores is chosen at the intersection point of the absorbances of the NCs and the reference dye. At this intersection wavelength both fluorophores are excited using a fluorometer, after which follows a fluorescence emission comparison. The whole underlying area under the fluorescence curve is integrated for both species, where the x-axis is converted from wavelength to energy. Using the efficiency of 95 % for Rhodamine, a relative fluorescence quantum efficiency value is calculated for nanocrystals. Better and more reliable results are obtained if these measurements are taken for multiple NC concentrations and afterwards a best-line is plotted. The fluorescence quantum efficiency of CdTe nanocrystals emitting at 537 nm is typically around 21 % in water.

Chapter 4

Fundamentals of Surface Plasmons

Early observation of the optical effects caused by plasmonic structures date back to the 4th century AD, when Romans utilized the famous historical metal nanoparticle stained cup, the Lycurgus, which is currently exhibited at the British Museum [27].



Figure 4.1. (Left) The Lycurgus cup when light is shine from the outside (reflection), and (right) when light is shine from the inside of the cup (absorption).

Under normal lighting conditions from the outside, the stained cup appears as green, while when illuminated from the inside this cup becomes red in color. This optical phenomenon known as surface plasmon resonance, which was unintentionally discovered at these early times, is effective at structure sizes around 20 times smaller than the wavelength of incident light. Besides the size of the material, what causes this effect is also the material used inside this cup. When light is incident on the cup, the metal and light strongly interact. Free electrons present in the metal structure start to strongly oscillate, generating a screening field so that light cannot pass through but is reflected. This strong oscillation can only be generated at certain frequencies, which are called the material's plasmon resonance frequency. At these specific frequencies light is highly absorbed and reflected, which gives the metal cup its characteristic properties depending on the metal structure size.

Surface plasmons are the collective oscillations of electrons arising at the interface between a dielectric and the conductor metal. There essentially exist two types of plasmons, the localized plasmons (LP) and the surface propagating plasmons (SP) as is illustrated in Fig. 4.2 [76].

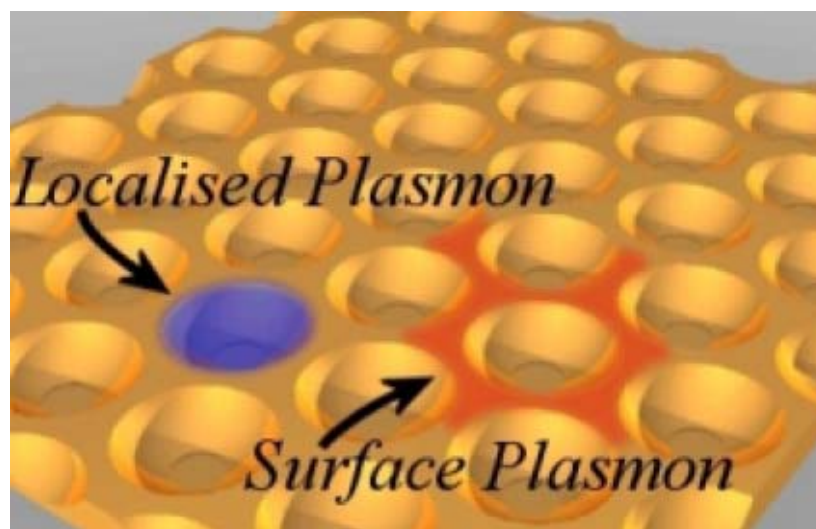


Figure 4.2. Schematic representation of surface propagating and localized plasmons on nanostructured gold surfaces [76].

This terminology may cause confusion, as all plasmons are generated at the surface of metals. The term LP is simply used when surface plasmons are trapped within confined metal nanostructures like voids or spheres and the latter term SP refers to the generation of freely propagating electromagnetic surface waves along a continuous metal surface [77]. Resulting electromagnetic fields can be calculated by solving the Maxwell equations with corresponding boundary conditions. In this work, we investigate optical behavior in hybrid systems by making use of LPs, which enable a wide range of practical applications including light guiding and manipulation at the nanoscale, biosensing at the single molecule level, enhanced optical transmission and high resolution optical imaging like surface-enhanced Raman spectroscopy, and fluorescence emission enhancement.

4.1 Optical Properties of Metals

One of the first scientific reports of surface plasmons dates back to the beginning of the 20th century. In 1904, Maxwell Garnett observed bright colors in stained glasses (metal stained) and described their optical behavior in terms of the newly developed Drude model for metals and the electromagnetic properties of small spherical metal particles as derived by Lord Rayleigh [78]. In the upcoming years in 1908, Mie makes a great contribution to this field by developing his widely used theory of light scattering by spherical particles, which elucidates the scattering and absorption characteristics of spherical particles at various sizes [79]. In 1956, David Pines conducts theoretical calculations to explain the energy losses of fast electrons passing through metals and ascribes the electron energy reduction to collective oscillations of free electrons in the metal [79]. At this time, these oscillations are named as ‘plasmons’. Later studies revealed that the

plasmon modes generated by metal particles reside at the surface of metals. One year later, the coupled oscillations of bound electrons inside the metal and light were termed as ‘polaritons’ [78]. Although up to this point surface plasmons have been extensively studied and understood, the relation to its optical properties have not been understood till 1970. As more and more developments contributed in the following years to this field, there has been a gradual transition from the fundamental studies to more application driven research. One of the major contributions made in this field was accomplished by Fleischmann and coworkers, who observed strong Raman signals from pyridine molecules in close vicinity to rough Ag surfaces [79]. The Raman scattering signal was enhanced by the nearby electromagnetic field at the silver surface due to the surface plasmons. This discovery further opened up horizons in the currently well-established field of surface enhanced Raman scattering (SERS) [80].

As a first approximation, a metal can be viewed as an isotropic medium with a dielectric constant denoted by ϵ , a permeability μ and a conductivity σ . Using these parameters the Maxwell equations take the following form,

$$\nabla \cdot \mathbf{H} = 0 \quad (4.1)$$

$$\nabla \cdot \mathbf{E} = \frac{\rho}{\epsilon} \quad (4.2)$$

$$\nabla \times \mathbf{E} + \mu \frac{\partial \mathbf{H}}{\partial t} = 0 \quad (4.3)$$

$$\nabla \times \mathbf{H} - \epsilon \frac{\partial \mathbf{E}}{\partial t} = \sigma \mathbf{E} \quad (4.4)$$

which can be further transformed to give useful information about the optical properties of the metal particles. Using (4.3) and (4.4) and taking the divergence of (4.4), one obtains,

$$\rho = \rho_0 e^{-t/\tau} \quad (4.5)$$

where $\tau = \varepsilon/\sigma$. Since the conductivity of gold is very large, the relaxation time τ becomes a relatively small value, which is around 10^{-12} s [81]. Within an approximate approach it is realistic to take therefore ρ to be zero. After rearranging expressions (4.3) and (4.4) and by considering the planewave solution to Maxwell's equations, one gets,

$$E = E_0 \exp(i\hat{k} \cdot x - i\omega t) \quad (4.6)$$

for which then the wave equation for the metal can be written as

$$\nabla^2 E + k^2 E = 0 \quad (4.7)$$

where $k^2 = \omega^2 \mu(\varepsilon + \frac{i\sigma}{\omega})$. Now, the refractive index can be defined by the following complex expression;

$$\hat{n} = n + i\kappa = \sqrt{\varepsilon\mu} \quad (4.8)$$

where κ is the extinction coefficient. The following expressions relate the dielectric constant and the refractive index to each other:

$$n = \sqrt{\frac{\sqrt{\varepsilon_1^2 + \varepsilon_2^2} + \varepsilon_1}{2}} \quad \text{and} \quad \kappa = \sqrt{\frac{\sqrt{\varepsilon_1^2 + \varepsilon_2^2} - \varepsilon_1}{2}} \quad (4.9)$$

for complex $\hat{\varepsilon} = \varepsilon_1 + i\varepsilon_2$. From here the planewave equation can be re-written as

$$E = E_0 \exp\left(-\frac{2\pi\kappa x}{\lambda}\right) \exp\left[i\left(\frac{2\pi n x}{\lambda} - i\omega t\right)\right] \quad (4.10)$$

The first exponential in (4.10), which is real, stands for the absorption of the light, while the second part, which is complex, represents the oscillatory part of the wave. At this point, one should define the penetration depth of a material,

which is the depth light can travel inside a material where the electric field strength reduces to 1/e of its initial value. For visible frequencies, this value is found to be approximately 40 nm for gold. The expression for the penetration depth is given as

$$\delta(\lambda) = \lambda / (2\pi\kappa(\lambda)) \quad (4.11)$$

Up to now, the parameters defining a material were considered to be constants; however, in reality they are not. The properties are highly dependent on the wavelength and thus have to be considered while performing optical calculations. The dielectric constant is a measure of how electrons in a medium respond to an optical field. These electrons can be either free or bound electrons as it is the case for a metal or a dielectric material, respectively. The oscillatory behavior of the applied optical field can be described in terms of simple harmonic motion, as it done via the Lorentz and Drude models for dielectric materials and metals, respectively [79].

$$m\ddot{x} + b\dot{x} + Kx = eE \quad (4.12)$$

where m and e are the electron mass and charge, b is the damping coefficient standing for the energy loss due to scattering events, K is the spring constant and E is the electric field. For a metal, the conduction band is partially filled with free electrons, which allows for interband transitions at low energies so that it is possible to assume the spring constant to be 0. Laborious calculations using expression (4.12), lead to the desired expressions for the real and complex parts of the dielectric constant, which are given as follows

$$\varepsilon_1 = 1 - \frac{\omega_p^2}{\omega^2 + \gamma^2} \quad \text{and} \quad \varepsilon_2 = \frac{\omega_p^2 \gamma}{\omega(\omega^2 + \gamma^2)} \quad (4.13)$$

where ω_p is defined as the plasma frequency given by $\omega_p = ne^2/m\varepsilon_0$, and $\gamma = b/m$. The plasma frequency is defined as the frequency at which the dielectric constant components are zero so that there are no TEM modes in the

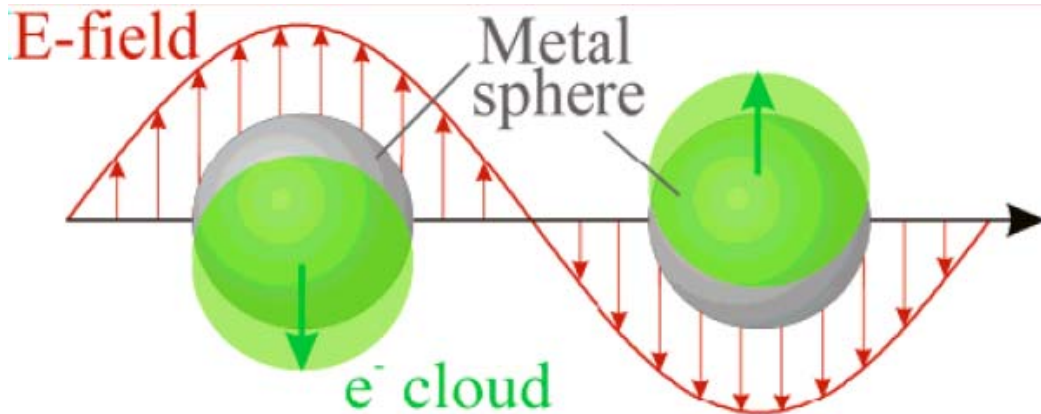


Figure 4.1.1. Schematic representation of electric field which is created by an incident wave and corresponding shift of electron cloud resulting in a plasmon resonance of the particle [82].

material and the wave is purely longitudinal, which corresponds to collective oscillations of the electrons in the direction of wave propagation. When a metal is radiated with light, the free electrons inside the metal will start to oscillate at the resonance frequency and generate a charge distribution within the metal, which will in turn form an electric field to reverse this effect and restore the initial neutral charge distribution. Fig. 4.1.1 depicts the polarization on the particle (with a sinusoidally varying electric field) and a restoring force generated due to the Coulomb attraction force between the fixed positively charged lattice and the conduction electrons [82]. The generated strong electric field inside the metal is an exponential function, which therefore readily decays to zero values at short distances. This effect is well observed for very small particles up to the penetration depth. When larger particle sizes are used, the metal behaves as a perfect reflector or even at lower frequencies, when the skin depth is reduced reflection becomes a dominant phenomenon. Although the Drude model is very effective in approximating optical properties of metals, it is not sufficient for metals like gold and silver due to complex interband transitions. Therefore, a model which uses both the Lorentz and the Drude models is necessary.

The surface plasmon resonance frequency of a metal nanoparticle is a property that strongly depends on the material of which it is composed. Various studies have shown that Al, Pb and Hg have SPR frequencies corresponding to the UV region, while Ag and Au NPs exhibit resonance frequencies towards the visible region. For this reason the latter two metals are very commonly used in applications including emission enhancement via plasmon-exciton interactions. Recent studies however have revealed that also Al NPs are very good candidates for the radiative power enhancement of intrinsic emission from bio-emitters like various peptides which are very commonly found in organisms [83]. The classical surface plasmon resonance is given in equation (4.14)

$$\omega = \left(\frac{e^2}{\epsilon_0 m_e 4\pi r_s^3} \right)^{1/2} \quad (4.14)$$

where ϵ_0 is the vacuum permittivity, m_e is the effective mass, and r_s is the radius of the sphere [84]. As can be seen from the equation, nanoparticle size is inversely proportional to the resonance frequency.

Finite difference time domain (FDTD) calculations made by using the commercially available simulation program (Lumerical Solutions Inc., Vancouver, Canada) reveal the effect of incident radiation on the near-field enhancement around the metal nanoparticle. The electric field intensity is maximized on the metal surface at the direction of polarization of the incident radiation and decays at very small distances as depicted in Fig. 4.1.2.

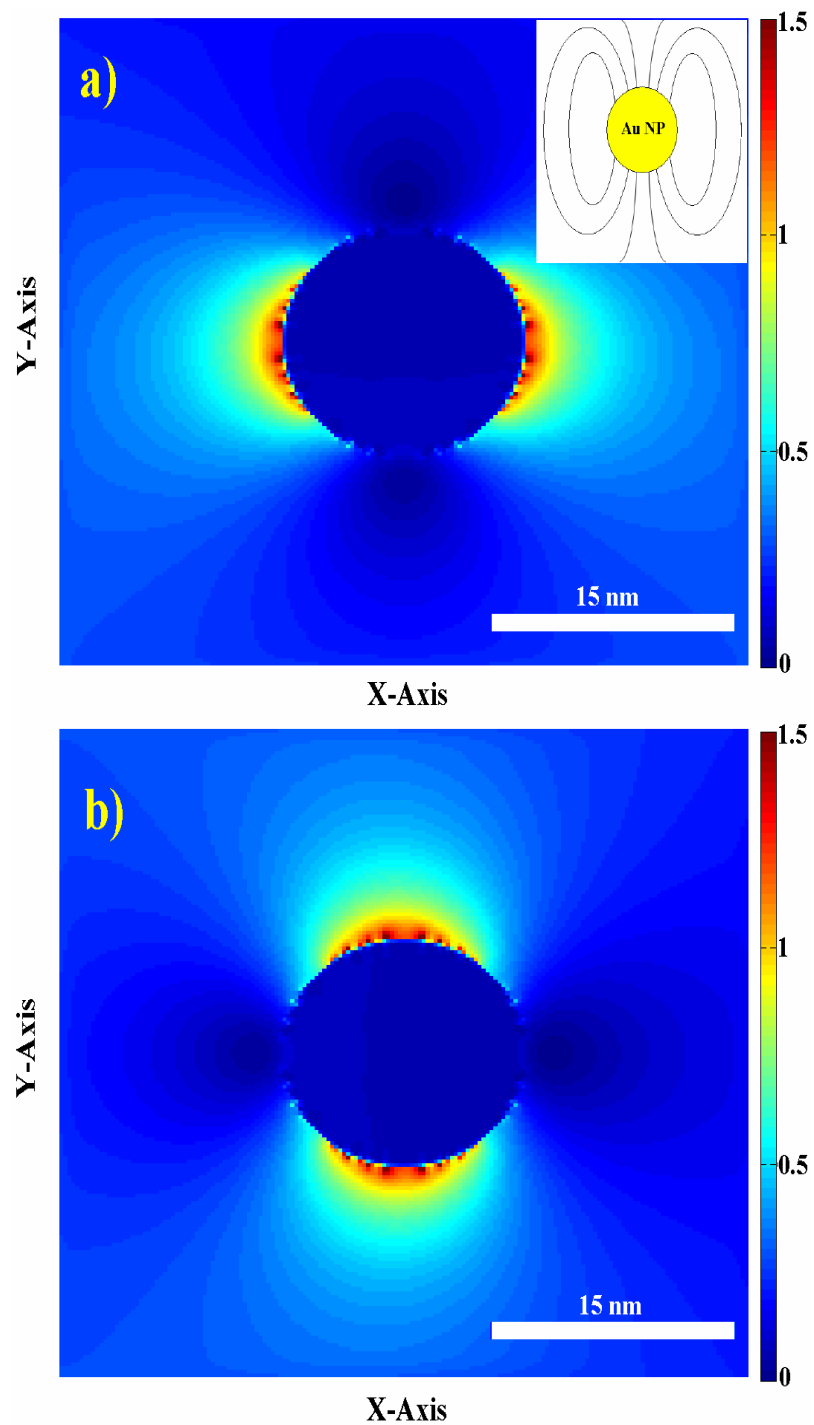


Figure 4.1.2. Electric field distribution of 15 nm Au metal nanoparticles at an incident plane wave radiating at 520 nm, which (a) propagates along the x-axis and is polarized along the y-axis, and (b) propagates along the y-axis and is polarized along the x-axis .

4.1.1 Mie Scattering

In 1908, Mie solved the Maxwell equations for electromagnetic radiation interacting with small metal spheres to explain the red color of colloidal gold nanoparticles [84]. The solutions of these calculations lead to a series of multipole oscillation cross-section of the metal nanospheres where $\sigma_{ext} = \sigma_{abs} + \sigma_{sca}$. The plasmon resonance depends highly on the size of the particle. In larger particles the higher-order modes become more significant because the light is no longer capable of polarizing the metal spheres in a homogenous manner. The peak of these higher-order modes appear at longer wavelengths, thus the experimentally observed red-shift in the plasmon band as nanoparticle sizes increase. Together with the red-shifting plasmon band, an increase in the bandwidth of the resonance band is observed. Size dependency in smaller nanoparticles, in which only dipole terms dominate, is more complicated. This assumption is made for particles satisfying the condition $2r \ll \lambda$, where only dipole terms contribute to the extinction cross-section. Using the dipole approximation, the Mie theory can be written in a simple form as

$$\sigma_{ext}(\omega) = \frac{9\omega\epsilon_m^{3/2}V\epsilon_2(\omega)}{c\{[\epsilon_1(\omega) + 2\epsilon_m]^2 + \epsilon_2(\omega)^2\}} \quad (4.15)$$

where V gives the particle volume, ω is the angular frequency of incident light, c is the speed of the light, ϵ_m and $\epsilon(\omega) = \epsilon_1(\omega) + i\epsilon_2(\omega)$ are the bulk dielectric constants of the surrounding material and the particle, respectively [85]. The resonance condition is realized when $2\epsilon_m(\omega) = -\epsilon_1(\omega)$, which is commonly known as the Fröhlich condition. Because the Mie theory assumes that the electronic structure and the dielectric constant of the nanoparticles and that of the metals are the same, which is no longer valid for very small particle sizes, in the results obtained from Mie calculations there appears no size dependency although the size dependency is observed experimentally. Therefore, the Mie theory needs

some modification, in which electron-surface scattering effects have to be taken into account for very small particles. The mean free path of electrons found for gold are around 70 nm, which means that if a particle has a diameter that is less than the mean free path of electrons, the electrons will scatter at the surface in an elastic but totally random way, which causes loss of the coherence of overall plasmon oscillation [86]. This effect is experimentally observed by a widening in the plasmon resonance bandwidth when particle sizes get smaller.

4.1.2 Size, Shape, Composition and Environment Dependency of Surface Plasmons

The surface plasmon resonance frequency is an optical property of metals that is highly sensitive to changes in size, shape, composition, and environmental factors [87,88]. Because of the importance of size in these materials there exist certain lower and upper boundaries for the observation of surface plasmons. This range can be stated as approximately 5 to 100 nm. The observed plasmon resonance peak for gold nanoparticles ranging from 5 to 50 nm spans a range of 500-600 nm, while this span is 380-430 nm for silver nanoparticles [89,90]. As explained above in the previous section, as the particle size increases the plasmon resonance peak shifts towards the red. As one of the key factors that affect the quality, i.e., the bandwidth of the plasmon resonance peak, is the monodispersity and the uniform shape of the colloidal nanoparticle dispersions. Highly monodisperse Ag dispersions are not easily obtainable using the current synthesis methods, therefore using gold as the plasmon generating material is preferred.

Furthermore, studies reveal that SPR bands are strongly shape dependent as has been shown by Schultz and coworkers as is depicted in Fig. 4.1.3 [91]. There are

several reports in the literature demonstrating the effect of different shapes including conventional spherical shapes, cubical, triangular and cylindrical ones,

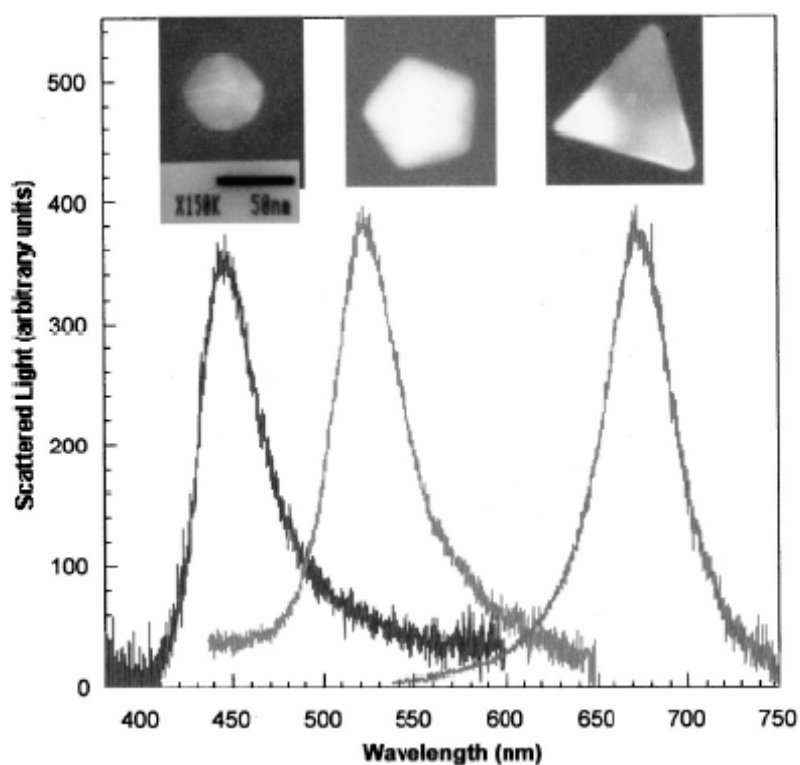


Figure 4.1.3. Scattered light intensities for silver nanoparticles with their corresponding high-resolution TEM images. Particles having spherical shape peak at the blue region, pentagon-shaped particles appear green, and triangular-shaped particles appear red [91].

which can also be named as nanorods. In one of these reports it has been shown that the plasmon resonance wavelength of a spherical Ag NP shifts from 400 to 670 nm by changing its shape to trigonal prism [91]. This change is attributed to the modified boundary conditions of the system corresponding to perturbed collective oscillations of conduction electrons and electromagnetic waves. The attractiveness of using small metal nanoparticles at different shapes lies also in their ability to modify the emitted light polarization kinetics as has been demonstrated in several studies. There are two types of surface plasmons formed

corresponding to the transverse and the longitudinal components of the resonance.

There exist also numerous reports of composite alloy structures of metal nanoparticles [92,93]. This strategy is exploited for the effective tuning of the observed plasmon resonance peak upon variation of the relative metal content. Another method that is used to alter SPR band is the change of the surrounding medium. Change of the solvent or spacer materials means a change in the refractive index of the surrounding medium, which accordingly modifies the observed SPR band. The formation of a silica dielectric spacer in form of metal core/silica shell nanostructures is a well established strategy to both modify the resonance peak but more importantly to reduce aggregation effects and prevent fluorescence quenching right at the fluorophore-metal interface. The presence of the silica shell surrounding the metal core nanoparticles induces again a red-shift in the plasmon resonance wavelength, which arises from a change in the refractive index of the outside medium. Also the silica shell thickness highly contributes to the shifts in the SPR band as will be shown in the next chapters. For our FDTD simulations, the refractive index of the surrounding medium is taken to be invariant to frequency is varied to 1.45, 1.33 and 1.00 depending on the medium which is silica, water or air.

4.1.4 Methods for Metal Nanoparticle Formation

Till date there have been developed many techniques to fabricate and synthesize metal nanostructures for utilization of plasmonic properties. Among these methods can be listed colloidal nanoparticle synthesis, electron-beam lithography, formation of metal islands using thermal evaporation, nano-skiving, focused ion-beam milling, photolithography, etc. Although electron-beam lithography and focused ion-beam patterning can produce highly precise

features, this technique suffers from being too expensive and time consuming compared to the listed other methods. In this work, we focus only on the formation of plasmonic nanostructures by the colloidal wet-chemistry in which the metal precursor is chemically reduced by sodium citrate to give the desired highly monodisperse metal nanoparticles [94]. This method proves to be very cost-effective as well as being a very simple process. The metal salt that is reduced for the Au NP synthesis is HAuCl_4 while citrate ions serve as the reducing agent as well as being the major stabilizing molecules, which surround the metal sphere and donate each of the nanoparticles a net negative charge. We had also previous attempts to utilize silver metal nanoparticles as the plasmon generating metal for which the metal salt we used was silver nitrate. Similar to the gold synthesis this synthesis requires the use of a reducing agent, which is sodium borohydride together with sodium citrate.

Chapter 5

Au-Silica Core/Shell Hybrid Nanoparticles Furnished with CdTe Nanocrystals for Enhanced Plasmon- Exciton Interactions

To date extensive research efforts have confirmed that optical properties of bulk semiconductors and metals are substantially modified when they are transformed into nano-dimensions [78]. For example, as described in Chapter 4, metal nanoparticles with dimensions smaller than hundred nanometers strongly oscillate at a specific resonance frequency to generate localized surface plasmons depending on their size [78]. This creates strongly localized electric fields in the close proximity of metal nanoparticles under external excitation. Similarly, because of the size effect, semiconductor quantum dot nanocrystals (NCs), with dimensions less than 10 nanometers, feature highly tunable absorption and emission characteristics. High levels of brightness and photostability, and broad excitation range with sharp emission spectra make these NCs ideal candidates as the building blocks for electronic and optoelectronic devices including light emitting diodes and solar cells, photodetectors, field-effect transistors and finally they can also be utilized as fluorescent labels in bioimaging [71,72,73,74,51,57].

Even though NCs are highly amenable for such a wide range of aforementioned applications, there are still some performance related issues yet to be overcome. One of such main challenges is to increase the fluorescence quantum efficiency of NCs and the other is to make them non-blinking. Plasmon coupling of NCs offers possible means to address these and similar problems. Recently, combining these two sets of nanomaterials has received increasing attention for their possible end uses of light harvesting and light generation in optoelectronics and highly promising sensing and imaging applications in biophotonics.

5.1 State-of-the-Art

A recent study conducted by Lakowicz and coworkers shows metal-enhanced intrinsic fluorescence of proteins on silver nano-structure surfaces separated by the dielectric material poly(vinyl alcohol). The specific protein for which enhancement factors up to 8 folds are observed compared to only on quartz films is the tryptophan analogue N-acetyl-Ltryptophanamide (NATA) [83]. This development could help for future applications of label free detection of biomolecules via plasmonic enhancement of intrinsic fluorescence of biomolecules. To observe plasmonic effects at a single molecule level, Sandoghdar and coworkers published their work in 2006 in which a single gold nanoparticle has been used as an optical nanoantenna for enhancement of single-molecule fluorescence [95]. This work was performed using the scanning probe technology. The quenching effect when fluorophores are in the near field to metal nanoparticles is usually an unwanted result when fluorescence enhancement is aimed. Past investigations of this kind of systems in comparison with theoretical estimations have suffered from the deficiency of control over a large number of parameters that are effective on the emission properties of emitters. To solve this problem, this group has developed a setup in which plasmon-exciton interactions can be investigated on single molecules under in-situ position control.

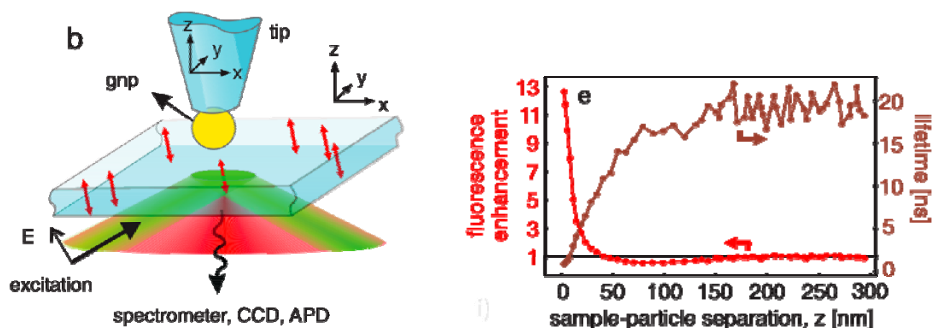


Figure 5.1.1 (left) Schematic representation of the experimental setup using a scanning probe method. (right) Fluorescence enhancement factor (red curve), lifetime (brown curve) of terrylene for varying sample-particle separations [95].

More recently, the number of publications describing plasmonic structures, in which there is a fixed dielectric spacer such as a silica shell, has increased. The growing interest in such plasmonic hybrid structures comes from the fact although there are straightforward methods of simply blending these nanomaterials and making thin films of their blends, or making bilayers of these nanocrystal and metal nanoparticle films on top of each other, such methods typically suffer from either limited control in spacing between metal nanoparticles and semiconductor nanocrystals precisely, or from total film thickness of bilayers that can be put together [96,97,98]. Because plasmons are generated right at the dielectric-metal interface, in order to achieve fluorescence enhancement instead of quenching there is a need for a dielectric spacing material, which is desirably optically transparent. In the literature there exist relatively new reports on the use of such nanostructures including the strong polarization dependence of plasmon-enhanced fluorescence of oxazine 725 embedded in the silica shell on single gold nanorods [99]. In this interesting study, the emission spectrum of the emitter is changed by the longitudinal plasmon resonance of the gold nanorods.

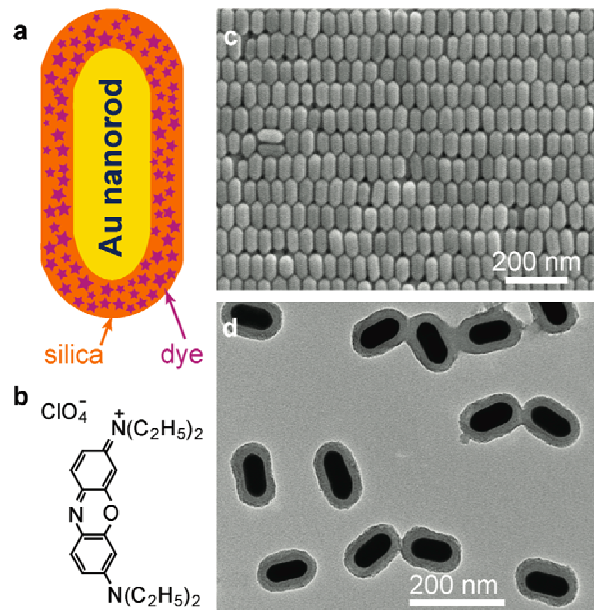


Figure 5.1.2. (a) Cartoon picture of the hybrid nanostructure composed of Au nanorods, silica shell and dye molecules, (b) Chemical structure of the dye oxazine 725, (c) SEM image of only Au nanorods, (d) TEM image of the core-shell nanostructures [99].

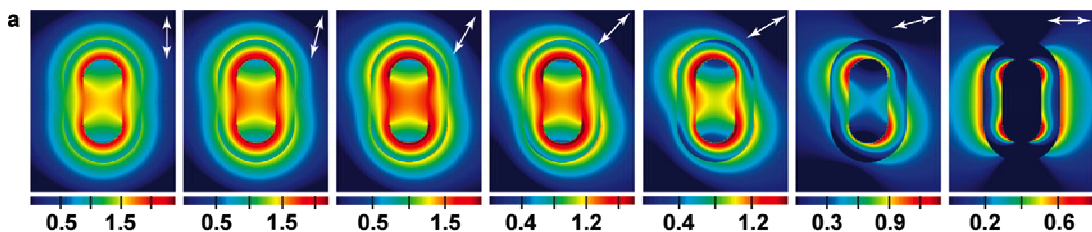


Figure 5.1.3. Electric field intensity maps obtained from FDTD simulations on a single Au nanorod core/silica shell structure, where the nanorod is aligned vertically. The excitation polarization of the incident light relative to the nanorod length axis is 0°, 15°, 30°, 45°, 60°, 75°, and 90°, respectively [99].

Another very recent study published in Nature is the demonstration of a spaser (surface plasmon amplification by stimulated emission of radiation)-based nanolaser using gold core dye impregnated silica shell spherical nanostructures of approximate size of 44 nm [100]. The motivation used in this study is that efficient use of nanoplasmonics is not fully realized because of lack of devices,

which can generate coherent plasmonic fields. The idea in this study is, as in analogy to a laser that generates stimulated emission of coherent photons, a spaser could generate stimulated emission of surface plasmons, which could further be used in plasmon-coupled FRET systems.

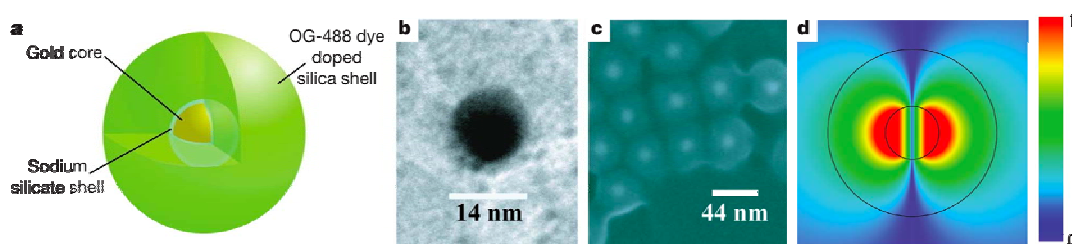


Figure 5.1.4. (a) Schematic of the hybrid nanostructure composed of Au core/dye-doped silica shell, (b) TEM image of Au core, (c) SEM image of gold/dye-doped silica core/shell nanoparticles, and (d) spaser mode with $\lambda = 525$ nm and $Q = 14.8$, where inner and outer circles are representative of the core and shell boundaries [100].

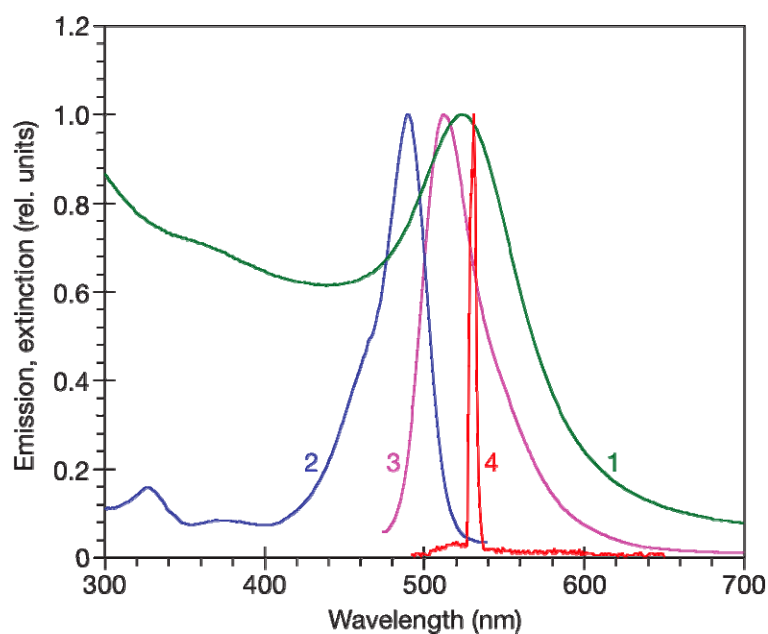


Figure 5.1.5. Normalized extinction (1), excitation (2), spontaneous emission (3) and stimulated emission (4) curves of Au/dye-doped silica nanoparticles [100].

In the literature, plasmonic coupling of nanocrystals using plasmonic metal nanoparticles have been previously demonstrated. One of the main methods used for such plasmonic coupling is the use of layer-by-layer coating of metal nanoparticles and nanocrystals. One main disadvantage of this method is that for this method in order to achieve maximum performance, one needs to optimize spacer thicknesses and accordingly coat monolayers of nanocrystal emitters in a layered manner. This can be somewhat laborious and time-consuming.

A recent work, which offers an alternative solution to this kind of plasmon-exciton interactions between gold NPs and NC emitters, is highly related to our work. In this study, the plasmon coupling of silica coated gold core shell nanoparticles decorated with CdSe NCs is studied [101]. In this report, only enhancement factors are given as a function of Au/SiO₂ nanoparticle concentration with respect to two different shell thicknesses at constant core diameter of 45 nm and for two different NC efficiencies. Higher enhancement factors which reach a maximum of 1.8 are observed for imperfect nanocrystals with a quantum efficiency of 5 %. All nanoparticle samples are prepared in THF.

5.2 Computational Analysis and Experimental Demonstration with Optical Characterization Results of our Hybrid CdTe Furnished Au-Silica Core/Shell Nanoparticles

In our work, we develop and demonstrate Au-silica core/shell nanoparticles that successfully assemble CdTe nanocrystals right on their silica shells for enhanced plasmon-exciton interactions, while avoiding the problems of lacking control in spacing and limited film thickness. Herein we present our synthesis and

characterization results of this new set of water-soluble CdTe NC decorated, Au-silica core/shell hybrid nanoparticles with silica shell thicknesses controlled and tuned by synthesis.

5.2.1 Synthesis, Characterization, and Simulation of Hybrid Nano-Assemblies

The following chemicals were of analytical grade and used without further purification: (3-aminopropyl)triethoxysilane (APS), tetraethylorthosilicate (TEOS), sodium silicate solution ($\text{Na}_2\text{O}(\text{SiO}_2)_{3-5}$, 27 wt % SiO_2), HAuCl_4 , trisodium citrate dihydrate, NH_4OH , ethanol, and the cation-exchange resin Dovex were purchased from Sigma-Aldrich. Milli-Q water and absolute ethanol was used in all syntheses.

Transmission electron microscopy (TEM) was carried out using Tecnai G2 F30 by FEI, and optical characterizations were carried out using Varian Eclipse for fluorescence measurements, Varian Cary 100 for absorption measurements and PicoQuant FluoTime 200, which is a polarizer integrated time-correlated single photon counting system for time-resolved photoluminescence measurements.

The simulations are performed by the use of a commercial software package (Lumerical Solutions Inc., Vancouver) on a high performance computer. This software solves the Maxwell's curl equations in time domain on discrete spatial grids. This is the state of the art method used in literature and is called the finite difference time domain (FDTD) method. We use Johnson and Christy data results for imitating the dielectric behavior of colloidal Au NPs and Palik for our silica shells. For the first set of simulations showing the absorbance calculation results for Au core and Au/Silica core-shell nanoparticles a propagating

planewave programmed to radiate between 300-800 nm is introduced into the simulation region to imitate the excitation source in the experiment. Au spheres are placed into a power transmission box with a refractive index of 1.33 (corresponding to the dispersion medium) to observe the plasmonic response of Au NPs. The plane-wave is oriented perpendicular to Au NPs surface with TE polarization. FDTD simulations replicate the plasmonic response of Au NP cores and also Au NP cores with varying silica shell thicknesses. In the second set of simulations normalized radiative and non-radiative decay rates of a dipole source (to imitate nanocrystals in our experiments) in close proximity are calculated using transmission and radiated power intensity values in the absence and the presence of plasmonic Au or Au-silica NPs. In the third set of simulations electric field intensity maps of a dipole source alone and in the presence of Au NP and Au NP with a 5 nm silica shell is simulated. Enhancement/quenching of electric field intensities are found by the ratio of the electric field intensity in the presence of plasmonic nanoparticles to the absence of plasmonic nanoparticles. At all sets the simulation region is divided into 0.5 nm mesh size with maximum mesh accuracy to minimize the staircase effect on the boundaries of metal spheres. The results of our numerical simulations are presented and discussed in the subsequent sections.

In our synthesis procedure, hybrid nanostructures of Au/SiO₂/CdTe-NCs are prepared using a synthetic pathway comprising multiple steps. First, synthesis of gold nanoparticles (5×10^{-4} M) is performed according to the standard sodium citrate reduction method, which yields a stable, deep-red gold nanoparticle dispersion with an average diameter of 15 nm. We prepare our gold colloids using the chemical reduction method [94]. For that, we use chloroauric acid HAuCl₄ and trisodium citrate Na₃C₆H₅O₇ as the starting materials. 0.08 g of chloroauric acid is dissolved in 200 mL of Milli-Q water corresponding to a molarity of 1 mM. Then, 0.26 g of sodium citrate is dissolved in 20 mL of Milli-Q water corresponding to a molarity of 44 mM in another beaker. Under continuous stirring, the first beaker is heated up until it starts boiling. The sodium

citrate solution in the second beaker is then added quickly into the first beaker. The mixture is boiled for 20-30 minutes to obtain a stable dispersion of dark-red colored gold nanoparticles. Finally, the mixture is cooled down to room temperature under continuous stirring; the resulting gold nanoparticle dispersion is shown in Figure 5.2.1.1.



Figure 5.2.1.1 A sample of dark red, colloiddally synthesized gold nanoparticles dispersed in aqueous medium.

The gold surface has very little electrostatic affinity for silica. Since gold does not form a passivation oxide layer in solution, no silica layer can directly be deposited on the particle surface. Apart from the inherent vitreophobicity of gold surfaces, also the organic ligands surrounding the gold particles for prevention from coagulation render the gold nanoparticles vitreophobic [94]. To circumvent this problem, one can use organic stabilizers with two functionalities at two ends, either thioalkanes or silane derivatives of thioalkanes. Due to the very strong

affinity of gold to amine and thiol groups, effective pre-coating of the silane coupling agents on Au NPs is achieved as a very thin layer.

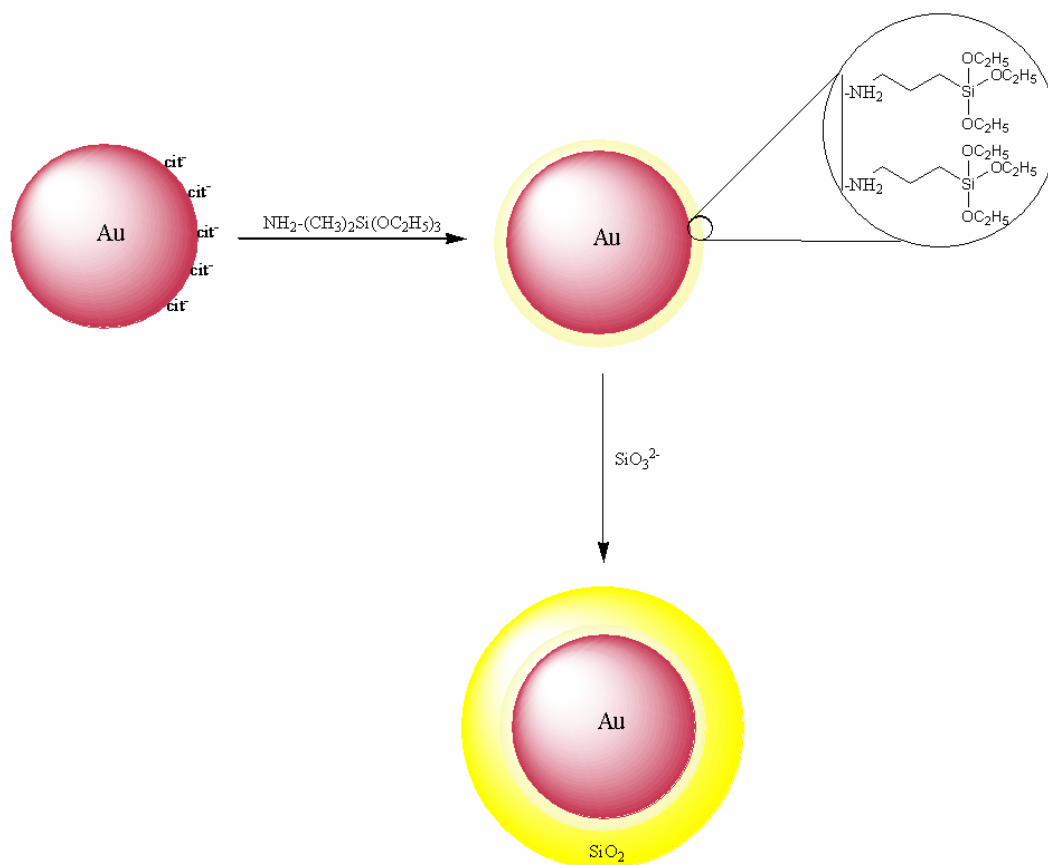


Figure 5.2.1.2 Principal procedure for the formation of gold-silica core/shell nanostructures. (a) Formation of monodisperse citrate capped gold nanoparticles, (b) surface modification by use of APS which forms as a monolayer, and (c) deposition of silica shell by polymerization of active silica on the pre-coated silanized gold surface.

Further steps involved surface activation of the citrate capped Au nanoparticles with (3-Aminopropyl) triethoxysilane (APS -a silane coupling agent) for 15 min to achieve complete complexation of amine groups with the gold surface. Next, to complete the silica-shell growth of the silane functionalized Au nanoparticles, a 100 mL gold sol is allowed to stand for 24 h under vigorous stirring after addition of a 5 mL solution of 0.54 wt % active silica, which is brought to the desired pH of 10-11 using Dowex. To facilitate further growth of a thicker silica shell on Au nanoparticles, the Au sol in varying water/ethanol concentrations is

mildly stirred for 12 h after addition of TES (tetraethyl orthosilicate) and ammonia [94].

In the next step, the silica coated gold nanoparticles are surface treated with APS to form hybrid Au-silica core/shell nanoparticles functionalized with $-NH_2$ groups. Finally, to the sonicated, surface-modified Au nanoparticle dispersion, a dilute solution of TGA capped CdTe NCs was rapidly added, which results in the aimed hybrid Au/SiO₂/CdTe-NC nano-assembly with the cartoon representation discussed in the next section.

5.2.2 Experimental Demonstration and Optical Characterization Results and Numerical Analysis

The absorption spectrum of our Au colloids is obtained with a peak maximum at 518 nm with a full width half maximum of around 80-90 nm as depicted in Fig. 5.2.2.1 The gold nanoparticle synthesis results in an average particle size of 15 nm with an expected size distribution of 10%. Our simulated absorption spectrum peaking at 520 nm, mimics the plasmon behavior of the colloiddally synthesized Au NPs and is in good spectral agreement with the experimental measurement.

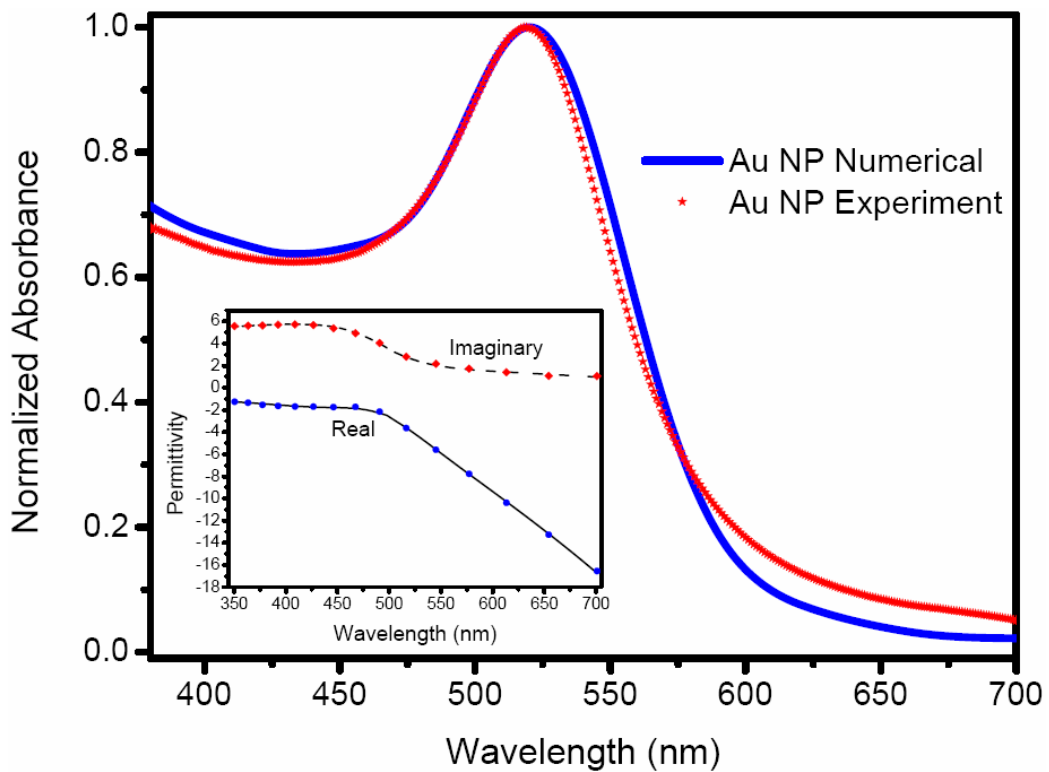
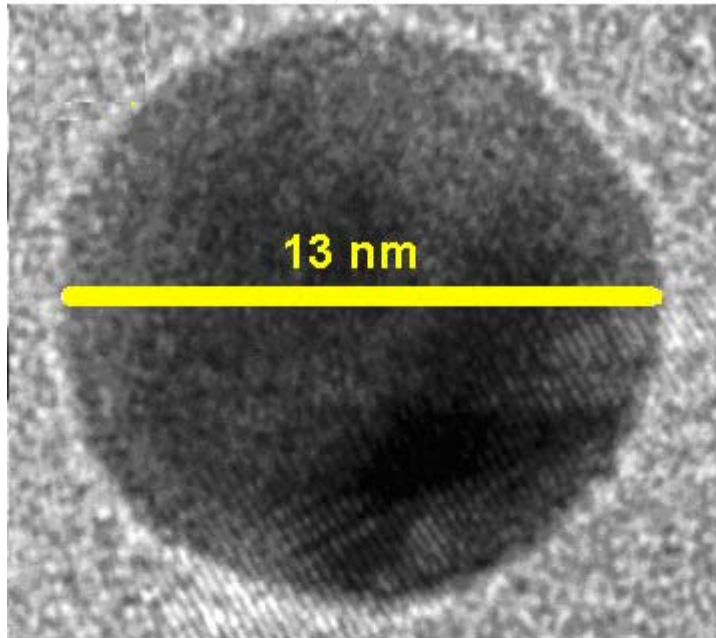


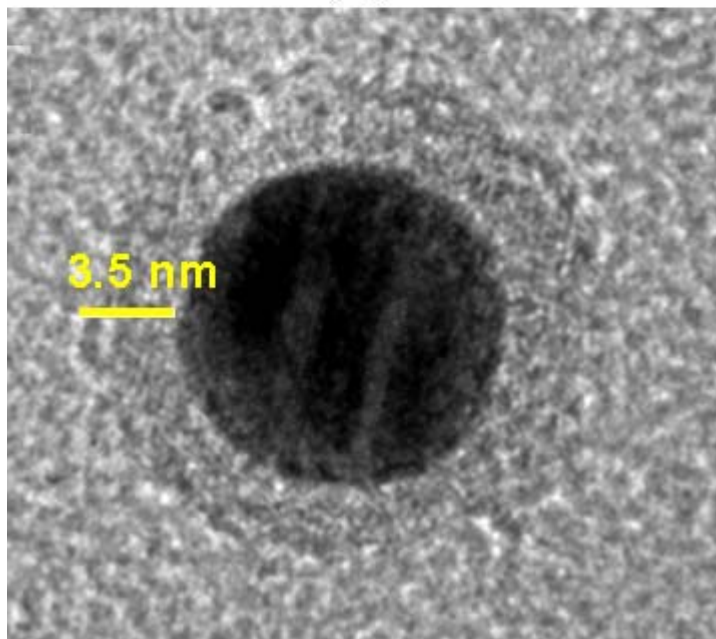
Figure 5.2.2.1 (Onset) Normalized numerical and experimental absorption spectra of 15 nm-colloidal Au NPs dispersed in water. (Inset) FDTD simulation and experimental data of real and imaginary parts of the permittivity constant of Au adopted from Johnson and Christy [102].

Extensive synthesis studies and TEM characterizations show that it is possible to control and tune the silica shell thickness around Au cores as can be seen in Fig. 5.2.2.2 (a)-(f).

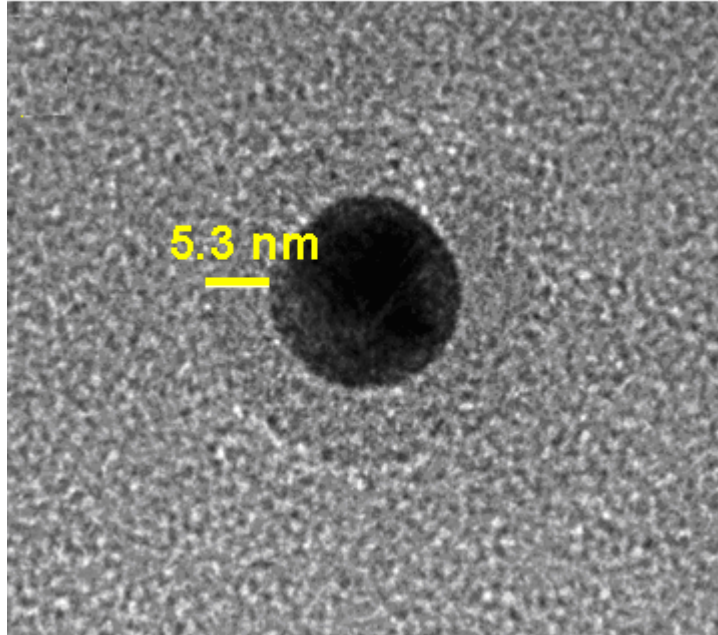
(a)



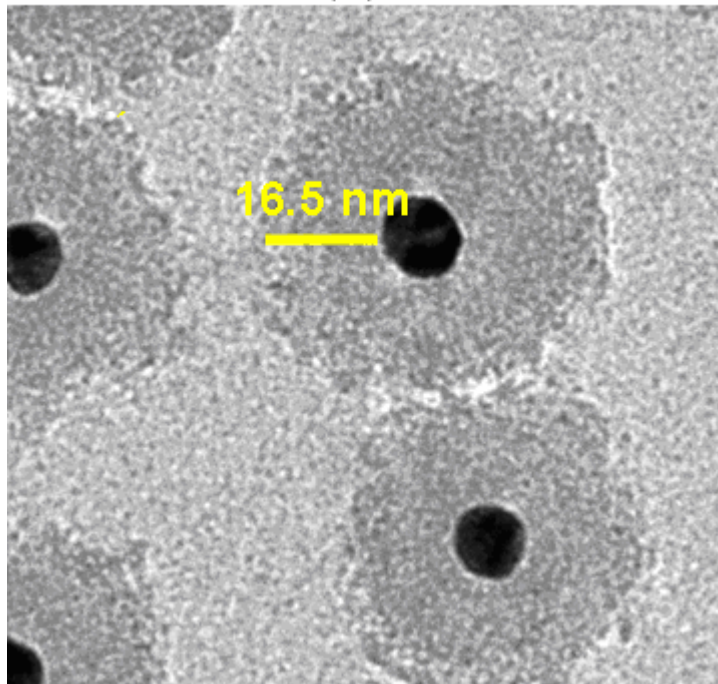
(b)



(c)



(d)



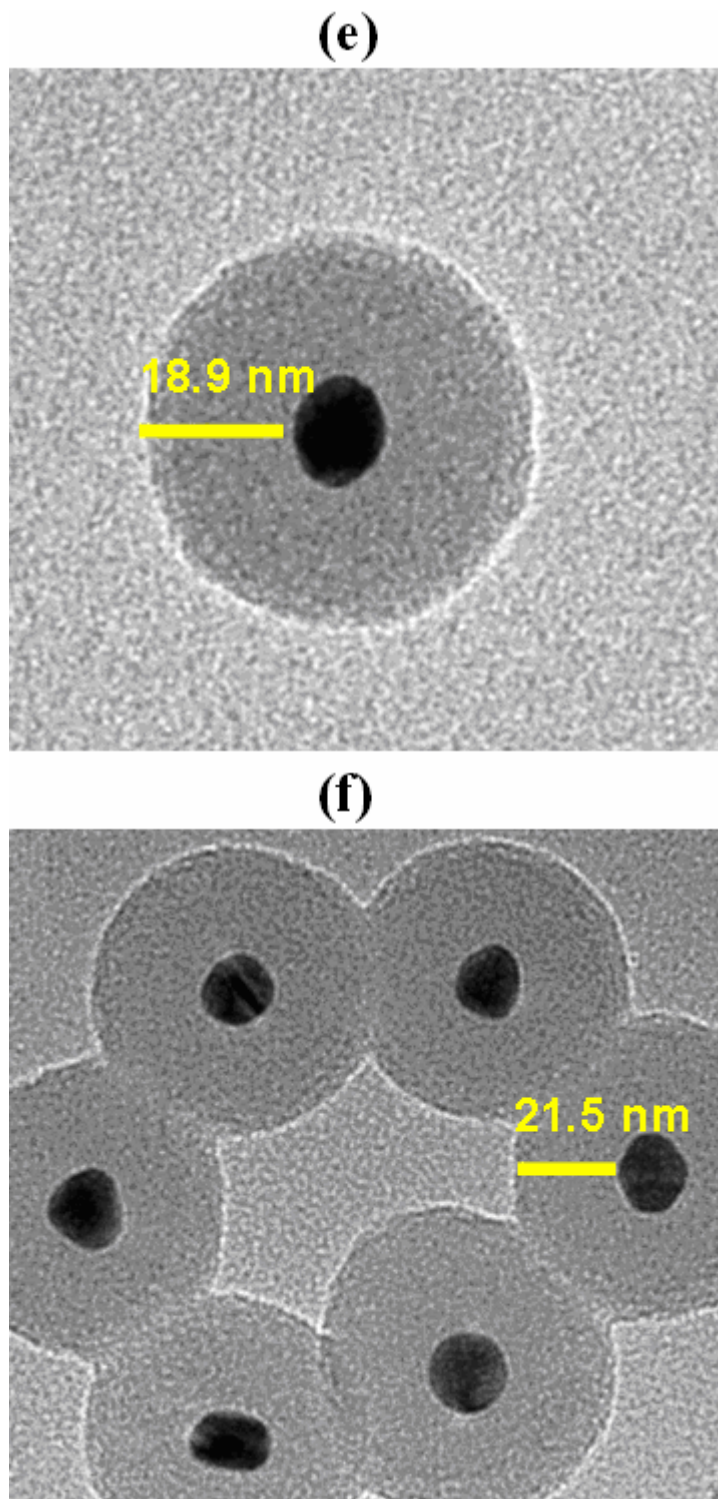


Figure 5.2.2.2 (a)-(f) Transmission electron micrographs of only Au NPs with average diameter being 15 nm, and Au core/silica shell nanoparticles with average shell thickness varying from 3, 6, 16, 19, 22 nm, respectively. The silica shell thicknesses are controlled and tuned by varying synthesis conditions.

Together with TEM imaging, in order to monitor optical behavior changing as a result of silica shell deposition as the shell thickness is varied, we additionally recorded their absorption spectra. Fig. 5.2.2.3 nicely depicts the red-shifting effect of increasing shell thickness, while the largest shift from 518 nm to 524 nm is observed for initial silanization of the gold surface with active silica to yield an average shell thickness of 3 nm.

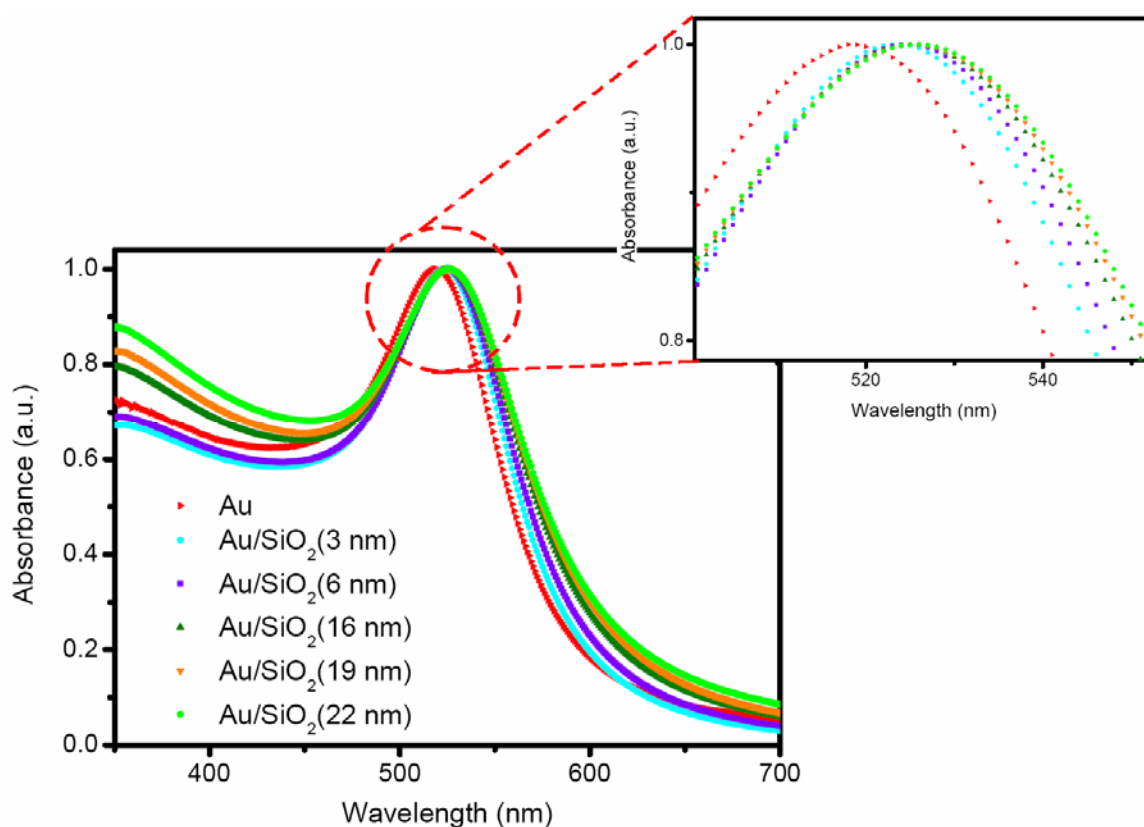


Figure 5.2.2.3. Absorbance spectra of samples given in Figures 5.1.2.2 a)-f) to monitor shifts in the surface plasmon resonance peaks because of increasing silica thickness. The SPR band for only Au NPs appears at 518 nm.

Decoration of CdTe NCs on Au-silica hybrid nanoparticles allows for the intimate integration of NCs with Au nanoparticles with a precisely controlled spacing shell. To maximize interactions between plasmonic nanostructures and fluorophores, there is a need for keeping the interparticle distance at an optimum separation. To achieve this goal, the hybrid nanoassembly shown below is a

perfect architecture with positively charged amine functional groups on silica rendering the silica surface electrostatically favorable for the negatively charged TGA capped CdTe NCs (Fig. 5.2.2.4).

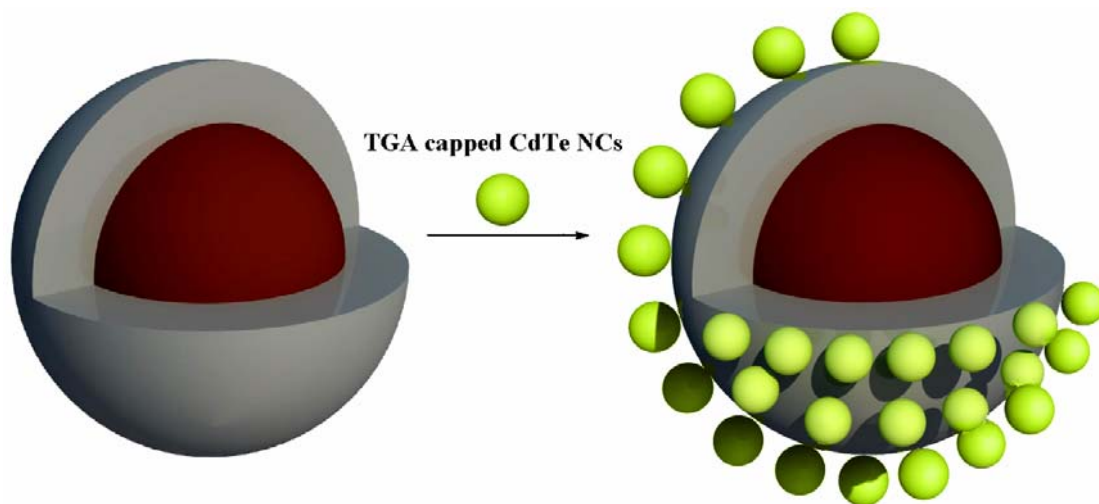


Figure 5.2.2.4 Flow diagram for the decoration of APS functionalized Au/SiO₂ core/shell nanoparticles with water-soluble CdTe NCs.

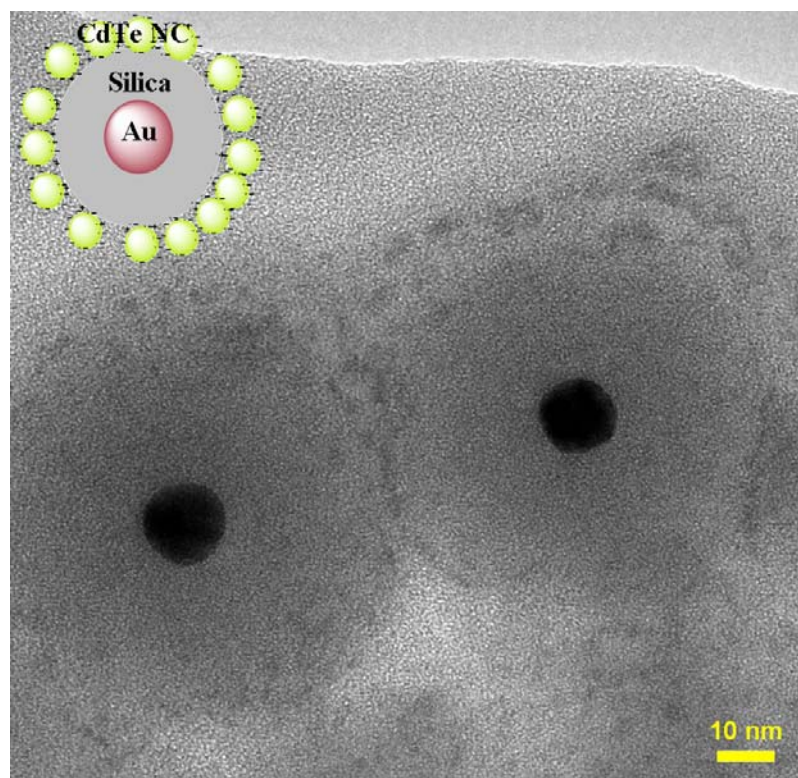


Figure 5.2.2.5. Transmission electron micrograph of hybrid Au/SiO₂/CdTe-NC nano-assembly (onset), schematic representation of this hybrid structure (inset).

To verify the binding of CdTe NCs to the positively charged silica surface, we performed TEM imaging. The micrograph depicted in Fig. 5.2.2.5 clearly illustrates the surface binding of NCs, which have an average size distribution of 4 nm.

The nanocrystal was intentionally chosen to obtain maximum spectral overlap between the NC absorption/emission and the Au NP absorption. Fig. 5.2.2.6 shows the absorbance spectrum of NC peaking at 520 nm.

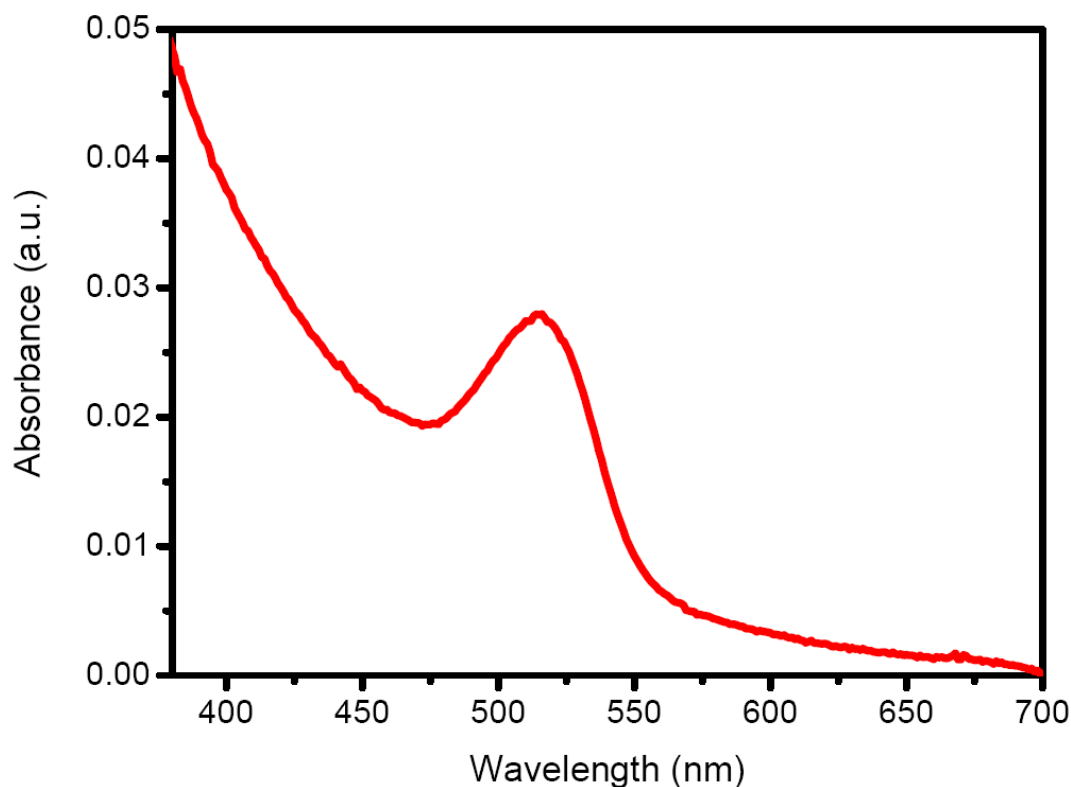


Figure 5.2.2.6. Absorbance spectrum of colloiddally synthesized CdTe NC in water.

In order to investigate the spectral match between the absorbance/emission of the NCs and the absorbance of Au NPs, we plotted their normalized intensities as a function of wavelength as is given in Fig. 5.2.2.7.

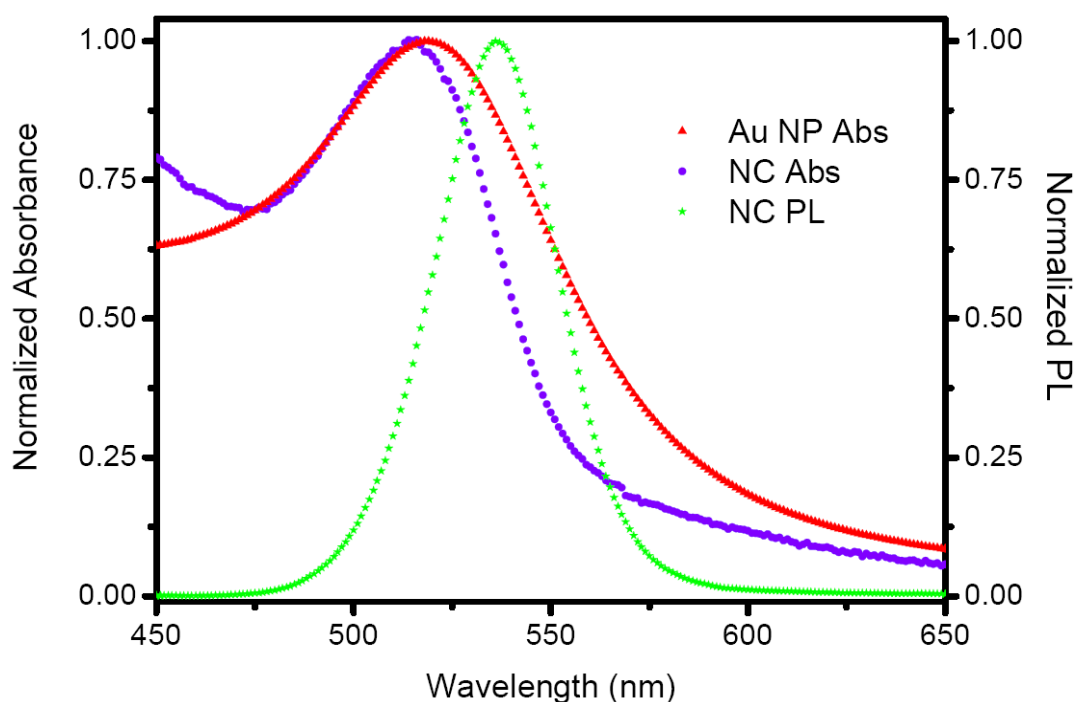


Figure 5.2.2.7. Spectral overlap between NCs and Au NPs for maximum plasmon-exciton coupling interactions. Absorbance and PL intensities are normalized.

To evaluate the metal effect on PL of CdTe NCs, we used a dilute solution of CdTe in water as a reference with an original fluorescence quantum efficiency of 20%, and a maximum emission wavelength at 538 nm. There are multiple interaction mechanisms between fluorophores and metal nanoparticles that can influence the PL intensity. One mechanism is due to the modification of the electric field near the metal surface, which changes both the field applied to the NCs and the field radiated by it. Experimentally, we observe that, in the presence of metal NPs separated by dielectric layer, the NC emission is significantly enhanced. But in the presence of metal NPs lacking a dielectric spacer, NC emission is quenched as is demonstrated in Fig. 5.2.2.8.

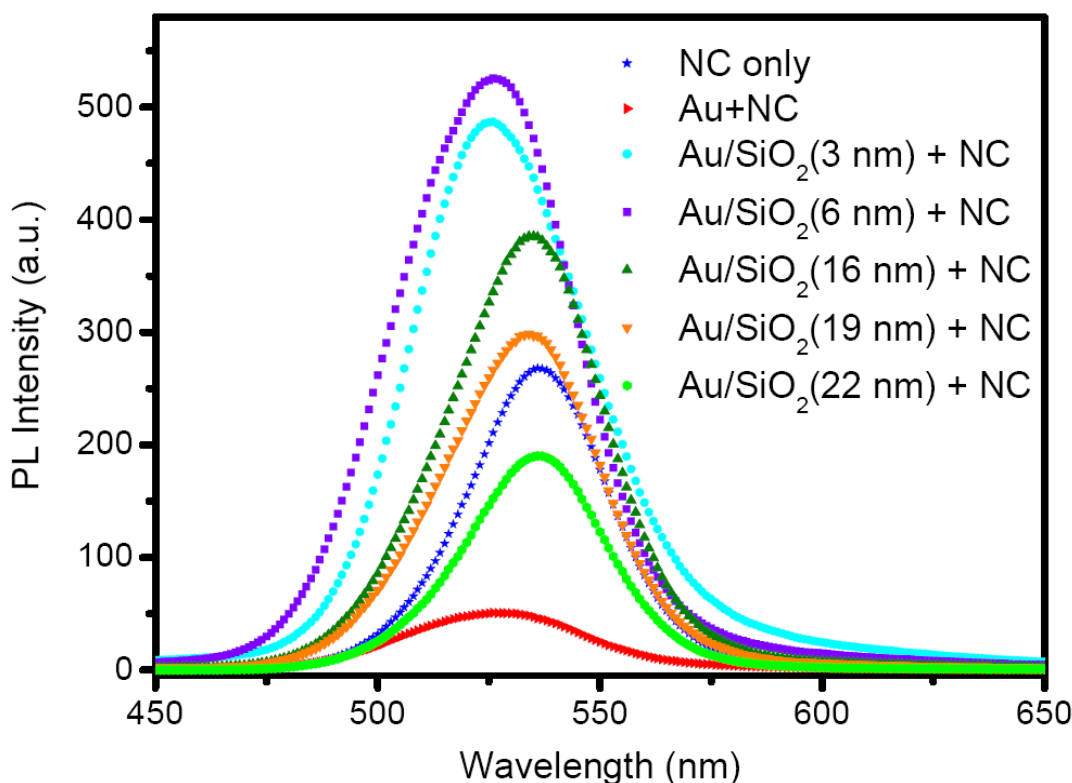


Figure 5.2.2.8. PL spectra of our CdTe NCs alone (blue curve), and those in the presence of Au NPs with and without a dielectric spacer made of a silica shell. The red curve indicates a 5.2-fold quenching due to the lack of a silica shell.

The PL spectra indicate a gradual shift of the peak position towards the plasmon resonance peak as plasmon-exciton interactions increase with decreasing shell thickness. Under strong plasmon-exciton interactions, enhanced emission takes place at the surface plasmon resonance wavelength, which therefore results in maximum peak wavelengths closer to the SPR band. We observed maximum emission for 6 nm thick silica shell with an enhancement factor of 1.97 compared to the NC only emission at 537 nm. A higher enhancement factor could be expected for the composite structures having thinner shells (3 nm). However, it is difficult to coat the core gold nanoparticles uniformly with such a thin layer of silica, which in turn resulted in a lower emission enhancement when than what would ideally be expected. The enhancement factor for a 3 nm shell thickness is approximately 1.81. But in the presence of gold NPs lacking a dielectric spacer,

the NC emission is quenched by a factor of 5.2, due to highly increased non-radiative mechanisms. Also, we observe that the effect of metal nanoparticles gradually decreases as the shell thickens, resulting in a NC emission that resembles almost the only NC emission both in terms of the photoluminescence

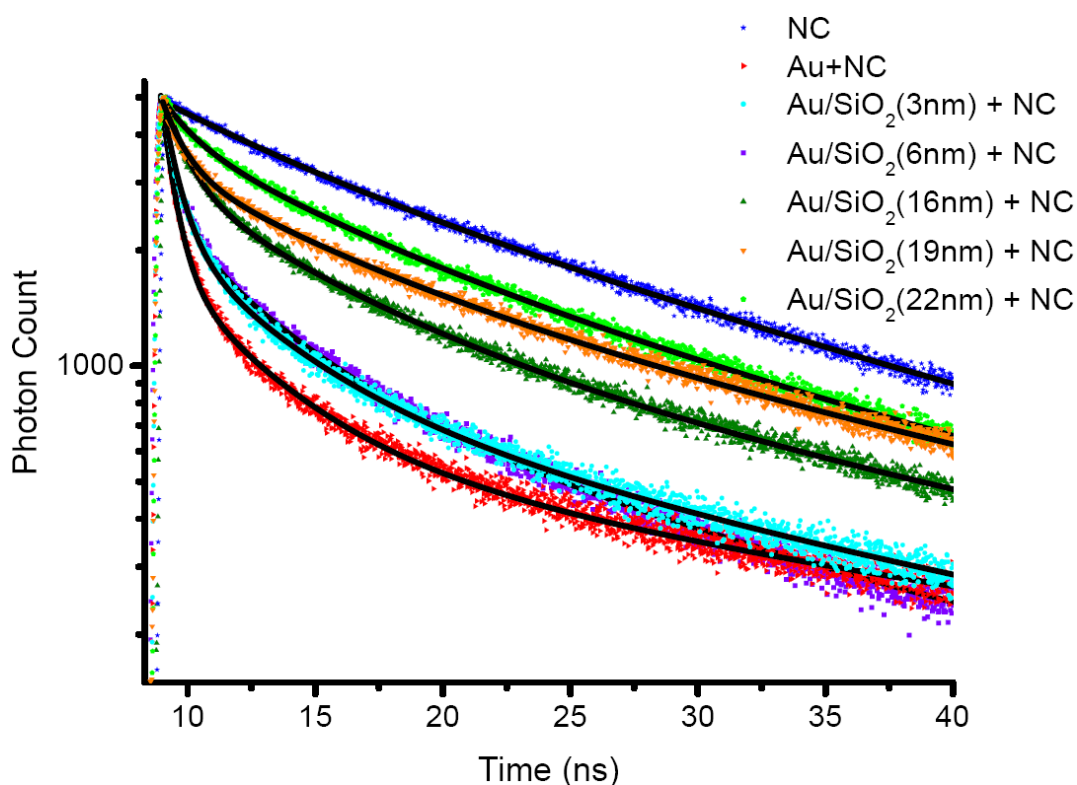


Figure 5.2.2.9. Time resolved PL decays of our CdTe NCs alone (blue curve) and those in the presence of Au NPs (red curve) and in the presence of Au NPs and a dielectric spacer shell. Corresponding fitted curves are indicated in black.

intensity as well as the PL peak wavelength. A lower PL intensity for the nanoparticle assembly with the highest average shell thickness of around 22 nm is probably observed due to competing effects resulting from high silica concentration or other competing effect which still have to be investigated.

We also comparatively investigate emission kinetics of these samples by taking time-resolved fluorescence decay curves, as depicted in Fig. 5.2.2.9. We observe a significant shortening in decay time of CdTe NCs for each hybrid assembly. The decay lifetimes of CdTe NCs are extracted using the multi-exponentially fitted decay curve through recording the time at which the maximum photon count falls to 1/e of its initial value. The recorded lifetimes and related quantities for the fitted curves are given in Table 5.2.2.1. For the most enhanced emission (3 nm and 6 nm spacing), the photon decay lifetime of CdTe NCs is modified from 15.4 ns to 1.9 ns and 2.1 ns, respectively in the presence of metal NPs and to 1.2 ns in the absence of a silica spacer between metal nanoparticle and NC.

Table 5.2.2.1. Comparison of the decay lifetimes and rates, calculated and experimental enhancement factors for the CdTe NCs with and without Au nanoparticles.

	CdTe NCs	CdTe NCs on Au NPs	CdTe NCs on Au/SiO ₂ (3 nm) NPs	CdTe NCs on Au/SiO ₂ (6 nm) NPs	CdTe NCs on Au/SiO ₂ (16 nm) NPs	CdTe NCs on Au/SiO ₂ (19 nm) NPs	CdTe NCs on Au/SiO ₂ (22 nm) NPs
Decay Lifetime (ns)	15.4	1.2	1.9	2.1	5.3	7.9	10.5
Decay Rate (ns⁻¹)	0.065	0.835	0.525	0.466	0.188	0.127	0.095
Calculated Enhancement Factor	-	-	4.50	4.44	3.62	2.95	2.27
Experimental Enhancement Factor	-	0.19	1.81	1.97	1.44	1.11	0.71

Photoluminescence and time-resolved fluorescence characteristics support each other. In both cases with metal NPs, decay rates comprising both radiative and non-radiative components. However, their modified emission spectra can be explained by increased non-radiative decay rate in the presence of metal NPs, which results in quenched fluorescence, and increased radiative decay rate in the

presence of metal NPs separated by dielectric silica shells, which results in enhanced fluorescence.

We account for the modified emission kinetics by investigating the CdTe NCs decay rates with and without Au nanoparticles. For NCs, the fluorescence quantum efficiency is expressed by the ratio of the radiative decay rate to the total physical decay rate including radiative and non-radiative decay components given in (5.1)

$$Q_0 = \frac{\Gamma}{\Gamma + k_{nr}} \quad (5.1)$$

where Γ is the radiative decay rate and k_{nr} is the non-radiative decay rate [20]. In the presence of Au nanoparticles with and without silica shells, radiative and non-radiative components are modified and the fluorescence quantum efficiency can be calculated using (5.2)

$$Q_m = \frac{\Gamma + \Gamma_m}{\Gamma + \Gamma_m + k'_{nr}} \quad (5.2)$$

where Γ is the radiative decay rate, Γ_m is the radiative decay rate in the presence of Au NPs, and k'_{nr} is the modified non-radiative decay rate in the presence of Au nanoparticles [20]. The comparison of all calculation results for varying hybrid nanostructures is depicted in Table 5.2.2.1.

Numerical modeling indicates that such a hybrid nano-assembly allows for plasmon-exciton interaction. We investigated the dependence of normalized decay rates of dipole emitters in close proximity to gold nanoparticles with respect to their interparticle separation. Our FDTD model is in strong agreement with the theoretically calculated values. Also, the orientation dependence of the

dipole has an effect on the decay rate, but still the effect is nearly similar in both polarizations. There is a strong interaction for small separations less than 10 nm, which exponentially decreases as the separation increases. Since the main contribution to the total decay rate comes from the non-radiative processes (e.g. phonon generation), there is not much discrepancy between the parallel and perpendicular orientations of the dipole radiator.

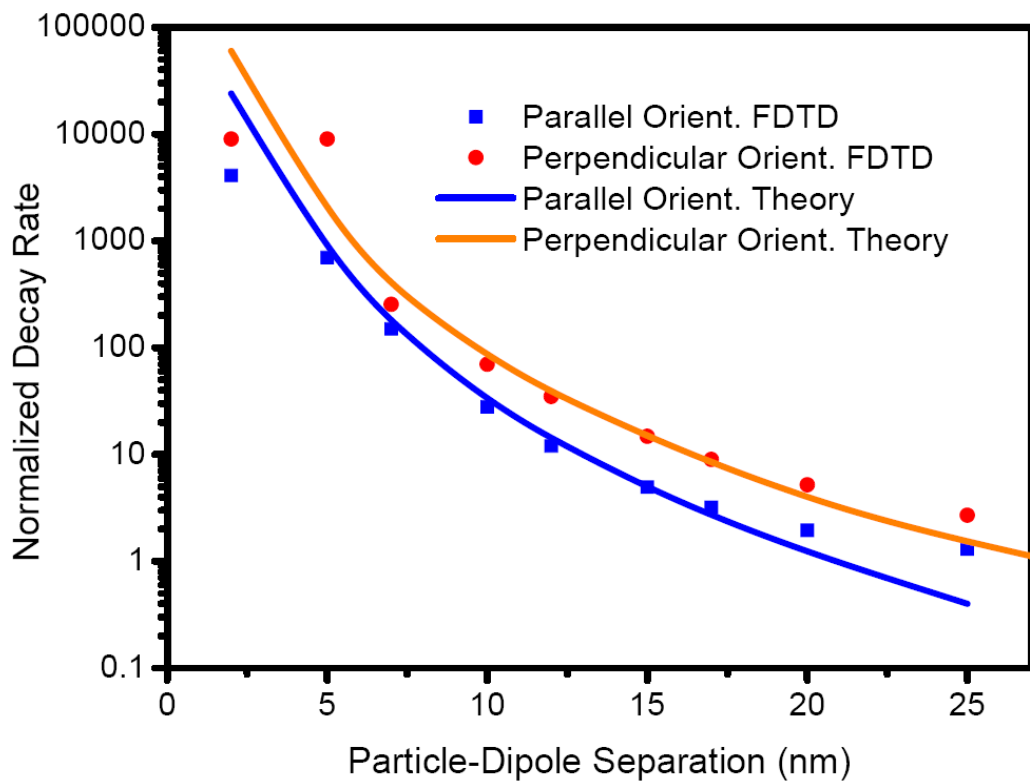


Figure 5.2.2.10. Calculations of normalized decay rates using computational FDTD method, and analytical method [103] in different orientations of dipole polarization to investigate the effect of particle-dipole separation.

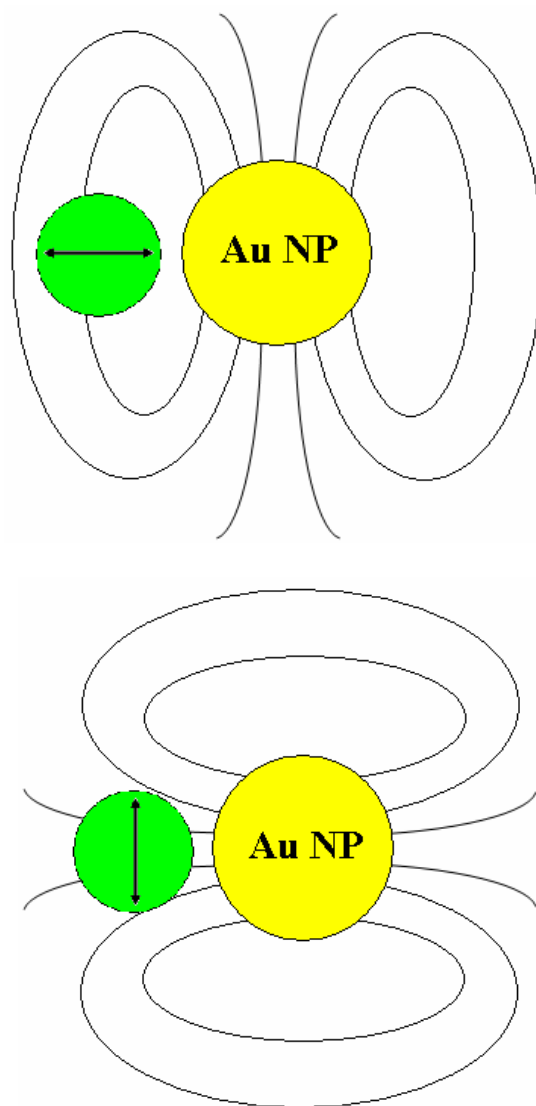


Figure 5.2.2.11. (Top) Perpendicular and (bottom) parallel polarization orientations of the dipole emitter with respect to the Au surface.

The dependence on polarization direction however strongly influences the radiative mechanisms as can be seen from the enhancement factors recorded for varying interparticle distances as illustrated in Fig. 5.2.2.12. We obtain maximum enhancement at distances 2 nm and 5 nm at perpendicular orientation, while these factors diminish to almost unity as the direction of the dipole radiator is changed to parallel orientation. Although the highly increasing trend towards smaller separations leads to a higher enhancement factor at 2 nm, the simulated factor is

only slightly higher than the value evaluated for 5 nm, which probably results from the strong non-radiative processes in such close proximities. These results

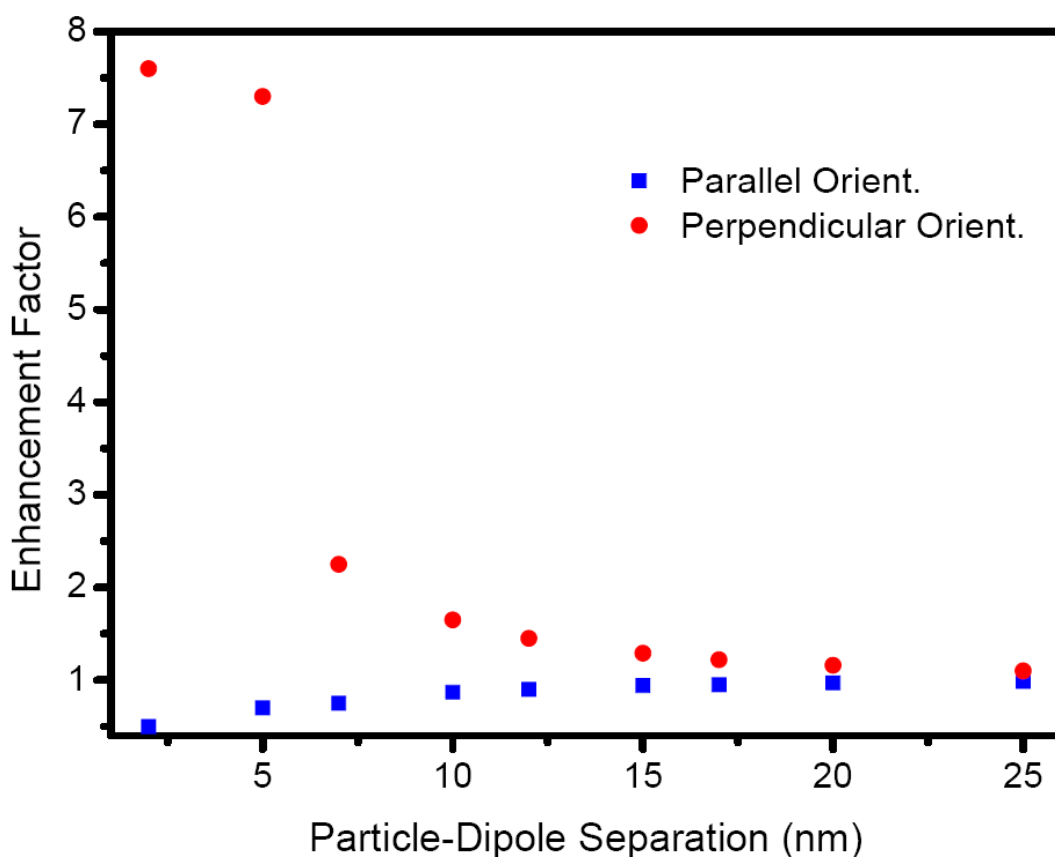


Figure 5.2.2.12. Simulation results of enhancement factors in relation to varying particle-dipole separations by using a silica shell for parallel orientation (square) and perpendicular orientation (disc).

are in good agreement with the experimentally observed enhancement factors given in Table 5.2.2.1 although they are about 4 times smaller than the simulated factors. This can be explained by the non-ideal conditions in the experimental setup such as the use of an incoherent and unpolarized light source giving an orientation averaged emission. Also, the inhomogeneous silica shell formation results in deviations in the plasmon-exciton interactions. At parallel orientation when the particle separation is very small, the resulting emission is quenched

because at such small separations plasmon modes cannot be generated in close proximity with the same polarization orientation. Also, as expected all enhancement factors converge to unity as the particle-dipole distance becomes larger because of the vanishing plasmon modes at sufficiently large distances. Finally, we investigated the effect of Au particle size on the enhancement factors at 2 and 5 nm separations between the Au NP and the fluorophore at perpendicular orientation. We observe that the use of 80 nm particles results in the highest enhancement factors, which decreases again at 120 nm particle size. This trend can be explained when considering the penetration depth of gold being 70 nm at around 500 nm. For smaller nanoparticle sizes, electron surface scattering becomes significant, when the mean free path of the conduction electrons is larger than the physical dimension of the nanoparticles.

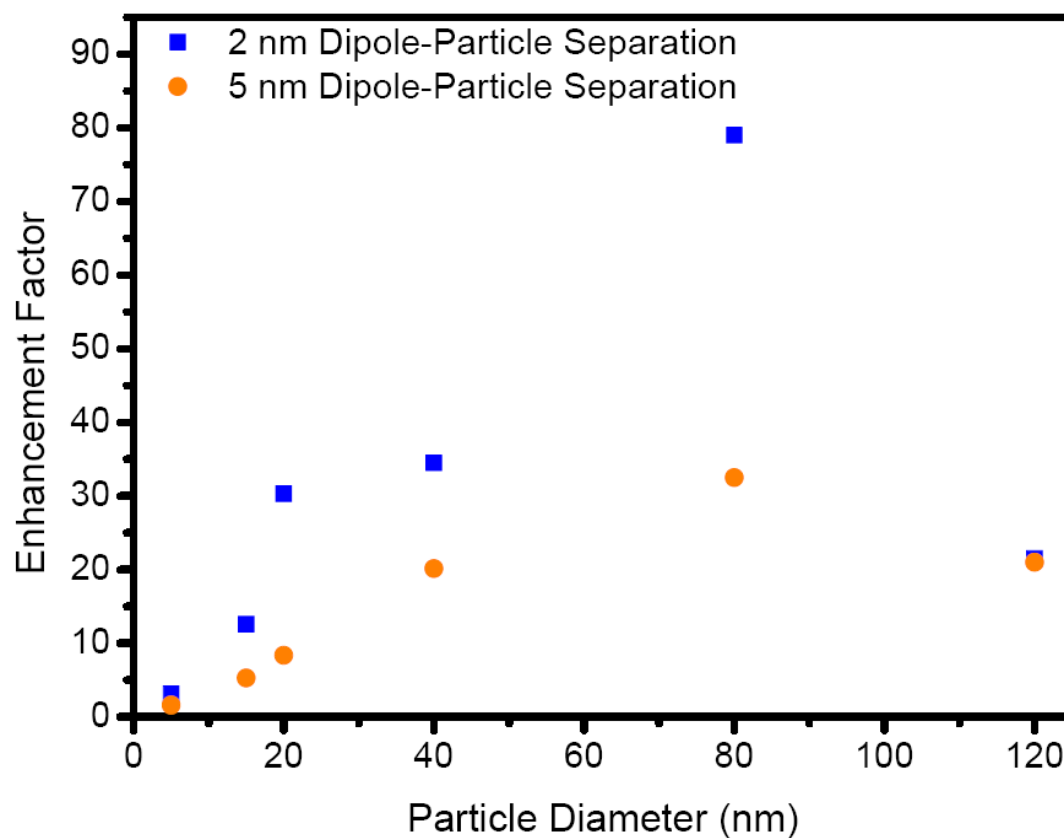


Figure 5.2.2.13. Particle diameter dependence of the simulated enhancement factors at perpendicular orientation for 2 nm (square) and 5 nm (disc) dipole-particle separation using a silica shell.

If the electrons scatter with the surface in a totally random manner, the coherence of the overall plasmon oscillation is disturbed. Our results indicate that by using 15 nm Au particle diameters we are quite below the optimum level at which plasmon enhancement can be maximally observed. Thus, it is possible that emission enhancement can be observed several times higher than our results report. There is a relatively regular trend observed for the data points taken for 5 nm interparticle separations, while it becomes more irregular when this distance is 2 nm.

In conclusion, we successfully developed and demonstrated the synthesis of varying silica shell thicknesses on gold nanoparticles for plasmon-exciton interactions between self-assembled CdTe NCs and Au core nanoparticles. We also performed simulations to investigate normalized decay rates and enhancement factors in relation to the effect of varying particle-dipole separations, polarization orientations, and particle diameters. We observed a strong overlap between computational and experimental results. Maximum emission enhancement factor of 1.97 was observed for a silica shell thickness of 6 nm with a fluorescence quantum efficiency value reaching 39.4% and corresponding decay lifetimes modified from 15.4 ns to 2.1 ns. Our hybrid nano-assemblies are highly promising for potential applications ranging from sensing technologies and solid-state lighting to amplification of surface plasmons.

Chapter 6

Non-Radiative Energy Transfer in Bi-Polymer Nanoparticles of Fluorescent Conjugated Polymers

6.1 Förster Resonance Energy Transfer in Organic Systems

Exhibiting superior optical properties, polyfluorenes have emerged as one of the most promising conjugated polymers for use in solid-state lighting applications. As blue emitters, polyfluorenes retain very high quantum efficiencies [41,104,105,106]. This can be useful for efficient energy transfer from polyfluorene acting as the donor to any lower energy acceptor molecule. Various studies have been carried out to analyze the energy transfer mechanisms, which can be radiative or non-radiative. Radiative energy transfer involves the emission of a photon by the highly energetic polymer and subsequent re-absorption by the acceptor. The non-radiative energy transfer also called resonance energy transfer (RET), on the other hand, is a more efficient and rapid process, which does not

involve emission of a photon from the donor [20]. This process is aided by the coupled dipole-dipole interactions of the donor and acceptor molecules. Since the efficiency of radiative energy transfer is relatively low compared to RET efficiency, the latter mechanism will be of major concern in our study, though Förster mechanism is not necessarily the only one valid in our systems under investigation. Hybrid systems consisting of donor polymer molecules and acceptor dye molecules for energy transfer have been thoroughly studied for many years [107,108,109,110]. These systems are mainly mixtures of donor and acceptor solutions, so that energy transfer takes place among random mixing proximal donor and acceptor molecules. Single donor-acceptor distances cannot be identified for such solutions, for which more complex calculations including the averaging of transfer rates are then required. But, if incidentally donor and acceptor molecules come into close vicinity (at comparable distances with the Förster radius), this process turns out to be efficient; the efficiency of the transfer mechanism is mainly limited by the random distribution of donor and acceptor molecules throughout the solution. A second approach is the energy transfer obtained from hybrid polymer solution-nanocrystal systems, in which nanocrystals are embedded in the energy donating polymer matrix [111,112,113]. The third and last approach, which has been recently developed for several materials, is the combination of donor nanoparticles and acceptor nanoparticles in form of physical mixtures [114,115,116,41,43,104]. Nanostructures used for such purposes are mixtures of NCs, two metal NPs, polymer nanoparticle blends prepared via the reprecipitation or the mini-emulsion methods either by mixing of polymer solutions and then forming NPs or first the formation of polymer NPs and then mixing of NP dispersions. Also, recently blends of polymers and dyes have been described by McNeill and coworkers [117]. This group reported the fluorescence properties and effects of energy diffusion and energy transfer in polyfluorene based nanoparticles, which are doped with various fluorescent dyes. Another study conducted by Scherf and coworkers involves the excitation energy transfer from polymer nanoparticles prepared via the mini-emulsion method to surface-bound Rhodamine 6G [118].

6.2 A New Approach for the Preparation of Dual-Emitting Polymer Nanoparticles

Being very similar to the first approach in terms of the proximities of the donor and acceptor species except for the polymer NPs which are comprised of two different polymers or nano-composites containing both polymer and dye within the same structure, neither of the above mentioned methods allow for the flexibility of construction of different architectures, which may enable the opportunity to search for the most efficient and stable structure.

Here we report novel dual-emitting bi-polymer nanoparticles prepared by the reprecipitation method. Especially, sequentially formed core-shell nanoparticles are of particular interest owing to their enhanced energy transfer efficiencies. Optical measurement results strongly support the formation of such sequential nanoparticles, when compared to the optical behavior of other polymer nanoparticles. To elucidate energy transfer mechanisms among the blue-emitting conjugated polymer derivative of polyfluorene (PF) and the green-emitting PPV-derivative MEH-PPV, we designed four different nanoparticle systems.

In System 1, the nanoparticles of PF and MEH-PPV are prepared separately and mixed after nanoparticle formation. System 2 involved the formation of nanoparticles from a mixture of PF and MEH-PPV solutions, so that polymer chains of each polymer were randomly distributed in each nanoparticle. For Systems 3 and 4, novel assemblies of sequentially formed nanoparticles were obtained. The former one is composed of PF inside and is surrounded by MEH-PPV outside, while the latter is the reverse structure, i.e., MEH-PPV forms the inner structure and PF, the outer structure of the nanoparticles.

6.3 Bi-Polymer Nanoparticle Preparation

To study the energy transfer among fluorescent nanoparticles and their efficiencies, four different systems containing PF and MEH-PPV are designed and synthesized as depicted in Fig. 6.3.1. PF (poly[9,9-dihexyl-9H-fluorene]) was synthesized by the Suzuki coupling of 2,7-dibromo-9,9-dihexyl-9H-fluorene with 9,9-dihexylfluorene-2,7-bis(trimethyleneborate) in a yield of 64%.

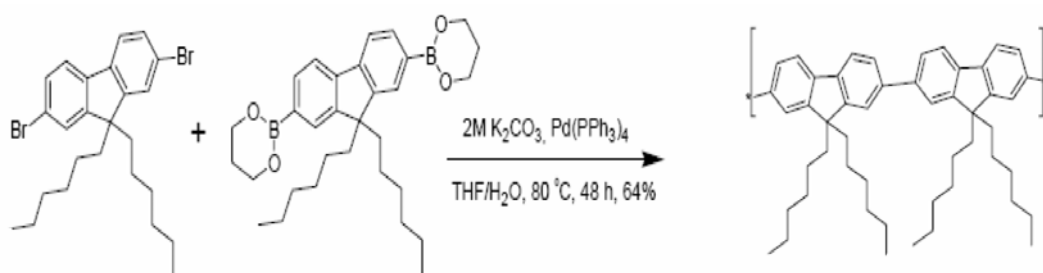


Figure 6.3.1 Synthesis of poly(9,9-dihexyl-9H-fluorene) using 2,7-dibromo-9,9-dihexyl-9H-fluorene and 9,9-dihexylfluorene-2,7-bis(trimethyleneborate) as the monomers.

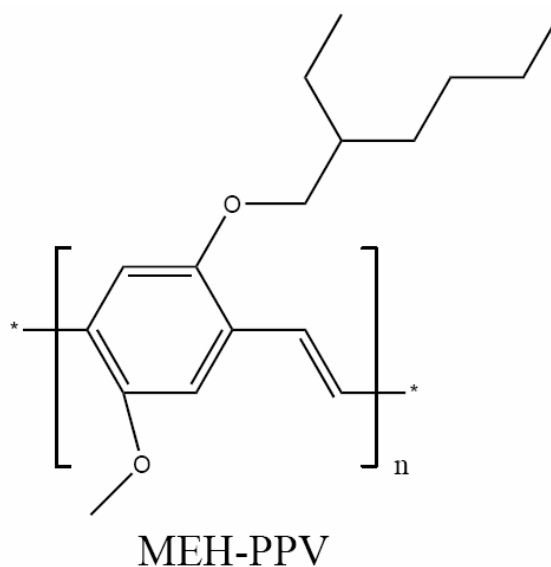


Figure 6.3.2 Chemical structure of poly[2-methoxy-5-(2'-ethyl-hexyloxy)-1,4-phenylene vinylene] (MEH-PPV) purchased from Sigma-Aldrich .

MEH-PPV (poly[2-methoxy-5-(2'-ethyl-hexyloxy)-1,4-phenylene vinylene]) was purchased from Sigma-Aldrich with an average M_n of 70,000-100,000 and was used as received (Fig. 6.3.2). Nanoparticles were prepared using the reprecipitation method as described previously. In this method, the fluorescent conjugated polymer is dissolved in a good solvent (such as THF) and the solution is added into a large amount of poor solvent (usually water) under sonication. The polymer chains are folded in a spherical shape due to hydrophobic effect in a poor solvent to form nanoparticles. To stabilize these nanoparticles and prevent them from dissolving once again in THF, the solvent is evaporated shortly. The size of the nanoparticles can be tuned by varying the concentration of polymer solution and the amount of poor solvent. Using this method, it is possible to obtain a dispersion of nanoparticles in water as small as 5-10 nm.

All polymer solutions and nanoparticle dispersions were prepared by taking the same amounts from the stock PF and MEH-PPV solutions for each set containing a total amount of 32 mL as liquid. The constant concentration of PF used in all sets is 9.0×10^{-3} mM. To obtain two different sets for comparison, the concentration of MEH-PPV was only varied, which will be denoted by **a** and **b**. Based on the molecular weight of the repeating units, these concentrations are calculated to be 4.6×10^{-3} mM and 18.2×10^{-3} mM, respectively. In total, from four nanoparticle systems we prepared eight dispersions for each MEH-PPV concentration **a** and **b**. The preparation of nanoparticles in these four systems is described below:

System 1. Nanoparticles of PF and MEH-PPV polymers are prepared separately from different concentrations of polymer solutions (with PF at its constant concentration, while MEH-PPV is prepared at concentrations **a** and **b**) and are

then mixed at a 1:1 ratio to obtain the mixed-nanoparticle system. The mixtures are denoted by (PF NP + MEH-PPV**a** NP) and (PF NP + MEH-PPV**b** NP), respectively.

System 2. The solutions of PF and MEH-PPV are mixed at two ratios and from this solution nanoparticles are prepared using the reprecipitation method. The resulting nanoparticle mixtures are denoted by (PF + MEH-PPV**a**) mixed NP and (PF + MEH-PPV**b**) mixed NP, respectively.

System 3. PF nanoparticles are prepared first as the cores and MEH-PPV solution is added sequentially to the preformed nanoparticles. With this method we expect to obtain sequentially formed core-shell nanoparticles in which PF is the core and MEH-PPV is the shell as the driving force here is the hydrophobicity of the polymers. For this system we use the following representation, (PF/MEH-PPV**a**) sequential NP and (PF/MEH-PPV**b**) sequential NP.

System 4. It is similar to System 3. However, in this system MEH-PPV constructs the core and PF the shell. These nanoparticles are denoted by (MEH-PPV**a**/PF) sequential NP and (MEH-PPV**b**/PF) sequential NP.

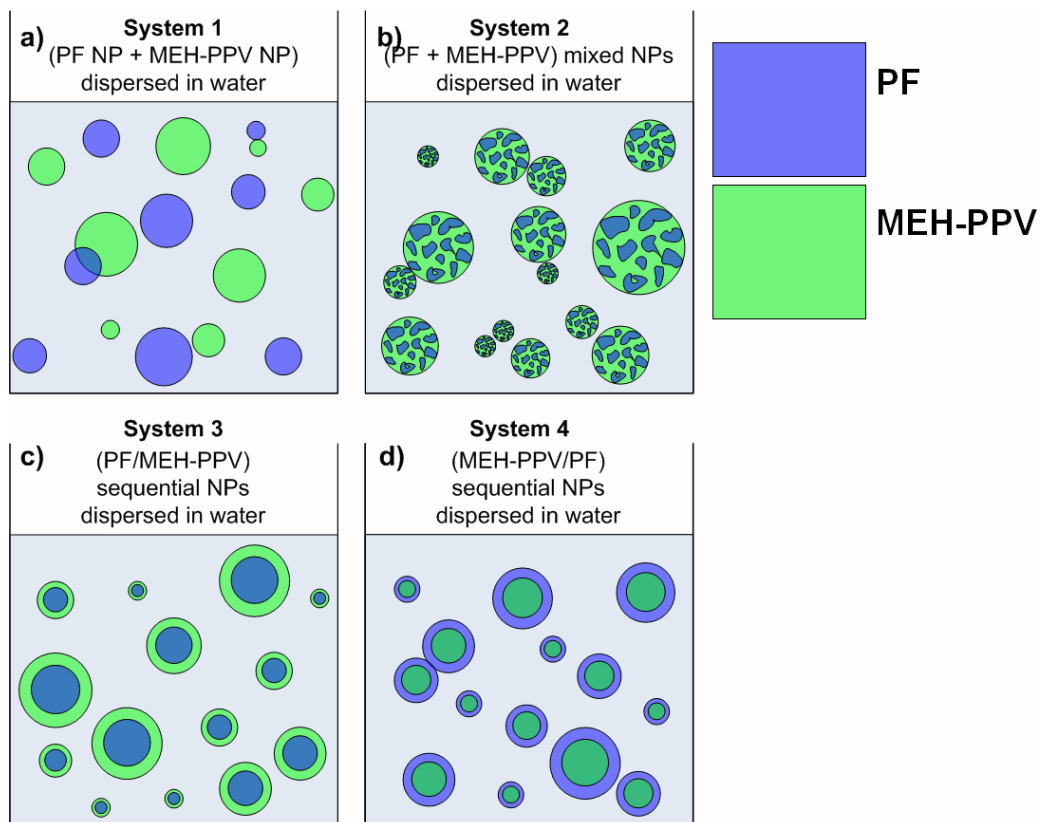


Figure 6.3.3. Schematic representation of the proposed nanostructures for polymer nanoparticles formed from PF and MEH-PPV via the reprecipitation method. (a) System 1: (PF NP + MEH-PPV NP), (b) System 2: (PF + MEH-PPV) mixed NPs, (c) System 3: (PF/MEH-PPV) sequential NPs, and (d) System 4: (MEH-PPV/PF) sequential NPs [].

Though an exact structural determination of each nanoparticle system could not be made, SEM characterization was performed for the films of PF solution, individual PF NP dispersion, MEH-PPV \mathbf{a} NP dispersion and (MEH-PPV \mathbf{a} /PF) sequential NP dispersion as shown in Fig. 6.3.4.

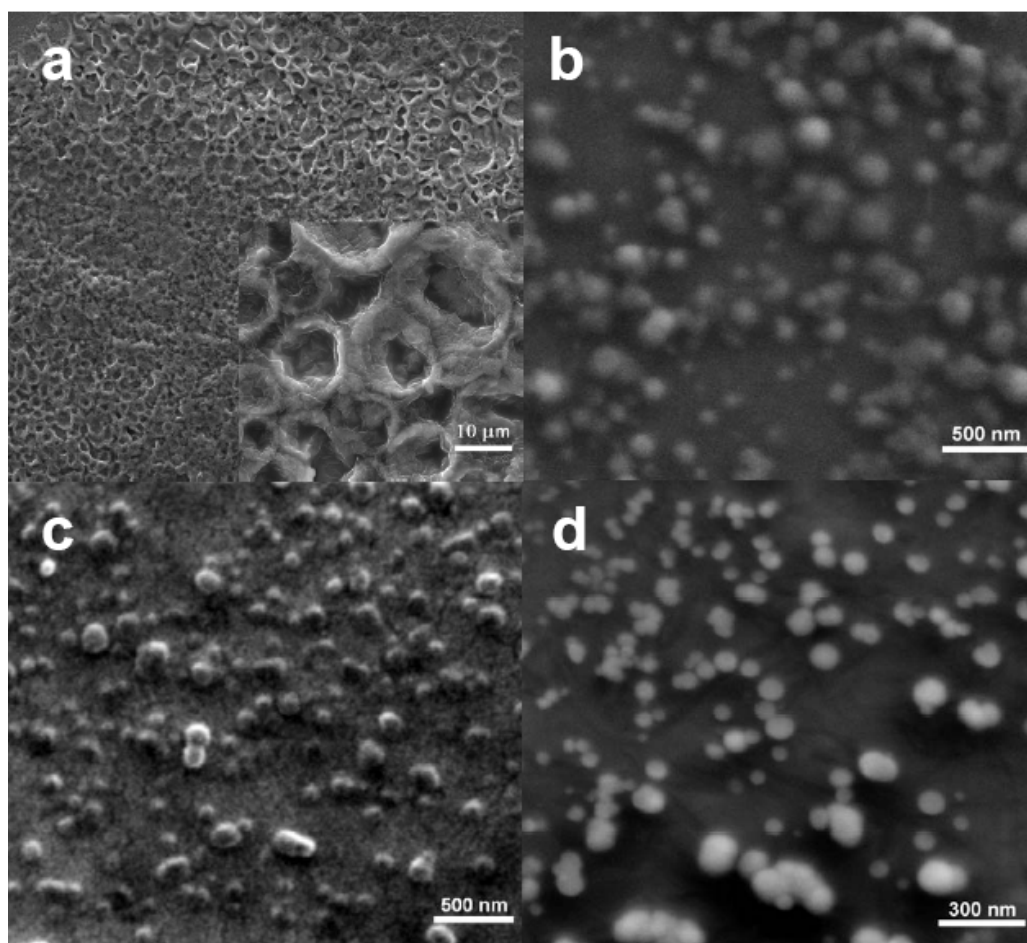


Figure 6.3.4. SEM micrographs of films prepared from (a) PF solution, (b) PF NP dispersion (c) MEH-PPVa NP dispersion, and (d) (MEH-PPVa/PF) sequential NP dispersion. The last image is taken with a tilt angle of 15° [22].

6.4 Experimental Demonstration and Optical Characterization Results

For the investigation of the photophysical properties of our four nanosystems, we run additional control experiments for solutions of PF and MEH-PPV at concentrations **a** and **b** for MEH-PPV. To track changes in energy transfer

efficiencies upon formation of various nano-architectures, we make use of steady-state and time-resolved fluorescence spectroscopy methods.

Collapse of polymer chains into nanoscale spherical particles results in red-shifted emission spectra by over 10 to 41 nm depending on the particle size and type of polymer being folded, as we described recently. Fig. 6.4.1 shows the changes in peak position of PF and MEH-PPV from their solution to nanoparticle dispersion states. Correspondingly, the inset demonstrates the absorption spectra of solutions and their polymer nanoparticle dispersions.

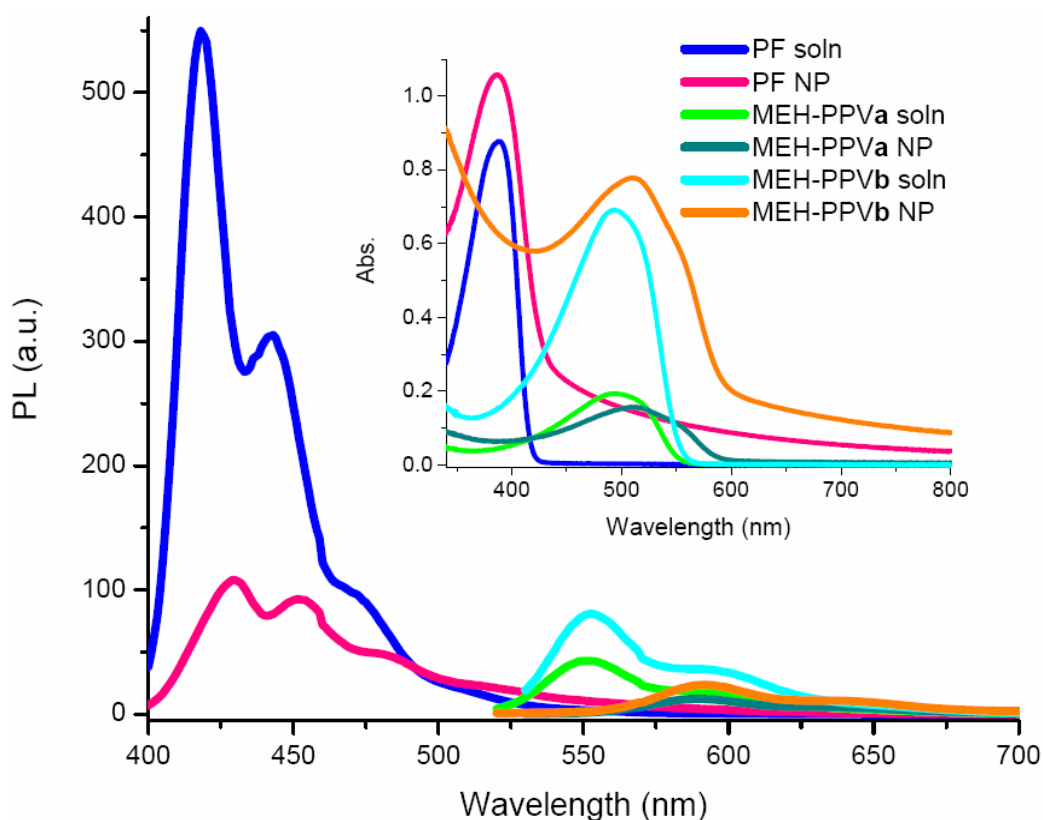


Figure 6.4.1. Onset: Emission spectra of PF solution and its corresponding PF NP dispersion, MEH-PPVa solution and its corresponding MEH-PPVa NP dispersion, and MEH-PPVb solution and its corresponding MEH-PPVb NP dispersion. Inset: Absorption spectra of PF solution and PF NP dispersion, MEH-PPVa solution and MEH-PPVa NP dispersion, and MEH-PPVb solution and MEH-PPVb NP dispersion.

The emission red-shifts from 418 to 429 nm when PF NPs are prepared from the PF solution (at its given concentration). We observe an even more pronounced shift for MEH-PPV**a** NPs changing from 551 to 589 nm and from 552 to 592 nm for MEH-PPV**b** NPs. The emission spectra of only PF NPs and MEH-PPV NPs will be used as reference curves to determine the resulting nanostructure and the energy transfer mechanism, as they provide evidence on how compact NPs are formed and how strongly they interact with each other.

Another measure of the transfer mechanisms is the lifetime of the donating and accepting species. All decay curves could be fitted with two exponentials. For comparison of different systems average intensity weighted lifetimes are under consideration. The average lifetimes are evaluated to be 0.01 ns for PF solution and 0.26 ns for PF NP dispersion. They are 0.32 ns for MEH-PPV**a** solution, 0.33 ns for MEH-PPV**b** solution, 0.51 ns for MEH-PPV**a** NP dispersion and 0.39 ns MEH-PPV**b** NP dispersion. Similar to the trend observed for spectral shifts of polymer species when transformed from the solution state to the dispersion state, we observe an increase in the decay times of the dispersions. This may be due to a retarded emission, which is caused by stacking and kinking of polymer chains within the boundaries of the nanoparticles; this in turn creates a shielded environment.

Control Experiments. Fig. 6.4.2 illustrates the emission spectra of only PF solution, only MEH-PPV solution and also their mixtures.

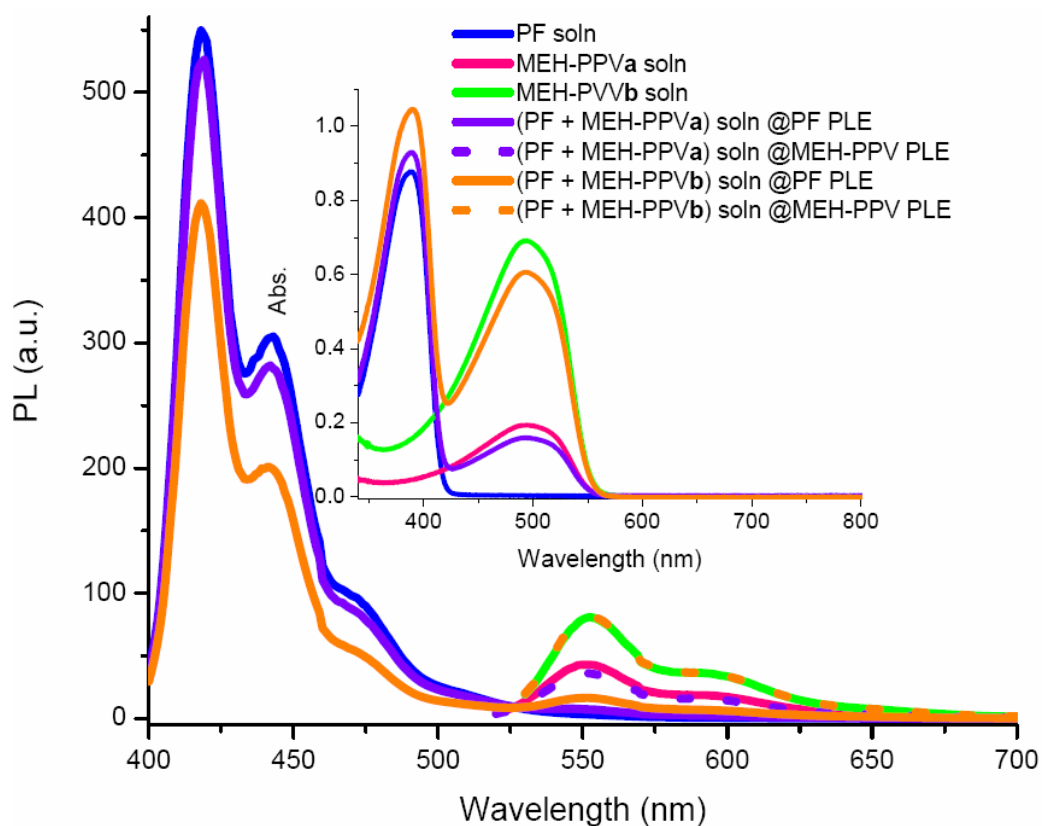


Figure 6.4.2. Onset: Emission spectra of solutions of PF, MEH-PPVa, MEH-PPVb, (PF + MEH-PPVa) and (PF + MEH-PPVb) at absorption maximum of PF (solid) and absorption maximum of MEH-PPV (dotted). Inset: Absorption spectra of PF, MEH-PPVa, MEH-PPVb, (PF + MEH-PPVa), and (PF + MEH-PPVb) solutions.

In the mixture of PF and MEH-PPVa we obtain no emission at around 551 nm at the photoluminescence excitation (PLE) of PF. Lifetimes of PF and MEH-PPVa in solution at 418 nm and 551 nm are found to be 0.01 ns and 0.21 ns. The lack of energy transfer can also be tracked from almost no quenching of the PF peak.

Dealing here with a solution of donor-acceptor pairs which are free to move randomly in solution and thus are not separated by a fixed distance (for example as in the case of control experiments and System 1), it is not appropriate to calculate the energy transfer efficiency by directly using the commonly known expressions (6.1) and (6.2),

$$\eta = 1 - \frac{\tau_{DA}}{\tau_D} \quad (6.1)$$

where τ_{DA} and τ_D denote the average weighted lifetimes of the donor in the presence and absence of acceptor, respectively, and

$$\eta = 1 - \frac{F_{DA}}{F_D} \quad (6.2)$$

where F_{DA} and F_D denote the peak photoluminescence intensity level of the donor in the presence and absence of acceptor [20]. However, it is worth noting that these equations can be safely applied for Systems 2, 3 and 4, where the distance between the donor and acceptor is fixed. The Förster radius of this solution is calculated to be 4.4 nm according to;

$$R_0^6 = \frac{9000(\ln 10)\kappa^2 Q_D}{128\pi^5 N n^4} \int_0^\infty F_D(\lambda) \varepsilon_A(\lambda) \lambda^4 d\lambda \quad (6.3)$$

where Q_D is the quantum yield of the donor (taken to be 80% in solution), κ is the orientation factor (taken to be 2/3 for randomly distributed orientation), N is Avogadro's number, n is the refractive index (taken to be approximately 1.4 for THF solution), $F_D(\lambda)$ is the experimentally measured photoluminescence spectrum of the donor and $\varepsilon_A(\lambda)$ is the extinction coefficient of the acceptor. To estimate the transfer efficiency for this case, we calculate the relative steady-state quantum yield of the donor by

$$\frac{F_{DA}}{F_D} = 1 - \pi^{1/2} \gamma \exp(\gamma^2) [1 - \text{erf}(\gamma)] \quad (6.4)$$

where $erf(\gamma) = \frac{2}{\pi^{1/2}} \int_0^\gamma \exp(-x^2) dx$ with $\gamma = C_A / C_A^0$ and C_A being the acceptor concentration, and $C_A^0 = \frac{3000}{2\pi^{3/2}NR_0^3}$ (in moles/liter) for the case of control

experiments and System 1 with varying D-A distances [20]. Using these expressions the transfer efficiency is estimated to be 0.15%. For an increased amount of acceptor molecules lifetimes are found to be 0.01 ns and 0.36 ns at 418 nm and 552 nm, respectively. This is a result of reduced donor-acceptor molecule distances as donor molecules are surrounded by a larger amount of acceptor molecules with increased MEH-PPV concentration. The resulting transfer efficiency of this system is 0.61%. However, still we are far off the range at which donor and acceptor molecules can interact efficiently. Thus, the design of new NP systems embedding both polymer species becomes a crucial step for the realization of efficient energy transfer, which could be especially useful for white light generation applications.

System 1. In System 1, in which separately formed nanoparticles of PF and MEH-PPV are mixed in a 1:1 ratio after nanoparticle formation, we observe that similar to the previous case the emission peak positions do not change with respect to their original states. The photoluminescence (PL) curves exhibit two peaks at 429 nm and 589 nm for the (PF NP + MEH-PPV \mathbf{a} NP) dispersion and 429 nm and 592 nm for the (PF NP + MEH-PPV \mathbf{b} NP) dispersion (Fig. 6.4.3). In terms of proximities and as a result, the interaction abilities of the donor and acceptor species these formerly mentioned two systems are similar to each other. Though in this system the distances between donor and acceptor, should be seen as doubled, since the donor and acceptor concentration are reduced to half the initial concentration. This becomes also evident from the very low energy transfer efficiencies, which are calculated to be 0.04% for (PF NP + MEH-PPV \mathbf{a} NP) and 0.21% for (PF NP + MEH-PPV \mathbf{b} NP). The energy transfer efficiencies are not calculated from lifetimes of the donor with and without donor using (6.1), as

there are no fixed D-A distances similar to the solution of PF and MEH-PPV considered above. For this system we use (6.3) to calculate the transfer efficiencies. The estimated D-A distances are found to be 13.3 nm and 10.8 nm, respectively.

The concentration of each species in the mixtures of PF NPs and MEH-PPV NPs given in Fig. 6.4.3 is reduced to half the initial value, since the individual nanoparticle dispersions are mixed in a 1:1 ratio. In order to obtain an estimate of the reference donor emission without acceptor as well as acceptor emission without donor, one may consider the curves given in Fig. 6.4.3 of PF NP and MEH-PPV NP multiplied by 0.5.

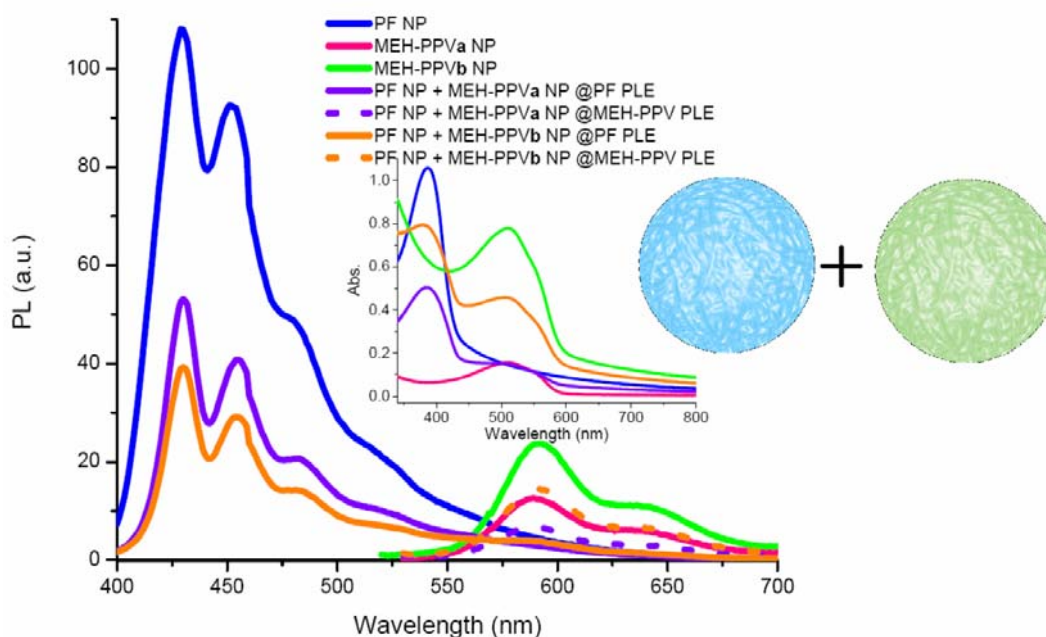


Figure 6.4.3. Onset: Emission spectra of PF NP, MEH-PPVa NP, MEH-PPVb NP dispersions and their corresponding mixtures in a 1:1 ratio as (PF NP + MEH-PPVa NP) and (PF NP + MEH-PPVb NP) at absorption maximum of PF (solid) and MEH-PPV (dotted), respectively. The concentration of each species in the NP mixtures is reduced by a factor of two due to mixing. **Inset:** Absorption spectra of PF NP, MEH-PPVa NP, MEH-PPVb NP dispersions and their mixtures in a 1:1 ratio, (PF NP + MEH-PPVa NP) and (PF NP + MEH-PPVb NP).

System 2. In the second bi-polymer NP system, NPs were formed by mixing solutions of PF and MEH-PPV in two different PF to MEH-PPV ratios and pouring those into 32 mL deionized and sonicated water. This way, we achieve the formation of NPs which contain both species in one NP. Evidence to this is given by the spectral changes as presented in Fig. 6.4.4, which we observe with respect to the peaks of only PF and MEH-PPV NPs. For the (PF + MEH-PPV_a) mixed NPs, the peak of PF appears at 425 nm and that of MEH-PPV at 569 nm. However, when the bi-polymer system is excited at approximately 520 nm to give maximum emission of MEH-PPV only, we observe an emission at 577 nm.

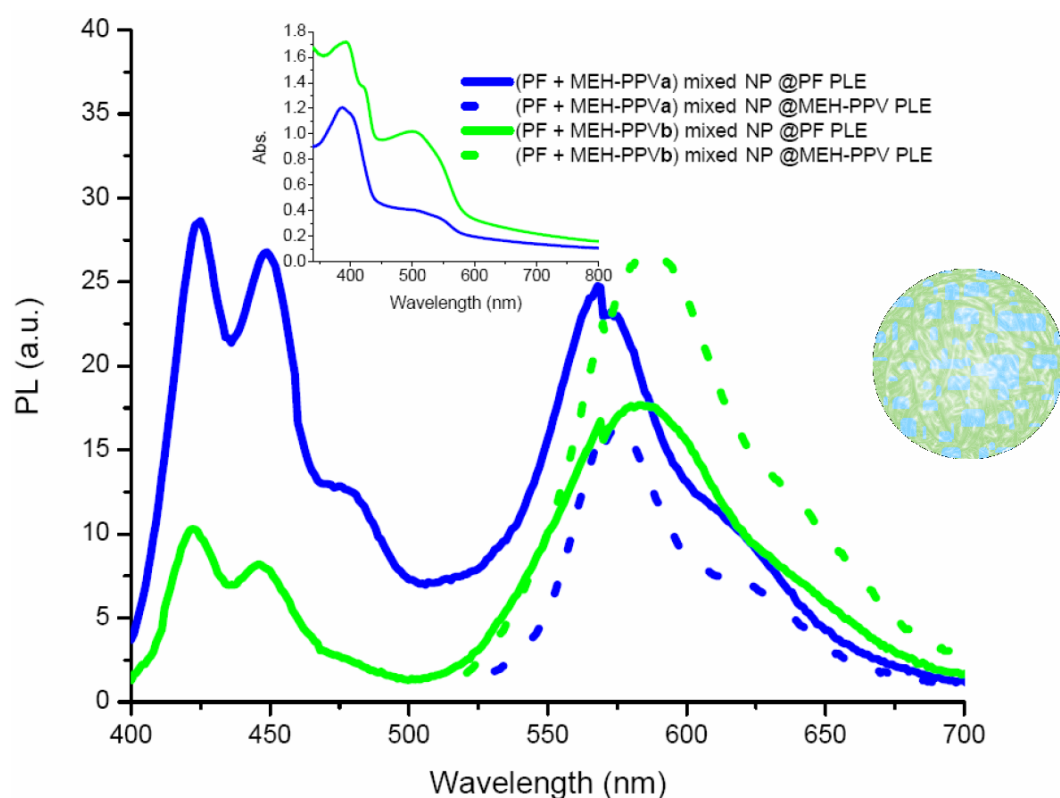


Figure 6.4.4. Onset: Emission spectra of (PF + MEH-PPV_a) and (PF + MEH-PPV_b) mixed NPs at absorption maximum of PF (solid) and MEH-PPV (dotted). Inset: Corresponding absorption spectra of (PF + MEH-PPV) mixed NPs.

The blue-shifted emission at 577 nm of our mixed NPs at PLE of MEH-PPV with respect to the peak observed at 589 nm for only MEH-PPV NPs, shows that the intrinsic nature of our NPs has changed. The fact that MEH-PPV chains are randomly separated by other PF chains reduces the effective conjugation length of the polymer chains, while the competing intra- and interchain forces resulting from chain folding and stacking have still a red-shifting effect on the emission. The emission at 569 nm of the MEH-PPV species in the bi-polymer system, when we use a pump light at 380 nm so that PF is excited, is probably caused by increased donor-acceptor interactions. The increased oscillating dipole-dipole interactions upon excitation of PF create a nearby electric field, which may shorten the excitonic lifetime. This means that the excitons do not have time to find their minima on the MEH-PPV chains and thus emit at higher energies. In this system, as we do not really have a corresponding reference for the PF emission without acceptor molecules, we can only speculate on the efficiency of energy transfer and quenching of the PF peak. Time-resolved measurements turn out to give average lifetimes of 0.21 ns and 0.69 ns at 425 nm and 569 nm, respectively. Using (6.1), the transfer efficiency for (PF + MEH-PPV**a**) mixed NPs is calculated to be 19%, while this value is only an approximation since the lifetime of only PF NPs is used for τ_D . However, it is certainly clear that this approach is more efficient when compared to System 1 and the mixtures in solution. For (PF + MEH-PPV**b**) mixed NPs the efficiency is calculated to be 15% as structural changes are even more compared to (PF + MEH-PPV**a**) mixed NPs. Though an increased efficiency is expected because of an increased amount of acceptor molecules, the fact that the total volume of THF solution injected into sonicated water is too much strongly indicates the failure of properly formed nanoparticles. The mixed NPs from (PF + MEH-PPV**b**) emit at 422 nm and 583 nm when excited at the maximum absorption wavelength of PF, and emit at 588 nm when excited at the maximum absorption of MEH-PPV.

Systems 3 and 4. In our next approach, we analyze the novel bi-polymer nanoparticles, which have been prepared using alternating polymers in a sequential manner. By this method, we are able to construct the inside of NPs from one polymer while the surrounding layer is made of the other polymer. Our aim is to achieve pure material properties on each polymer domain, while keeping them at distances comparable with the Förster radius. Emission and corresponding absorption spectra of (PF/MEH-PPV) sequential NPs are given in Fig. 6.4.5. At the PLE of MEH-PPV the emission peaks are at 587 nm and 589 nm for concentrations **a** and **b**, which almost perfectly matches with the emission peaks of only MEH-PPV**a** and MEH-PPV**b** NPs at 589 nm and 592 nm, respectively. Little changes result from the fact that MEH-PPV is now surrounding the inner core consisting of PF, thus forming a looser structure as a shell. Excitation of the (PF/MEH-PPV) sequential NPs at the PLE of PF results on the other hand in a blue-shifted MEH-PPV emission by 21 to 7 nm for concentrations **a** and **b** with respect to the emission of MEH-PPV at PLE of MEH-PPV. This effect was already observed above for the other systems. When MEH-PPV is sequentially added to the PF NPs, the PF emission is quenched. The average lifetimes of (PF/MEH-PPV**a**) sequential NPs are fitted by two exponentials to be 0.20 ns at 429 nm and 1.22 ns at 566 nm, while we measure 0.20 ns and 0.67 ns for (PF/MEH-PPV**b**) sequential NPs at 425 nm and 582 nm, respectively. Time-resolved spectra for individual PF and MEH-PPV**a** NPs at 429 nm and 589 nm and (PF/MEH-PPV**a**) sequential NPs at 429 nm and 566 nm are given in Fig. 6.4.6. The energy transfer efficiency for the former dispersion is calculated to be 23%, using (6.1). Since the whole PF domain is surrounded by a MEH-PPV domain, MEH-PPV exhibits almost the same emission characteristics in the structure when it is excited at its own maximum absorption wavelength in both cases **a** and **b**. At the maximum absorption wavelength of PF, we observe that especially for the (PF/MEH-PPV**a**) sequential NP system the emission of MEH-PPV is much more blue-shifted (21 nm) with respect to the MEH-PPV emission at the PLE of MEH-PPV in that corresponding system, than in all other cases. There are two reasons for this observation. The first reason is that there

exists a strong interaction between donor and acceptor molecules, which results in the decay of acceptor molecules at shorter wavelengths as has been observed also above for the second structure.

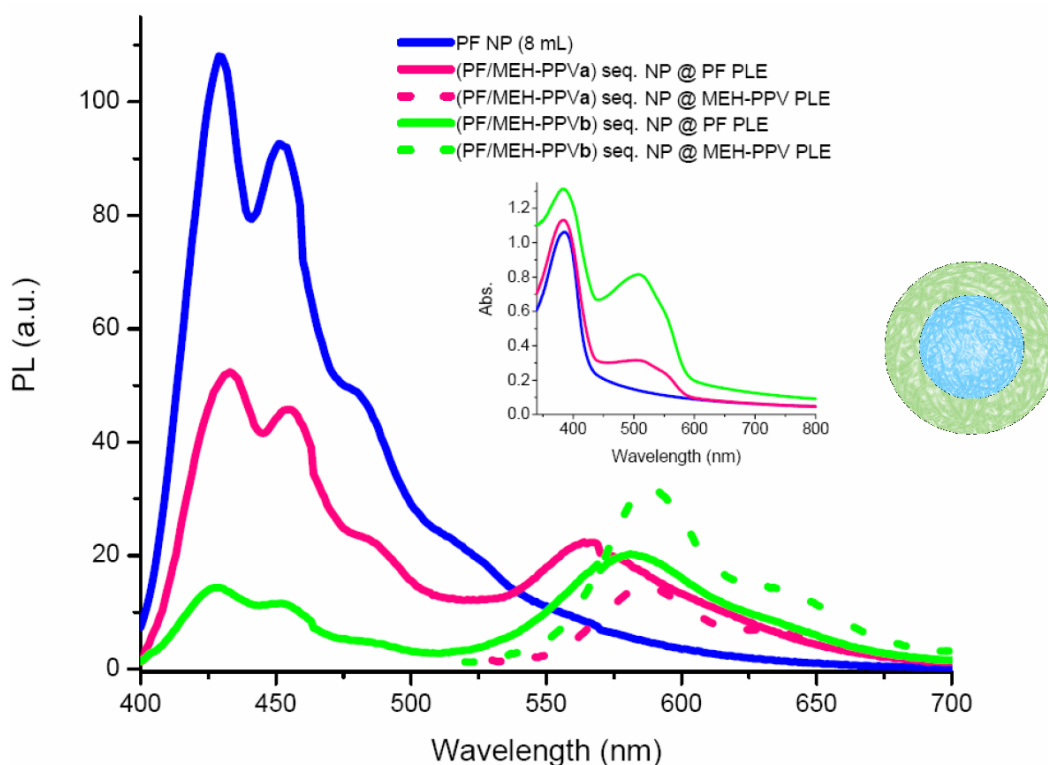


Figure 6.4.5. Onset: Emission spectra of PF NPs, (PF/MEH-PPVa) sequential NPs at absorption maximum of PF (solid) and MEH-PPV (dotted), and (PF/MEH-PPVb) sequential NPs at absorption maximum of PF (solid) and MEH-PPV (dotted) Inset: Absorption spectra of PF NPs and (PF/MEH-PPV) sequential NPs.

The second reason for the large shift when compared specifically to the b sample is that in the former structure there is a thinner layer of MEH-PPV so that all acceptor molecules strongly interact with the donor molecules. Evidence for the fact that MEH-PPV molecules really mostly surround the PF NPs in dispersion a, but do not form separate MEH-PPV NPs is the emission peak of MEH-PPV at 587 nm instead of 589 nm for MEH-PPV when we excite the system at the maximum absorption of MEH-PPV. Even stronger evidence however is the

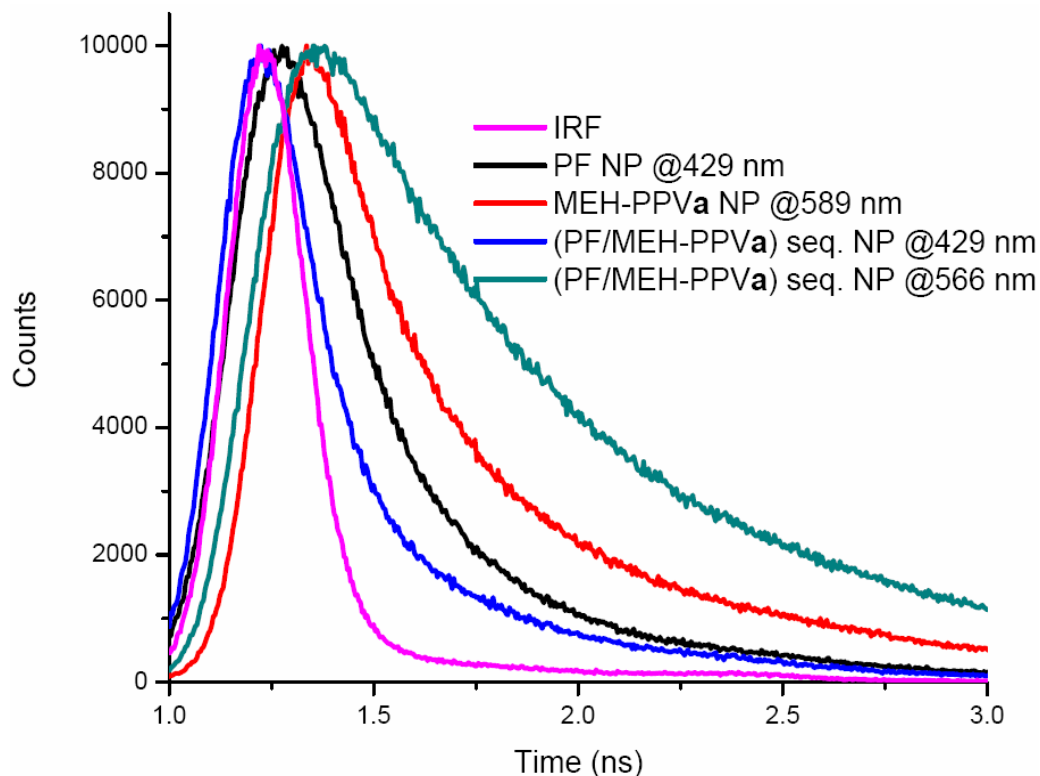
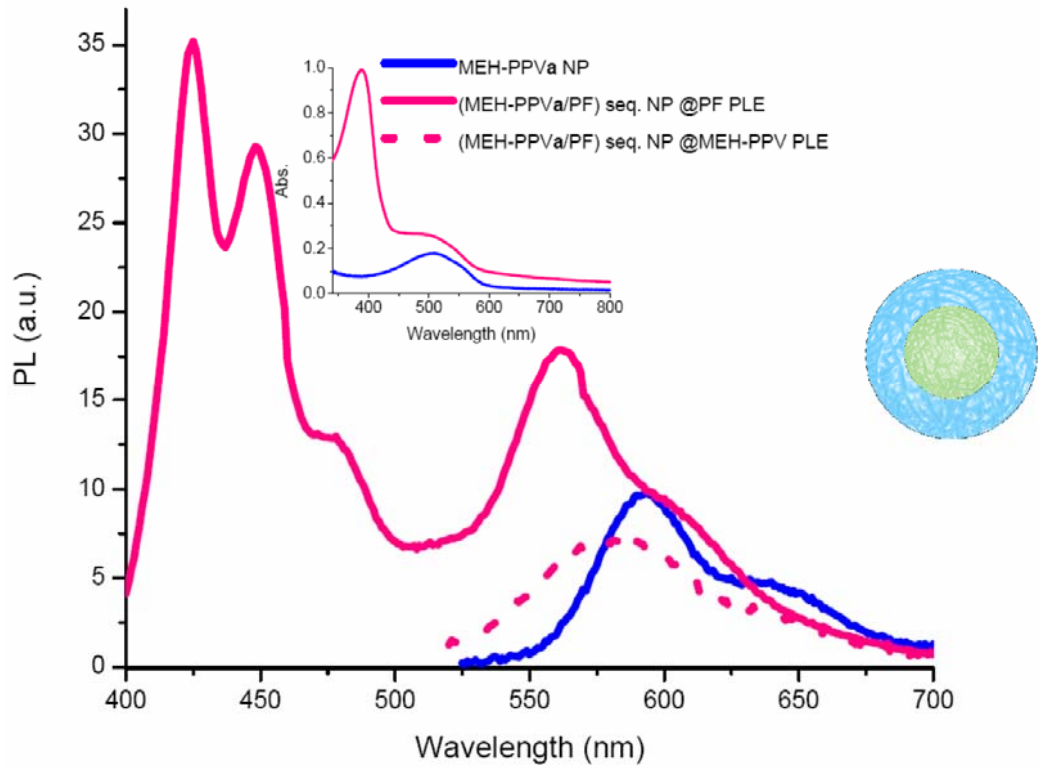


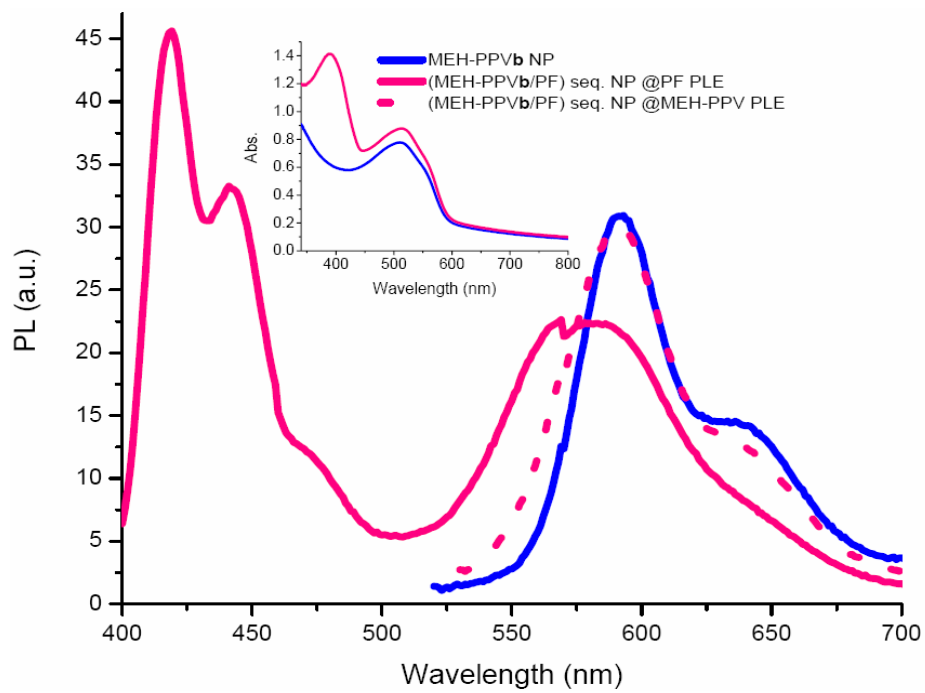
Figure 6.4.6. Biexponentially fitted decay curves of PF NPs at 429 nm (0.26 ns), MEH-PPVa NPs at 589 nm (0.51 ns) and (PF/MEH-PPVa) sequential NPs at 429 nm (0.20 ns) and 566 nm (1.22 ns). Reported lifetimes are average intensity weighted values and decay fit parameter “R” ranges from 0.8 to 1.2.

pronounced blue-shifted emission of MEH-PPV at the PLE of PF with respect to the emission of MEH-PVP at PLE of MEH-PPV. This is not exactly the case for the latter dispersion, as MEH-PPV blue-shifts merely 7 nm. This indicates that there is a reduced interaction between PF and MEH-PPV as more MEH-PPV chains have formed individual NPs.

Finally, there is the last nanoparticle system as shown in Fig. 6.4.7, which is very similar to the previous one, except that MEH-PPV forms the inner structure while the PF layer surrounding it, is sequentially formed later. For this system as in the second structure with mixed nanoparticles, we also do not have a reference initial



(a)



(b)

Figure 6.4.7. a) Onset: Emission spectra of MEH-PPV NPs, (MEH-PPV \mathbf{a} /PF) sequential NPs at absorption maximum of PF (solid) and MEH-PPV (dotted). Inset: Absorption spectra of MEH-PPV NP \mathbf{a} and (MEH-PPV \mathbf{a} /PF) sequential NPs. b) Onset: Emission spectra of MEH-PPV \mathbf{b} NPs, (MEH-PPV \mathbf{b} /PF) sequential NPs at absorption maximum of PF (solid) and MEH-PPV (dotted). Inset: Absorption spectra of MEH-PPV \mathbf{b} NP and (MEH-PPV \mathbf{b} /PF) sequential NPs.

PF emission spectrum without acceptor molecules, so that it is not possible to directly calculate the energy transfer efficiency from the quenching of the donor emission.

An important fact about the donor emissions in both sets is that though further quenching of donor emission is expected for (MEH-PPV \mathbf{b} /PF) sequential NPs due to increased acceptor concentration, this is not the case. This is probably a morphological effect resulting from higher photoluminescence efficiency of the thinner PF layer formed around MEH-PPV \mathbf{b} , whereas the thicker PF layer around MEH-PPV \mathbf{a} , subject to serious inter- and intramolecular interactions, leads to reduced emission intensity of PF chains which are not involved in the non-radiative energy transfer mechanism. The elusory higher intensity of MEH-PPV emission in (MEH-PPV \mathbf{b} /PF) sequential NPs comes from the fact that the tail of PF emission is higher in intensity when compared to (MEH-PPV \mathbf{a} /PF) sequential NPs. Since this time PF forms the outer structure of our sequentially formed nanoparticles, losses due to reflection or several other non-radiative processes are not of major concern, so that the expected energy transfer efficiency of this approach might be higher than calculated for the reverse structure above. Indeed, the calculated transfer efficiency for (MEH-PPV \mathbf{a} /PF) sequential NPs is 35%, which is the highest calculated energy transfer efficiency of all structures. This makes this structure a promising candidate in terms of efficiency for use in energy transfer in dual-color emitting systems. Time-resolved measurements show 0.17 ns at 425 nm and 0.90 ns at 561 nm for sample a. Decay curves for

individual PF and MEH-PPV \mathbf{a} NPs at 429 nm and 589 nm and (MEH-PPV \mathbf{a} /PF) sequential NPs at 425 nm and 561 nm are given in Fig. 6.4.8.

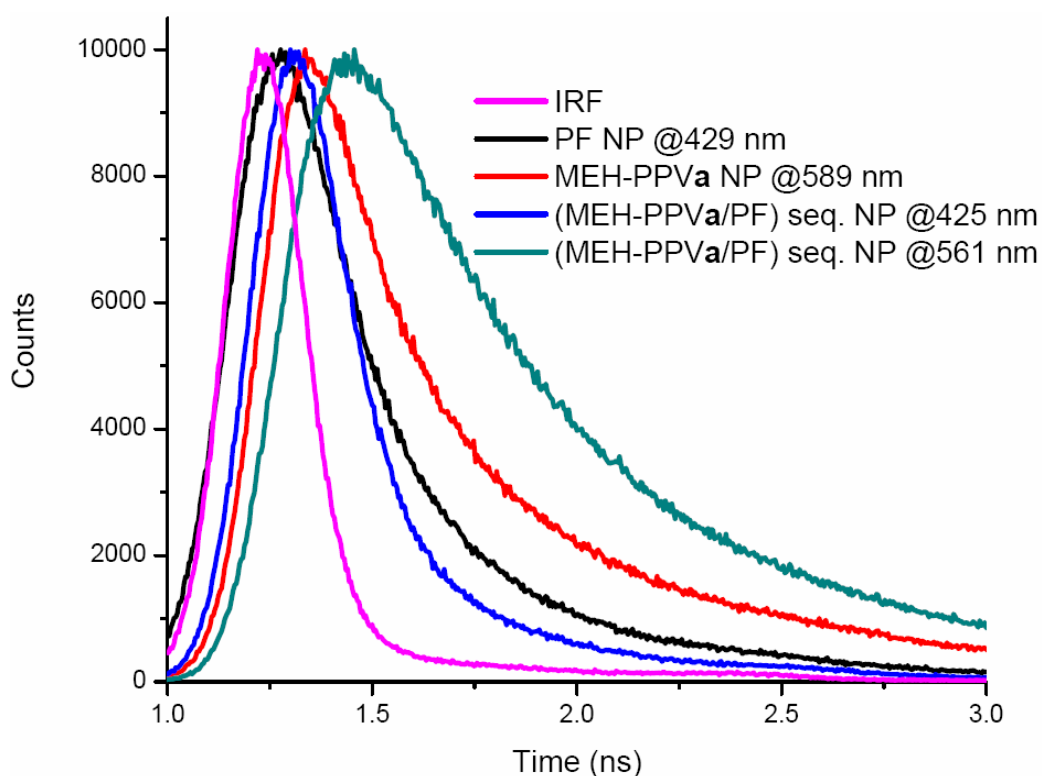


Figure 6.4.8. Biexponentially fitted decay curves of PF NPs at 429 nm (0.26 ns), MEH-PPV \mathbf{a} NPs at 589 nm (0.51 ns) and (MEH-PPV \mathbf{a} /PF) sequential NPs at 425 nm (0.17 ns) and 561 nm (0.90 ns). Reported lifetimes are average intensity weighted values and decay fit parameter “R” ranges from 0.8 to 1.1.

Similar arguments as were discussed for (PF/MEH-PPV) sequential nanoparticles hold for the formation of (MEH-PPV/PF) sequential NPs. Evidence for the fact that we formed bi-polymer nanoparticles, but not separate PF and MEH-PPV NPs, is the emission peak position of the outer polymer domain, in this case the PF layer. For sample a as the PF layer is thicker we observe an emission at 425 nm, which shows that PF did not form separate NPs emitting normally at 429 nm. PF in sample b on the other hand emits at 419 nm, which shows really how thin the PF layer on the inner MEH-PPV domain is, so that its emission characteristics

have almost not changed in comparison to the PF solution. A second evidence for the verification of the resulting structure is also the slightly blue-shifting MEH-PPV emission at PLE of PF, which shows that PF and MEH-PPV domains are in very close proximity.

In summary, we successfully showed differences in the optical behavior of four differently designed polymer nanosystems. Resonance energy transfer efficiencies of these systems were calculated to explicitly discover the most useful structure. The solution mixtures of PF and MEH-PPV as well as System 1, in which we have a mixture of individual PF NPs and MEH-PPV NPs, exhibit almost the same low values of energy transfer efficiencies. In principle both systems have large donor-acceptor separations, which in turn results in low transfer efficiency values. The systems prepared by keeping donor and acceptor molecules within a closer distance, show significantly improved efficiencies, around 10 times higher or more. The highest energy transfer efficiency was recorded for the (MEH-PPV_a/PF) sequential NP system.

The studies of energy transfer in the four systems using steady-state and time-resolved fluorescent spectroscopy reveal that the nanoparticles of the first approach show no acceptor emission. The nanoparticles of the second approach show a considerably stronger emission for the acceptor while donor emission is suppressed. The Förster radius for the system composed of individual PF nanoparticles and MEH-PPV nanoparticles has been calculated to be 3.6 nm and 3.9 nm, for two different MEH-PPV concentrations a and b. The sequential hybrid nanoparticles prepared in the third and fourth approaches show remarkably higher energy transfer efficiencies as high as 35%

Chapter 7

Conclusion

In this thesis, we worked on the investigation and development of highly efficient emitters using two different energy transfer mechanisms; resonance energy transfer between metal nanoparticles and nanocrystals, and Förster resonance energy transfer between two different conjugated polymers, namely PF and MEH-PPV. We introduced some basic terminology on conjugated polymers and polyfluorenes and on semiconducting nanocrystals, their synthesis and optical characterization. We also introduced fundamentals of surface plasmons and explained the effective parameters on the surface plasmon resonance frequency.

In the next chapters we presented our experimental details and characterization results. First, we reported on modified CdTe NC emission kinetics using plasmonic coupling in hybrid Au-silica core/shell nanoparticles furnished with CdTe nanocrystals. We studied the optimization of plasmon-exciton interactions by varying the silica shell thickness between the NC emitters and gold core. We also made a thorough investigation of the effects of various parameters including shell thickness and metal particle diameter on the enhancement factors by using FDTD numerical simulations. Experimentally, we observed enhanced emission up to a factor of 1.97 resulting in a quantum efficiency of 39.4% along with decay lifetimes modified from 15.4 ns to 2.1 ns for only CdTe NCs and the NC emission decorated on the hybrid nanoparticle, respectively.

Additionally, we demonstrated the comparative studies of non-radiative resonance energy transfer in bi-polymer nanoparticles based on fluorescent conjugated polymers. For this purpose, four different bi-polymer nanoparticle systems were designed and synthesized. Both steady-state fluorescence spectra and time-resolved fluorescence measurements indicated varying energy transfer efficiencies from the donor polymer PF to the acceptor polymer MEH-PPV depending on the D-A distances and structural properties of the nanoparticles. The highest energy transfer efficiency recorded to be 35% is obtained from the last core-shell type nanoparticle system, in which a PF layer is sequentially formed on MEH-PPV NPs.

During this thesis work, we published an SCI paper from Chapter 6 as given in the reference. We are also in the preparation process of Chapter 5 to an SCI journal. Moreover, the material included in Chapter 6 has been presented at a refereed international conference, while the material in Chapter 5 was recently submitted to a refereed international conference.

BIBLIOGRAPHY

-
- [1] G. Cao, *Nanostructures & Nanomaterials*. Imperial College Press, 2007.
- [2] G. Heliotis, P. N. Stavrinou, D. D. C. Bradley, E. Gu, C. Griffin, C. W. Jeon and M. D. Dawson, *Appl. Phys. Lett.*, **87**, 2005, 103505.
- [3] F. Hide, P. Kozodoy, S. P. DenBaars and A. Heeger, *Appl. Phys. Lett.*, **70**, 1997, 2664.
- [4] J. K. Sheu, S. J. Chang, C. H. Kuo, Y. K. Su, L. W. Wu, Y. C. Lin, W. C. Lai, J. M. Tsai, G. C. Chi and R. K. Wu, *IEEE Photon. Technol. Lett.*, **15**, 2003, 18.
- [5] N. Hirosaki, R.-J. Xie, K. Kimoto, T. Sekiguchi, Y. Yamamoto, T. Suehiro and M. Mitomo, *Appl. Phys. Lett.*, **86**, 2005, 211905.
- [6] A. Kraft, C. Grimsdale and A. B. Holmes, *Angew. Chem.*, **37**, 1998, 402.
- [7] B. W. D'Andrade, R. J. Holmes and S. R. Forrest, *Adv. Mater.*, **16**, 2004, 624.
- [8] T. A. Skotheim and R. L. Elsenbaumer, *Handbook of Conducting Polymers*, Marcel Dekker, New York, 1998.
- [9] H. V. Demir, S. Nizamoglu, T. Ozel, E. Mutlugun, I. O. Hoyal, E. Sari, E. Holder and N. Tian, *New J. Phys.*, **9**, 2007, 362
- [10] M. Mazzeo, V. Vitale, F. D. Sala, M. Anni, G. Barbarella, L. Favaretto, G. Sotgiu, R. Cingolani and G. Gigli, *Adv. Mater.*, **17**, 2005, 34
- [11] J. Luo, X. Li, Q. Hou, J. Peng, W. Yang and Y. Cao, *Adv. Mater.*, **19**, 2007, 1113.
- [12] J. Liu, Q. Zhou, Y. Cheng, Y. Geng, L. Wang, D. Ma, X. Jing and F. Wang, *Adv. Mater.*, **17**, 2005, 2974.
- [13] J. Liu, Z. Xie, Y. Cheng, Y. Geng, L. Wang, X. Jing and F. Wang, *Adv. Mater.*, **19**, 2007, 531.
- [14] J. Liu, S. Shao, L. Chen, Z. Xie, Y. Cheng, Y. Geng, L. Wang, X. Jing and F. Wang, *Adv. Mater.*, **19**, 2007, 1859.
- [15] G. Tu, C. Mei, Q. Zhou, Y. Cheng, Y. Geng, L. Wang, D. Ma, X. Jing and F. Wang, *Adv. Funct. Mater.*, **16**, 2006, 101.
- [16] J. Jiang, y. Xu, W. Yang, R. Guan, Z. Liu, H. Zhen and Y. Cao, *Adv. Mater.*, **18**, 2006, 1769.
- [17] K. Hosoi, *Thin Solid Films*, **12**, 2003, 438.

-
- [18] R. H. Lambeth, *Electroluminescence of Conjugated Aromatic Polymers in Organic Light Emitting Diodes*, 2005.
- [19] S. K. Lee, N. S. Cho, J. H. Kwak, K. S. Lim, H. Shim, D. Hwang, C. J. Brabec, *Thin Solid Films*, **157**, 2006, 511.
- [20] J. R. Lakowicz, *Principles of Fluorescence Spectroscopy*, Plenum Publishing Corporation, 2nd edition, 1999.
- [21] T. Förster, *Ann. Physik*, **437**, 1948, 55.
- [22] I. O. Ozel, T. Ozel, H.V. Demir, and D. Tuncel, *Opt. Express*, **18**, 2010, 670.
- [23] S. Nizamoglu, T. Ozel, E. Sari and H. V. Demir, *Nanotechnology*, **18**, 2007, 065709.
- [24] E. Mutlugun, I. M Soganci, and H. V. Demir, *Opt. Express*, **16**, 2008, 3537.
- [25] D. Alexson, H. Chen, M. Cho, M. Dutta, Y. Li, P. Shi, A. Raichura, D. Ramadurai, S. Parikh, M. A. Stroschio and M. Vasudev, *J. Phys. : Condens. Matter.*, **17**, 2005, 637.
- [26] A. A. Chistyakov, I. L. Martynov, K. E. Mochalov, V. A. Oleinikov, S. V. Sizova, E. A. Ustinovich, and K. V. Zakharchenko, *Laser Phys.*, **16**, 2006, 1625.
- [27] D. Harden, *Glass of the Caesars*, exh. cat. London, The British Museum Press, 1988.
- [28] M. Faraday, *Philos. Trans. R. Soc. London*, **147**, 1857, 145.
- [29] G. Mie, *Ann. Phys.*, **25**, 1908, 377.
- [30] C. D. Geddes and J. R. Lakowicz, *J. Fluoresc.*, **12**, 2002, 121.
- [31] A. Otto, I. Mrozek, H. Grabborn and W. Akemann, *J. Phys.: Condens. Matter*, **4**, 1992, 1143.
- [32] T. Y. F. Tsang, *Opt. Lett.*, **21**, 1996, 245.
- [33] H. Kano and S. Kawata, *Opt. Lett.*, **21**, 1996, 1848.
- [34] U. Koldemir, *Conjugated Polymers Based on Polyfluorene Derivatives and Polypyrrole* (M.S. Thesis, 2007).
- [35] S. K. Lee, N. S. Cho, J. H. Kwak, K. S. Lim, H. Shim, D. Hwang, C. J. Brabec, *Thin Solid Films*, **157**, 2006, 511.
- [36] A. Bernanose, *British J. of Appl. Phys.*, 1953.
- [37] D. Vak, C. Chun, C. L. Lee, *J. Mater. Chem.*, **14**, 2004.
- [38] F. Cacialli, J. S. Wilson, J. J. Michels, C. Daniel, C. Silva, R. H. Friend, N. Severin, P. Samorì, J. P. Rabe, M. J. O'Connell, P. N. Taylor, H. L. Anderson, *Nature Materials*, **1**, 2002, 160.
- [39] I. O. Huyal, T. Ozel, D. Tuncel, H. V. Demir, *Opt. Express*, **16**, 2008, 1391.
- [40] D. Marsitzky, R. Vestberg, P. Blainey, B. T. Tang, C. G. Hawker, K. R. Carter, *J. Am. Chem. Soc.*, **123**, 2001, 6965.
- [41] F. Kong, X. L. Wu, G. S. Huang, R. K. Yuan, P. K. Chu, *Thin Solid Films*, 2008.
- [42] C. Syzmanski, C. Wu, J. Hooper, M. A. Salazar, A. Perdomo, A. Dukes, J. McNeill, *J. Phys. Chem B*, **109**, 2005, 8543.
- [43] T. Kietzke, D. Neher, K. Landfester, R. Montenegro, R. Güntner, U. Scherf, *Nature*, **2**, 2003, 408.

-
- [44] N. Kurokawa, H. Yoshikawa, N. Hirota, K. Hyodo, and H. Masuhara, *ChemPhysChem*, **5**, 2004, 1609.
- [45] F. Wang, M.-Y. Han, K. Y. Mya, Y. Wang, and Y.-H. Lai, *J. Am. Chem. Soc.*, **127**, 2005, 10350.
- [46] C. Wu, H. Peng, Y. Jiang, and J. McNeill, *J. Phys. Chem B*, **110**, 2006, 14148.
- [47] X. Wang, J. Zhuang, Q. Peng, Y. Li, *Nature*, **437**, 2005, 121.
- [48] H. Kasai, H. S. Nalwa, H. Oikawa, S. Okada, H. Matsuda, N. Minami, A. Kakuta, K. Ono, A. Mukoh, H. Nakanishi, *Jpn. J. Appl. Phys.*, **31**, 1992, L1132.
- [49] C. Wu, C. Syzmanski, and J. McNeill, *Langmuir*, **22**, 2006, 2956.
- [50] T. Kietzke, D. Neher, M. Kumke, O. Ghazy, U. Ziener, K. Landfester, *Small*, **3**, 2007, 1041.
- [51] V. I. Klimov, *Los Alamos Science*, 28, 2003.
- [52] N. Mal, E. H. Sargent, S. O. Kelley, *Nature Nanotechnology*, **4**, 2009, 121.
- [53] W. J. Parak, D. Gerion, T. Pellegrino, D. Zanchet, C. Micheel, S. C. Williams, R. Boudreau, M. A. Le Gros, C. A. Larabell, A. P. Alivisatos, *Nanotechnology*, **14**, 2003, R15.
- [54] A. Ekimov, *Sov. Glass Phys. Chem.*, **6**, 1980, 511.
- [55] R. Rossetti, R., et al., *J. Chem. Phys.*, **79**, 1983, 1086.
- [56] D. V. Talapin, A. L. Rogach, A. Kornowski, M. Haase and H. Weller, *Nano Lett.*, **1**, 2001, 207.
- [57] S. Kim, B. Fisher, H.-J. Eisler and M. Bawendi, *JACS*, **125**, 2003, 11466.
- [58] G. P. Mitchell, C. A. Mirkin, R. L. Letsinger, *J. Am. Chem. Soc.*, **121**, 1999, 8122.
- [59] C.-C. Chen, C.-P. Yet, H.-N. Wang, C.-Y. Chao, *Langmuir*, **15**, 1999, 6845.
- [60] D. M. Willard, L. L. Carillo, J. Jung, A. V. Orden, *Nano Lett.*, **1**, 2001, 469.
- [61] M. J. Bruchez, M. Moronne, P. Gin, S. Weiss, A. P. Alivisatos, *Science*, **281**, 1998, 2013.
- [62] D. Gerion, F. Pinaud, S. C. Williams, W. J. Parak, D. Zanchet, S. Weiss, A. P. Alivisatos, *J. Phys. Chem. B*, **105**, 2001, 8861.
- [63] M. Giersig, L. M. Liz-Marzan, T. Ung, D. Su, P. Mulvaney, *Ber. Bunsenges. Phys. Chem.*, **101**, 1997, 1617.
- [64] W. J. Parak, D. Gerion, D. Zanchet, A. S. Woerz, T. Pellegrino, C. Micheel, S. C. Williams, M. Seitz, R. E. Bruehl, Z. Bryant, C. Bustamante, C. R. Bertozzi, A. P. Alivisatos, *Chem. Mater.*, **14**, 2002, 2113.
- [65] L. Guo, S. Yang, C. Yang, P. Yu, J. Wang, W. Ge, G. K. Wong, *Appl. Phys. Lett.*, **76**, 2000, 2901.
- [66] M. A. Hines, G.D. Scholes, *Adv. Mater.*, **15**, 2003, 1844.
- [67] S. Nizamoglu, T. Ozel, E. Sari, H. V. Demir, *Nanotechnology*, **18**, 2007, 065709.
- [68] H.-J. Eisler, V. C. Sundar, M. G. Bawendi, M. Walsh, H. I. Smith, V. Klimov, *Appl. Phys. Lett.*, **80**, 2002, 4614.
- [69] M. B. Fischbein, M. Drndic, *Appl. Phys. Lett.*, **86**, 2005, 193106.
- [70] A. J. Nozik, *Physica E*, **14**, 2002, 115.
- [71] E. Mutlugun, I. M Soganci, H. V. Demir, *Opt. Express*, **16**, 2008, 3537.

-
- [72] M. T. Harrison, S. V. Kershaw, M. G. Burt, A. L. Rogach, A. Kornowski, A. Eychmüller, H. Weller, *Pure Appl. Chem.*, **72**, 2000, 295.
- [73] N. Gaponik, D. V. Talapin, A. L. Rogach, K. Hoppe, E. V. Shevchenko, A. Kornowski, A. Eychmüller, H. Weller, *J. Phys. Chem. B*, **106**, 2002, 7177.
- [74] A. L. Rogach, T. Franzl, T. A. Klar, J. Feldmann, N. Gaponik, V. Lesnyak, A. Shavel, A. Eychmüller, Y. P. Rakovich, J. F. Donegan, *J. Phys. Chem. C*, **111**, 2007, 14628.
- [75] A. K. Gaigalas, L. Wang, *J. Res. Natl. Inst. Stand. Technol.*, **113**, 2008, 17.
- [76] T.A. Kelf, Y. Sugawara, R.M. Cole, J.J. Baumberg, M.E. Abdelsalam, S. Cintra, S. Mahajan, A.E. Russell, and P.N. Bartlett, *Phys. Rev. B.*, **74**, 2006, 245415.
- [77] <http://www.timkelf.com/ResearchSurfacePlasmons.html>
- [78] A. J. Tudos, R. B. M. Schasfoort, Handbook of Surface Plasmon Resonance, RSC Publishing (2008).
- [79] T. A. Kelf, “Light-Matter Interactions on Nano-Structured Metallic Films” (PhD Thesis), 2006.
- [80] A. Otto, I. Mrozek, H. Grabborn, W. Akemann, *J. Phys.: Condens. Matter*, **4**, 1992, 1143.
- [81] P.K. Jain, W. Qian, M. A. El-Sayed, *J. Phys. Chem. B*, **110**, 2006, 136.
- [82] K. Lance Kelly, Eduardo Coronado, Lin Lin Zhao, and George C. Schatz, *J. Phys. Chem. B*, **107**, 2003, 668.
- [83] M. H. Chowdhury, K. Ray, S. K. Gray, J. Pond, J. R. Lakowicz, *Anal. Chem.*, **81**, 2009, 1397.
- [84] U. Kreibig, M. Vollmer, Optical Properties of Metal Clusters, Springer Verlag, Berlin, 1995.
- [85] <http://www.cinam.univmrs.fr/confs/FrontNanoSpinPhoto/PDF/BONOD.pdf>
- [86] Raether H: Surface Plasmons on Smooth and Rough Surfaces and on Gratings. Berlin: Springer-Verlag; 1988.
- [87] L. M. Liz-Marzan, *Langmuir*, **22**, 2006, 32.
- [88] J. R. Heath, C. M. Knobler, D. V. Leff, *J. Phys. Chem. B*, **101**, 1997, 189.
- [89] S. W. Chen, R. S. Ingram, M. J. Hostetler, J. J. Pietron, R. W. Murray, T. G. Schaaff, J. T. Khoury, M. M. Alvarez and R. L. Whetten, *Science*, **280**, 1998, 2098.
- [90] M. M. Alvarez, J. T. Khoury, T. G. Schaaff, M. N. Shafiqullin, I. Vezmar and R. L. Whetten, *J. of Phys. Chem. B*, **101**, 1997, 3706.
- [91] J. J. Mock, M. Barbic, D. R. Smith, D. A. Schultz, S. Schultz, *J. Chem. Phys.*, **116**, 2002, 15.
- [92] B. Rodriguez-Gonzalez, A. Burrows, M. Watanabe, C. J. Kiely and L. M. Marzan, *J. Mat. Chem.*, **15**, 2005, 1755.
- [93] P. Mulvaney, M. Giersig and A. Henglein, *J. Phys. Chem.*, **97**, 1993, 7061.
- [94] L. M. Liz-Marzán, M. Giersig, P. Mulvaney, *Langmuir*, **12**, 1996, 4329.
- [95] S. Kühn, U. Hakanson, L. Rogobete, V. Sandoghdar, *Phys. Rev. Lett.*, **97**, 2006, 017402.
- [96] O. Kulakovich, N. Strekal, A. Yaroshevich, S. Maskevich, S. Gaponenko, I. Nabiev, U. Woggon, M. Artemyev, *Nano Lett.*, **2**, 2002, 1449.

-
- [97] a) M. Futamata, Y. Maruyama, M. Ishikawa, **107**, 2003, 7607; b) T. Nakamura, S. Hayashi, *Jpn. J. Appl. Phys.*, **44**, 2005, 6833.
- [98] a) Y. Fedutik, V. Temnov, O. Schöps, U. Woggon, M. V. Artemyev, *JACS*, **129**, 2007, 14939; b) Y. Fedutik, V. Temnov, O. Schöps, U. Woggon, M. V. Artemyev, *Phys. Rev. Lett.*, **99**, 2007, 136802.
- [99] T. Ming, L. Zhao, Z. Yang, H. Chen, L. Sun, J. Wang, C. Yan, *Nano Lett.*, **9**, 2009, 3896.
- [100] M. A. Noginov, G. Zhu, A. M. Belgrave, R. Bakker, V. M. Shalaev, E. E. Narimanov, S. Stout, E. Herz, T. Suteewong, U. Wiesner, *Nature*, **460**, 2009, 1110.
- [101] N. Liu, B. S. Prall, V. I. Klimov, *J. Am. Chem. Soc.*, **128**, 2006, 15362.
- [102] P. B. Johnson, R. W. Christy, *Phys. Rev. B*, **6**, 1972, 4370.
- [103] J. Gersten, A. Nitzan, *J. Chem. Phys.*, **75**, 1981, 1139.
- [104] F. Kong, Y. M. Sun, R. K. Yuan, *Nanotechnology*, **18**, 2007, 957.
- [105] B. P. Lyons, K. S. Wong, A. P. Monkman, *J. Chem. Phys.*, **118**, 2003, 4707.
- [106] A. R. Buckley, M. D. Rahn, J. Hill, J. Cabanillas-Gonzalez, A. M. Fox, D. D. C. Bradley, *Chem. Phys. Lett.*, **339**, 2001, 331.
- [107] K. Brunner, J. A. E. H. van Haare, B. M. W. Langeveld-Voss, H. F. M. Schoo, J. W. Hofstraat, A. Van Dijken, *J. Phys. Chem. B*, **106**, 2002, 6834.
- [108] A. Aneja, N. Mathur, P. K. Bhatnagar, P. C. Mathur, *J. Biol. Phys.*, **34**, 2008, 487.
- [109] K. Tada, H. Harada, M. Onoda, H. Nakayama, K. Yoshino, *Synth. Met.*, **102**, 1999, 981.
- [110] J. Cabanillas-Gonzalez, A. M. Fox, J. Hill, D. D. C. Bradley, *Chem. Mater.*, **16**, 2004, 4705.
- [111] S.-K. Hong, K. H. Yeon, S. W. Nam, *Physica E*, **31**, 2006, 48.
- [112] H. V. Demir, S. Nizamoglu, T. Ozel, E. Mutlugun, I. O. Huyal, E. Sari, E. Holder, N. Tian, *N. J. Phys.*, **9**, 2007, 1367.
- [113] J. H. Park, J. Y. Kim, B. D. Chin, Y. C. Kim, J. K. Kim, and O. O. Park, J. KyeongKim, O. O. Park, *Nanotechnology*, **15**, 2004, 1217.
- [114] N. Cicek, S. Nizamoglu, T. Özel, E. Mutlugun, D. U. Karatay, V. Lesnyak, T. Otto, N. Gaponik, A. Eychmüller, H. V. Demir, *Appl. Phys. Lett.*, **94**, 2009, 061105.
- [115] S. Saini, S. Bhowmick, V. B. Shenoy, B. Bagchi, *J. Photochem. Photobiol. Chem.*, **190**, 2007, 335.
- [116] T. Kietzke, D. Neher, M. Kumke, R. Montenegro, K. Landfester, U. Scherf, *Macromolecules*, **37**, 2004, 4882.
- [117] C. Wu, Y. Zheng, C. Syzmanski, J. McNeill, *J. Phys. Chem. C Nanomater. Interfaces*, **112**, 2008, 1772.
- [118] S. Grigalevicius, M. Forster, S. Ellinger, K. Landfester, and U. Scherf, *Macromol. Rapid Commun.*, **27**, 2006, 200.